Spring 5-15-2017

Development and applications of novel fluorescent molecular probe strategies

Dolonchampa Maji
Washington University in St. Louis

WASHINGTON UNIVERSITY IN ST. LOUIS

School of Engineering and Applied Science

Department of Biomedical Engineering

Dissertation Examination Committee:
Samuel Achilefu, Chair
Mark Anastasio
Gregory M. Lanza
Srikanth Singamaneni
Lihong V. Wang
Katherine N. Weilbaecher

Development and applications of novel fluorescent molecular probe strategies

By

Dolonchampa Maji

A dissertation presented to
The Graduate School
of Washington University in
partial fulfillment of the
requirements for the degree
of Doctor of Philosophy

May 2017
St. Louis, Missouri

Table of Contents

List of Figures

List of Tables

List of Abbreviations

Chapter 1: Near infrared (NIR), Diffuse Optical Tomography (DOT), Fluorescence Molecular Tomography (FMT).

Chapter 2: Forster Resonance Energy Transfer (FRET), Dimethyl Sulfoxide (DMSO), Bovine Serum Albumin (BSA), Phosphate Buffered Saline (PBS), QE (Quenching Efficiency), Fluorescence Lifetime (FLT).

Chapter 4: Sub-surface depth (d_{ss}), total depth (d_{total}), object depth (d_{obj}).

Chapter 5: Fluorescence Lifetime (FLT), Fluorescence Lifetime Imaging Microscopy (FLIM)

Chapter 7: Circulating Tumor Cell (CTC), Red blood cell (RBC).

Chapter 8: Natriuretic Peptide Clearance Receptor (NPR), C-type Atrial Natriuretic Factor (CANF), Fluorescence Molecular Tomography (FMT)

Acknowledgments

I have loved my time at Washington University in St. Louis, and specially, the Optical Radiology Lab (ORL), where I have learnt from an extremely hard-working and brilliant group of researchers, and above all grown tremendously as a person. First, I would like to thank my mentor Dr. Samuel Achilefu for his constant support and motivation throughout my studies, and my growth as a person and as an independent researcher. He has always been a great inspiration for me and at the same time, been a great critic of my work, which has helped me always raise the bar for myself. I cannot thank him enough for his parent-like support during an extremely difficult phase of my life after the loss of my mother. Next, I would like to thank all my committee members for giving me great advice and fresh perspectives on my research directions. Special thanks to Dr. Gregory Lanza for his constant motivation, guidance and mentorship. I thank the ORL faculties: Dr. Monika Shokeen, Dr. Mikhail Berezin, Dr. Walter Akers and Dr. Joe Culver for their support. Special thanks to Brenda Phelps and Danielle Napoli at ORL for all the administrative support. Thanks to the Department of Biomedical Engineering for its assistance specially Karen Teasdale and Kate Ruzicka.

I would next want to thank the wonderful Achilefu group for the great experience it has been – for the great collaborative research environment both during the feisty debates in our group meetings as well as the fun times during lab get-togethers. Above all, I would like to thank Dr. Mingzhou Zhou and Dr. Pinaki Sarder who mentored me and helped create a great foundation for my thesis research. I am grateful to Dr. Rui Tang, Kexian Liang, Gail Sudlow and all members of the ORL, present and past, without whose assistance much of the work would have been impossible. I was fortunate to be in the company of wonderful fellow PhD students – Rebecca, Jessica, Deep, Liz,

Avik, Lemoyne, Suman, Metasebya, Karla, Jon, and Matt who have helped me grow and challenge my abilities as a researcher. The future of the lab lies in great hands – Daniel, Liz, Rebecca, Lemoyne, Deep, all of whom have helped make the lab a better place.

I have missed my family - my late mother, my father, and my sister - the most during my time in St. Louis. They have been the single biggest source of strength for me - they have listened to all I had to say and in return, always given me courage by expressing their relentless faith in my ability. I am immensely thankful to Sagar, and his parents, Saroj Uncle and Kaberi Aunty who has been a pillars of strength for me. Sagar has always been a source of positive energy, support and encouragement during the challenges of graduate school and life.

I am fortunate to have friends in St. Louis, who have lent me great support in good and bad times: Ravi, Anu, Hemangi, Piyush, Suman, Vasavi, Kirti, and plenty more. Very special thanks to Ravi and Anu for making St. Louis home away from home, you both are family to me. Your limitless support, love, encouragement, guidance, and relentless faith in me at each and every step of my personal and professional lives have been and will be irreplaceable. I cannot thank you enough for always being there as pillars of strength for me.

I am grateful to all the sources of funding which have enabled my research. I was partially supported by the Imaging Sciences Pathway graduate student fellowship offered by the Division of Biology and Biomedical Sciences (DBBS), Washington University in St. Louis (Grant number: T32 EB014855 21st Century Imaging Training Grant). Funding was provided in part from the US National Institutes of Health (NIH) NCI (R01 CA171651 and P50 CA094056), NIBIB (R01 EB007276 and R01 EB008111), and shared instrumentation grants (S10 OD016237 and S10 RR031625), NIH NCI: R01CA176221 and the Center for Multiple Myeloma Nanotherapy

(U54CA199092. Imaging services were provided by WU-MDACC Inter-Institutional Molecular Imaging Center (NCI P50CA094056) and the Siteman Cancer Center Small Animal Imaging Core (NCI P30CA091842*)*. And finally, I thank the readers for their time and attention.

Dolonchampa Maji,

Washington University in St. Louis

May 2017

Dedicated to

My late mother, Mrs. Reba Maji, she lives through my good deeds; and my father, Dr. Nanda dulal Maji.

For believing in me,

for their limitless love, support and sacrifices,

and for pardoning my imperfections, large and small.

ABSTRACT OF THE DISSERTATION

Development and applications of novel fluorescent molecular probe strategies

By

Dolonchampa Maji

Doctor of Philosophy in Biomedical Engineering

Washington University in St. Louis, 2017

Advisor: Samuel Achilefu, Ph.D.

Abstract

Optical imaging and spectroscopy technologies offer the ability to provide structural and functional information in a fast, low-cost, ionizing radiation free, highly sensitive and high throughput fashion. The diverse contrast mechanisms and complementary imaging platforms form the foundation for the application of optical imaging in pre-clinical studies of pathophysiological development as well as direct clinical application as a tool for diagnosis and therapy. Fluorescence imaging techniques have been one of the most rapidly adopted methods in biology and biomedicine. Visualization of biological processes and pathologic conditions at the cellular and tissue levels largely relies on the use of exogenous fluorophores or their bioconjugates. Some fluorescent molecular probes provide usable contrast for disease diagnosis due to their responsiveness to interactions with other molecular species and/or immediate microenvironment. As a result, understanding exogenous fluorescent contrast mechanisms will allow the development of efficient strategies for biomedical fluorescence imaging.

The present work focuses on exploring novel fluorescent molecular probe strategies for imaging cancer and cardiovascular diseases. We have developed a platform for synthesizing activatable fluorescent molecular probes using the fluorescence quenching properties of copper (II) ions. We used these activatable probes for rapid imaging of cancerous tissue *in vivo* in mice. While developing these molecular probes, we discovered an unexpected molecular interaction that yields stable dimeric molecules. This finding can potentially enable the development of new molecular entities for modifying the signaling properties of fluorescent dyes to minimize background fluorescence.

Although planar fluorescence imaging methods using exogenous molecular probes provide rapid information about molecular processes *in vivo*, extraction of depth information require complex data acquisition and image analysis methods. By designing a dual emission fluorescent probe incorporating two spectrally different fluorophore systems, we developed a method to successfully estimate the depth of fluorescent inclusions from planar imaging data and demonstrated the potential of using this approach to locate a blood vessel and tumorous tissue in mouse *in vivo*.

An important feature of fluorescence methods is the availability of various techniques that provide complementary information. Combining the fluorescence intensity and lifetime properties of a biologically targeted near infrared fluorescent probe, we demonstrate an effective way to distinguish specific from nonspecific uptake mechanisms in cancer cells, an approach that can be translated *in vivo*. Alternatively, dynamic fluorescence imaging technique expands the scope of applications to include detection and estimation of the size of circulating cancer cells and clusters. The approach developed in this work could allow longitudinal monitoring of these cells, which are implicated in cancer metastases.

To circumvent the shallow penetration of light using optical methods, we developed multimodal imaging approaches by incorporating a radionuclide for nuclear imaging into a broad spectrum near infrared fluorescent tumor targeting agent. This molecular construct allows for noninvasive whole body nuclear imaging of tumors, followed by fluorescence image guided resection. In each of these areas, novel fluorescent molecular probes were developed, characterized and applied to solve critical biomedical problems.

Chapter 1 Introduction

1.1. Introduction

Optical imaging technologies offer the ability to provide molecular and functional information in a fast, low-cost, high throughput, highly sensitive fashion.[2] This imaging modality exploits the interaction of light with biological tissue leading to a number of photophysical events such as absorption, scattering, and fluorescence emission (Figure 1-1). These diverse photophysical events provide optical imaging contrast which can be used to obtain both functional and structural information from the tissue of interest.[3] In optical imaging, light interaction with tissues begins with the scattering of light by cellular organelles or absorption by chromophores (endogenous or exogenous) present in the tissue of interest. Light scattering is defined as the deviation of a photon path from a straight trajectory as it travels through a heterogeneous medium. Mie's theory provides the most useful approximation for describing light scattering in biological tissue.[4,5] The theoretical and practical application of light scattering in biomedical imaging has been described in detail

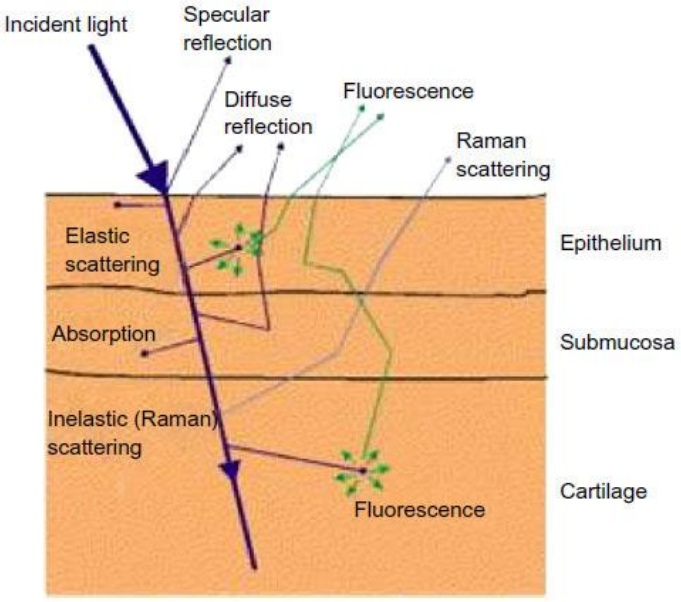

Figure 1-1: Schematic diagram of light pathways in a turbid media such as biological tissue (bronchial tissue shown here). [1]

earlier.[6] In absorption optical imaging, contrast is generated by the differential intensity of the

absorbing chromophores in the target tissue relative to the surroundings. Some intrinsic absorbers in the body that are used for generating contrast are oxyhemoglobin, deoxyhemoglobin, melanin, myoglobin, and waters. The energy of the light absorbed can also be converted or dissipated as heat to the surrounding tissue, a phenomenon that is useful for generating contrast for photoacoustic spectroscopy and imaging. [7] A special category of chromophores can convert this absorbed energy into re-emitted light at longer wavelengths than the incident light. This phenomenon is called fluorescence and the emitted light can be used for imaging the tissue of interest. These fluorescent molecules can be indigenous to the tissue of interest, in which case the phenomena is known as auto-fluorescence. In general, the term fluorescence is used for emission signal generated by exogenous contrast agents that are custom synthesized or expressed in cells and administered into the body to achieve contrast. In yet another type of optical contrast, light can be generated and emitted as a result of a biochemical reaction, such as the oxidation of luciferin by luciferase enzyme. This process is termed bioluminescence. The versatility of optical imaging methods and the diverse mechanism to generate optical contrast forms the basis of the optical imaging platforms that include spectroscopic, planar, diffuse, and hybrid biomedical optics methods. This chapter focuses on brief introduction to optical fluorescence imaging and its various characteristics that are explored in the following chapters for applications in imaging cancer and cardiovascular diseases.

1.2. Fluorescence imaging

Singlet state fluorescence occurs when a fluorophore molecule absorbs radiation of specific energy, followed by the emission of photons as the molecule returns to the ground state, as described in the Jablonski diagram [Figure 1-2]. Because energy is lost between the excitation and emission

processes, fluorescence is emitted at a higher wavelengths than those of the excitation radiation.[8] Several factors affect molecular fluorescence, including the molecular structures and associated vibrational energy levels as well as the physical and chemical environment of the fluorophores.[8] Perturbation of the fluorescence of many organic molecules could decrease the quantum yield at the same emission wavelength or cause spectral shift. Both effects are useful for biological applications. Within linearity, changes in the fluorescence intensity can be used to determine the concentration of fluorophores in a medium. Shifts in the spectral profile of fluorophores can provide quantitative data via ratiometric measurements at two different wavelengths. Although these approaches are highly reliable for reporting biological events in solutions or shallow surfaces, enhanced light scattering and absorption in heterogeneous mediums such as cells and tissue can adversely affect the fluorescence intensity in a less predictable manner. For these reasons, most fluorescence measurements in cells and tissue are typically reported on a relative intensity scale using calibration standards or by self-referencing. A variety of endogenous and exogenous fluorescent molecules are widely used for preclinical and clinical imaging of pathological processes.

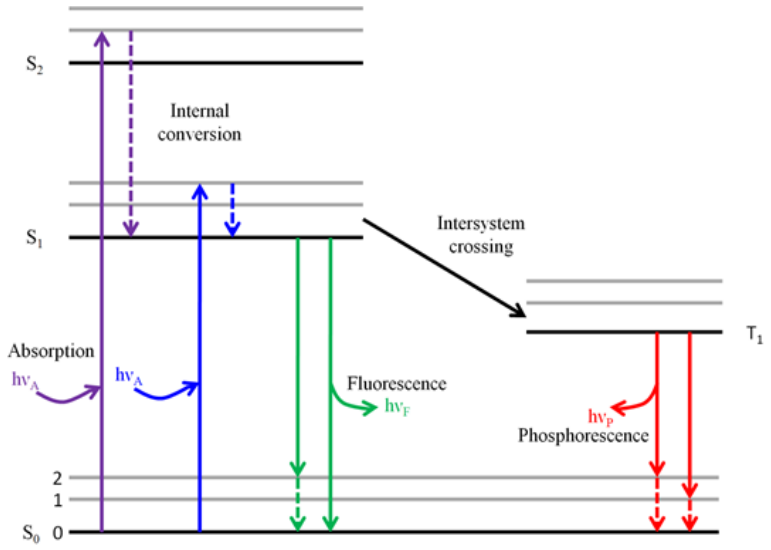

Figure 1-2: Jablonski diagram showing various processes following absorption of light by the fluorophore.[9]

1.2.1 Endogenous fluorescent molecules

Biological tissue has intrinsic fluorescence (also known as auto-fluorescence) due to endogenous fluorogenic molecules that emit in the UV and visible wavelengths.[10] The most prominent tissue fluorophores include nicotinamides and flavins, which are key molecules regulating cellular metabolism; aromatic amino acids (tryptophan, tyrosine, phenylalanine and histidine) which form the basic building blocks of proteins in the body; porphyrins which carry out the functions of transporting respiratory gas and fluorescent pigments (lipofuscins, melanin). Polymeric biomolecules, which are fluorescent, include structural proteins collagen and elastin. Several of these intrinsic fluorophores perform critical cellular and tissue functions and therefore are used. As a result, disruption of normal function can alter the endogenous fluorescence which can serve as a source of contrast for diagnosing pathophysiological processes. They are also regularly used to study the mechanisms of cellular and molecular processes and interactions in their native conditions.[10,11]

1.2.2 Exogenous fluorescent contrast agents

The shallow penetration of light in the UV and visible light regions of the electromagnetic spectrum, as well as the low expression of a target endogenous fluorophore in tissues of interest confine the applications of conventional optical imaging to specialized cases of pathophysiology. In addition, the often weak and nonspecific nature of the endogenous fluorescence further requires long signal acquisition time and sophisticated image analysis software to enhance detection sensitivity and decipher different types of tissue. These limitations can be overcome by the use of exogenous contrast agents and molecular probes.[11] Exogenous contrast allows customization of biological functionality by conjugation of the agent to appropriate targeting moiety. Fluorescent contrast agents that absorb and emit in the visible spectral range are well suited for superficial tissue imaging (for example diagnosis of skin cancer) and studies of cellular processes via microscopy. However, visible fluorescence signal is greatly attenuated in thick tissue primarily due to absorption and scattering. In the context of exogenous contrast, auto fluorescence signal provides a high background. In order to bypass these problems, fluorescent agents that absorb and emit in the near infrared (NIR) window have been developed (Figure 1-3). The NIR window allows greater depth penetration into biological tissue due to reduced absorption from biological chromophores and also bypasses tissue auto-fluorescence. Therefore NIR window is greatly suited for *in vivo* and deep tissue imaging. The Achilefu lab has been a pioneer in the development of several NIR fluorescent contrast agents for cancer imaging.

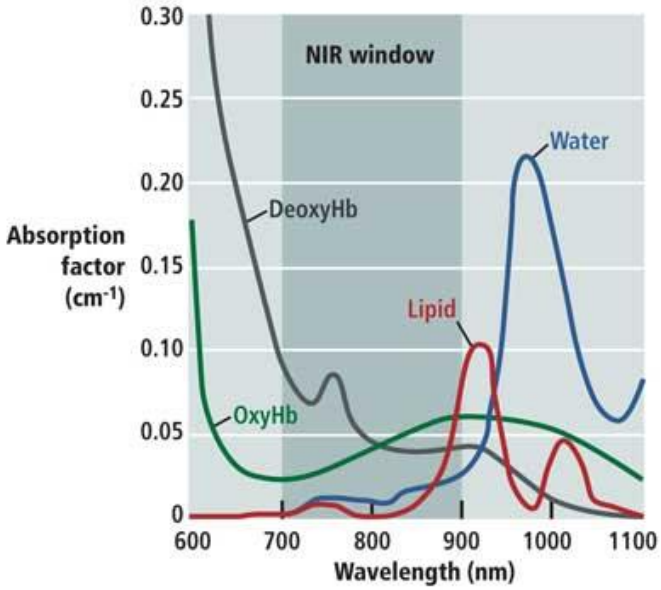

Figure 1-3: The NIR window (700 - 900 nm), showing the absorption coefficients of oxygenated hemoglobin (HbO_2), deoxygenated hemoglobin (Hb), and water (H_2O) reaching a minimum, making the therapeutic window ideal for *in vivo* imaging.[12]

1.3. Fluorescence Lifetime Imaging

Apart from the conventional intensity measurements, fluorescence also allows us to explore other features for imaging. An example is fluorescence lifetime (FLT or τ) of fluorophores, which is the average time a molecule spends in the excited state between absorption and emission of radiation before returning to the ground state. The lifetimes of fluorophores can range from picoseconds to hundreds of nanoseconds, which can be measured by the use of modern optical instrumentation. Mathematically, FLT is calculated as the time taken for the number of excited molecules to decay to 1/e or 36.8% of the original population of excited molecules. Fluorescence typically follows first order kinetics. As shown in the intensity decay figure [Figure 1-4], the fluorescence lifetime, τ, is the time at which the intensity has decayed to 1/e of the original value. The decay of the intensity as a function of time is given by:

$$I(t) = \alpha e^{-t/\tau} \quad \text{.....(1)}$$

Where, I(t) is the intensity at time t, α is a normalization term (the pre-exponential factor) and τ is the lifetime.

Unlike fluorescence intensity-based imaging, FLT of molecular probes is less dependent on the local fluorophore concentration or the method of measurement, which minimizes imaging artifacts and provides reproducible quantitative measurements over time. Accurate determination of the FLT of fluorophores and application in biological imaging and spectroscopy depends on both instrumentation and understanding of the fluorophore system. The FLT of a fluorophore can be measured by spectroscopic, microscopic, or *in vivo* imaging methods.[10] Several FLT instruments are commercially available for spectroscopic (e.g., Horiba) and microscopic (e.g., PicoQuant) measurements. For *in vivo* imaging, many studies rely on custom-built FLT systems because commercial sources are not available.

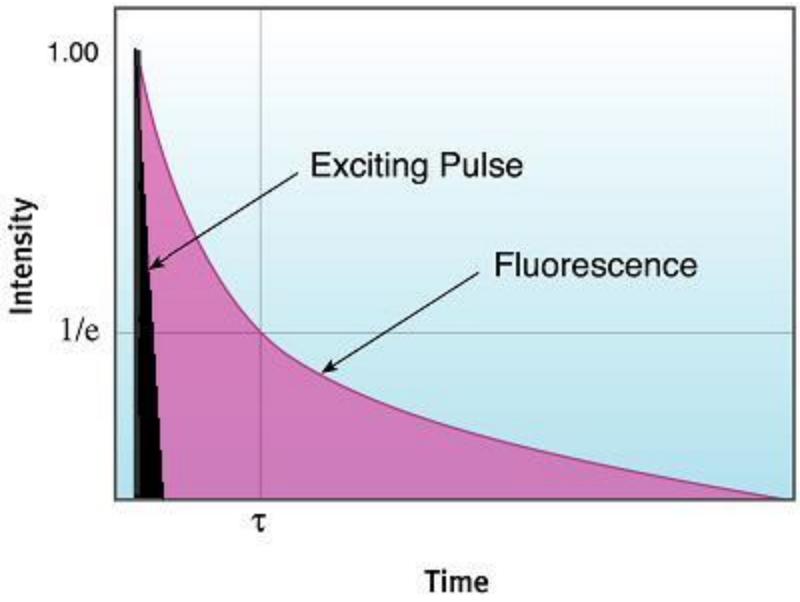

Figure 1-4: An intensity decay figure showing the fluorescence lifetime, T, which is the time at which the intensity has decayed to 1/e of the original value.[13]

1.4. Multimodal contrast agents

The idea behind using multimodal contrast agents is to obtain complementary diagnostic information through the administration of a single imaging agent. Dual labeled agents comprising of fluorescence and radionuclide moieties are one of the widely explored approaches. Using these agents whole body diagnostic imaging can be performed using nuclear imaging while the depth limited fluorescence signal can be used to provide real time image guidance during surgery. Examples include, fluorescence/PET or fluorescence/SPECT agents[14], fluorescence/ultrasound agents[15], and fluorescence/MRI agents[14].

1.5. Fluorescence imaging platforms for *in vivo* imaging

In this section, the basic principles of planar and diffuse optical imaging are described. These imaging techniques are used in the following chapters to perform optical fluorescence imaging. Detailed description of these methods have been published earlier.[16,17]

1.5.1 Planar Imaging

Planar fluorescence imaging techniques are most widely used for *in vivo* imaging. In the most basic design, light of appropriate wavelength is used to excite the fluorescent molecules. A high sensitivity camera (CCD/CMOS) is coupled to a high numerical aperture objective lens, which captures images with long exposure times. Desired fluorescence is separated from other signals by the use of appropriate band-pass filters. Planar imaging utilizes both ballistic and diffused light to rapidly obtain wide-field surface weighted projected fluorescent images of the tissue of interest (Figure 1-5). Such images may be used for real time feedback in pre-clinical and clinical applications. Exogenous fluorescent contrast agents can be used to provide contrast and thus identify the features of interest. When near-infrared (NIR) fluorescent dyes are used, tissues can be interrogated to greater depths (centimeter) than with visible light due to the NIR optical window.

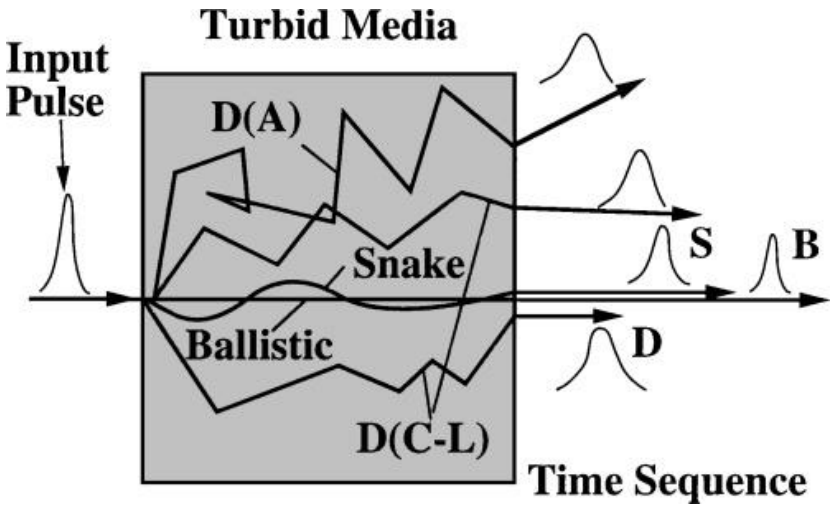

Figure 1-5: Schematic of the forward-scattered ballistic, snake, and diffusive photons propagating through a turbid medium. B, ballistic; S, snake; D, diffusive.[18]

1.5.1 Diffuse Optical Tomography & Fluorescence Molecular Tomography

To image light originating from greater depths, optical imaging relies on diffuse photons.[19] Diffuse Optical Tomography (DOT) involves combining signal measurements from multiple angles to computationally back calculate the spatial location of an object of interest in a scattering media such as biological tissue. DOT collects measurements of a 3D volume using a source-detector array, and these multiple measurements are then used to mathematically localize each volume element's relative contribution to the overall signal. DOT has been applied for imaging of brain function and breast cancer in humans. [20,21]

Fluorescence Molecular Tomography (FMT) employs the same principles of DOT, where fluorescence instead of absorption is captured. With the help of appropriate fluorescent contrast agents, FMT has been applied to image tissue of interest at centimeter depths in small animals.[22-24] One of the drawbacks of FMT is that the calculations require extensive computational capacity, which limits real-time feedback applications.

1.6. Conclusions

In this chapter we have briefly discussed basic principles, contrast mechanism and instrumentation needed for fluorescence optical imaging. In the following chapters, we will describe development application of custom fluorescent imaging agents and techniques to address specific biomedical imaging problems.

Chapter 2

Copper quenched fluorescent activatable molecular probes

2.1 Introduction

Fluorescent molecular probes have emerged as indispensable tools for detecting, imaging or quantifying diverse chemical and biomolecular processes with exceptional sensitivity. Activatable fluorescent probes are attractive in particular, as they allow for the modulation of the output fluorescence signal in response to the targeted molecular interaction, thus amplifying the signal in the target while minimizing the background signal.[25-27] For example, activatable probes based on protease susceptible peptides can be used for imaging and quantifying pathophysiological protease activity.[28-30] However, the development of efficient, versatile and biocompatible activatable probes remains challenging and an important area of research. Many activatable probes have been designed based on Förster Resonance Energy Transfer (FRET), which utilizes the highly efficient non-radiative transfer of excited state energy between molecules in close proximity. [27,29]

In general, efficient self-quenched activatable probes are obtained when multiple fluorophores are conjugated to polymers or nanoparticles. The slow activation and clearance of these macromolecules from blood require prolonged imaging time to achieve high contrast over background signal.[27,31] An alternative approach is to use small molecular fluorophore-quencher design to improve response time without loss of high signal-to-background contrast.[32] There is a paucity of efficient fluorescent quenchers in the near infrared (NIR) fluorescence region, an important spectral window for imaging deep tissue *in vivo* with minimal interference from tissue auto-fluorescence.[33,34] Most NIR dyes have narrow Stokes shifts, necessitating the development of tailored quencher molecules. In addition, many quencher molecules are themselves fluorescent, which result in the use of suboptimal excitation wavelengths to minimize signal overlap between the two dyes. Although non-fluorescent quencher molecules are available for visible dyes, efforts

to develop stable quenchers for broad spectrum NIR activatable probes remain a challenge. [27,35] A further complication is the elaborate synthetic route needed to prepare quencher dyes in the NIR region, as evidenced by the complex structure and high cost of an available commercial NIR quencher dye, which is also unstable under certain reaction conditions. [36]

In this study, we report a novel strategy for designing small molecular activatable probes across the visible and NIR spectral range by employing the broad spectrum quenching properties of Cu(II).[37-40] At room temperature, Cu(II) is a non-fluorescent quencher, facilitating the detection of fluorescence with high sensitivity. Complementary changes in fluorescence lifetime were associated with fluorescence quenching which could also be used to report probe activation.

2.2 Materials and Methods

2.2.1. Synthesis of Cu (II)-quenched activatable probes.

To demonstrate our concept, we developed four fluorescent probes **1**, **2**, **3** and **4** as described below. All chemicals and reagents were purchased from commercial sources and were used without further purification. Each step was characterized by liquid chromatography-mass spectrometry (LC-MS) using electrospray ionization (ESI) as the ionization method). The final molecules were characterized by high-resolution mass spectrometry (HRMS).

*Synthesis protocol of compounds **5, 1**, and **2***

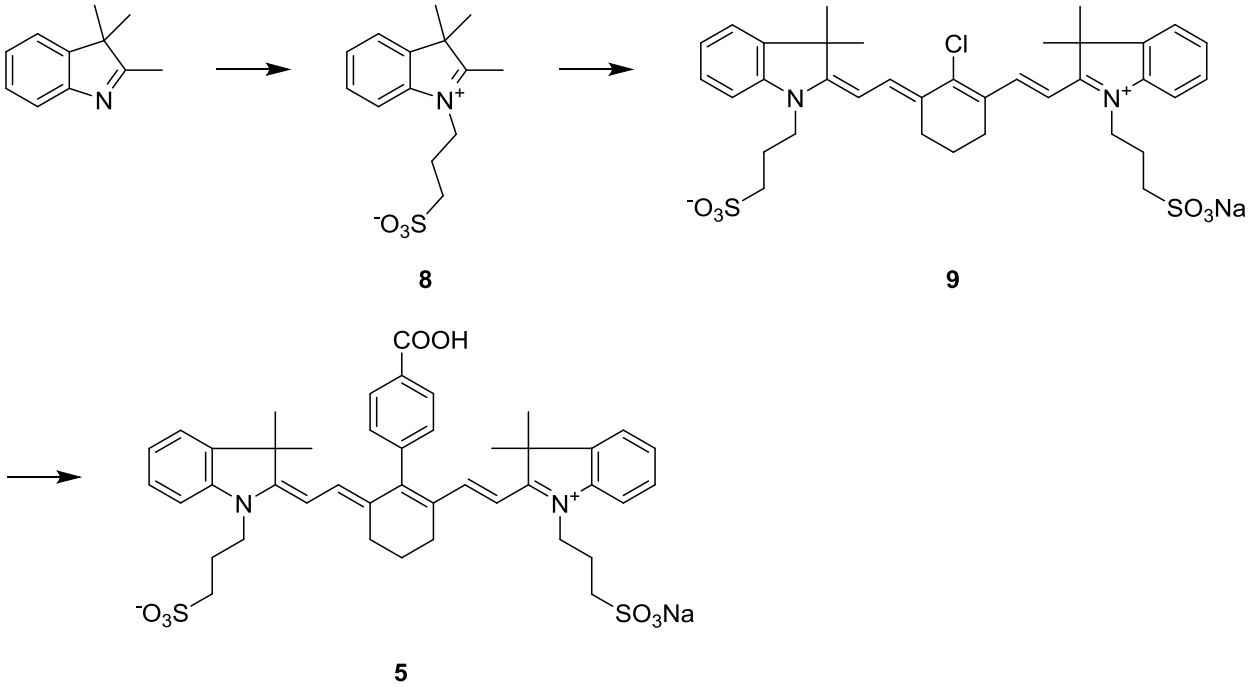

8 **9**

5

3-(2,3,3-Trimethyl-3H-indol-1-ium-1-yl)propane-1-sulfonate (8) To a suspension of 2,3,3-trimethylindolenine (16 mL, 20 mmol) in 1,2-dichlorobenzene (10 mL), 1,3-propanesultone (3.67 g, 60 mmol) was added. The mixture was stirred at 140 °C overnight. After cooled down to room temperature, the reaction mixture was filtered through sintered glass and the solid was rinsed with diethyl ether and acetone. The crude was used in the next step without further purification.

2-[2-[2-Chloro-3-[2-[1,3-dihydro-3,3-dimethyl-1-(4-sulfopropyl)-2H-indol-2-ylidene]-ethylidene]-1-cyclohexen-1-yl]-ethenyl]-3,3-dimethyl-1-(4-sulfopropyl)-3H-indolium hydroxide, inner salt sodium salt (9)

To a solution of **8** (3.65 g, 13 mmol) and sodium acetate (2.13 g, 26 mmol) in EtOH (32 mL) and acetic anhydride (32 mL), N-[(3-(Anilinomethylene)-2-chloro-1-cyclohexen-1-yl)methylene]aniline monohydrochloride (2.33 g, 6.5 mmol) was added. The reaction mixture was refluxed overnight. The solvent was then removed under reduced pressure. The crude was rinsed

with acetone followed by crystallization using MeOH and diethyl ether. The crude was used in the next step without further purification.

2-[2-[2-(4-carboxylphenyl)-3-[2-[1,3-dihydro-3,3-dimethyl-1-(4-sulfopropyl)-2H-indol-2-ylidene]-ethylidene]-1-cyclohexen-1-yl]-ethenyl]-3,3-dimethyl-1-(4-sulfopropyl)-3H-indolium hydroxide, inner salt sodium salt (5)

To a solution of **9** (290.8 mg, 0.4 mmol) and tetrakis(triphenylphosphine)palladium(0) (23.3 mg, 20 µmol) in H_2O (5 mL), 4-carboxyphenylboronic acid (120 mg, 0.7 mmol) was added. The reaction mixture was refluxed overnight. The crude was purified with reverse column chromatography (H_2O: MeOH = 1.5:1) to obtain **5** as a green solid.

^{1}H NMR (600 MHz, DMSO) δ 8.14 (d, J = 7.7 Hz, 2H), 7.44 (d, J = 7.3 Hz, 2H), 7.39 (dd, J = 11.4, 8.2 Hz, 4H), 7.30 (t, J = 7.5 Hz, 2H), 7.11 (t, J = 7.3 Hz, 2H), 6.98 (d, J = 13.9 Hz, 2H), 6.37 (d, J = 14.0 Hz, 2H), 4.29 – 4.19 (m, 4H), 2.73 – 2.64 (m, 4H), 2.52 – 2.48 (m, 4H), 1.98 - 1.86 (m, 6H), 1.06 (s, 12H). ^{13}C NMR (150 MHz, DMSO) δ 171.2, 167.0, 159.8, 146.8, 143.8, 142.1, 140.7, 130.8, 130.2, 129.7, 129.4, 128.4, 124.5, 122.4, 111.0, 100.6, 48.1, 47.8, 42.5, 27.0, 24.2, 23.3, 20.9.

HRMS m/z calculated for $C_{43}H_{47}N_2Na_2O_8S_2$ $[M + Na]^+$: 829.2564, found 829.2546. The yield calculated was %. Overall yield calculated was 18%.

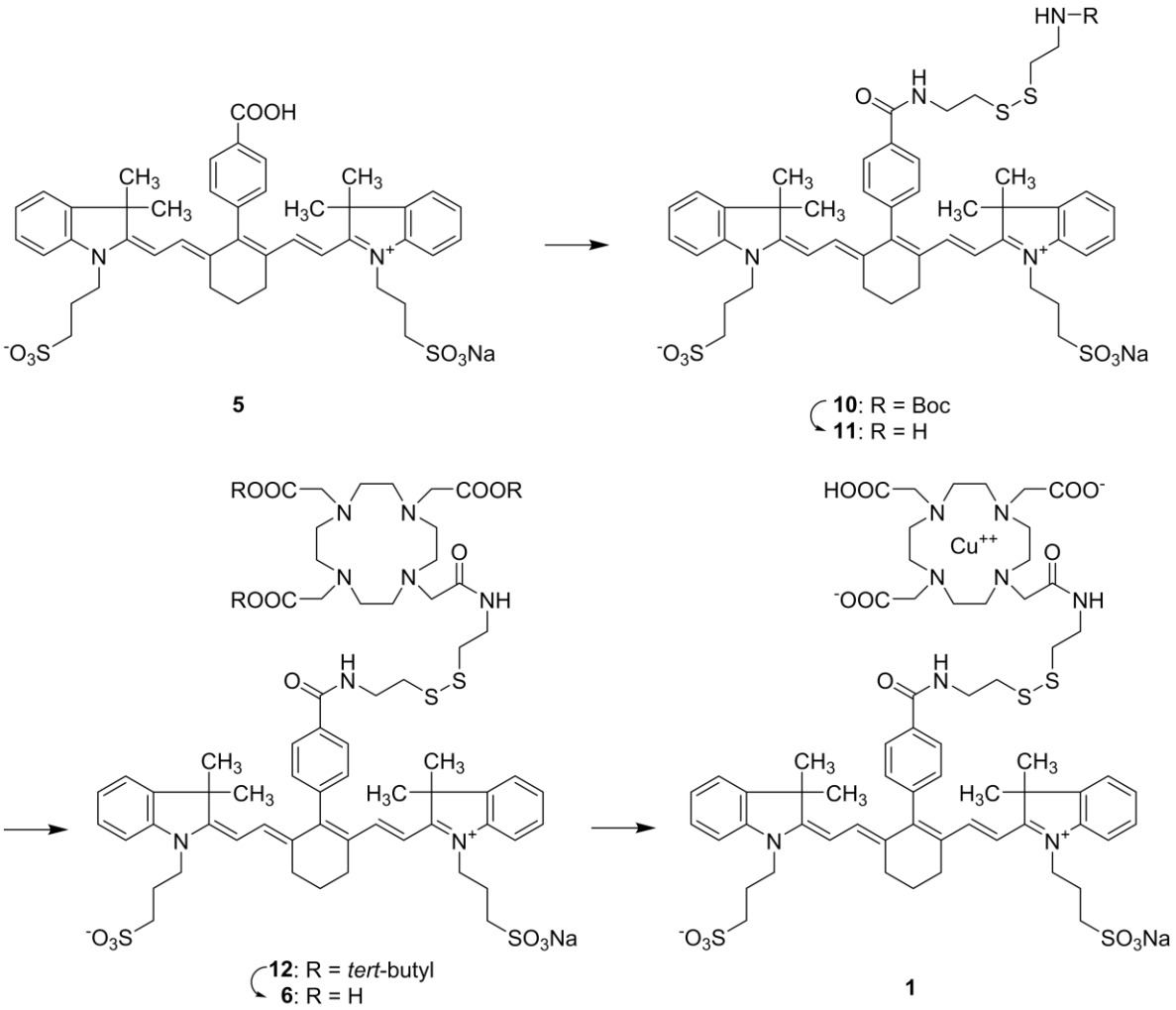

10: A mixture of **5** (18 mg, 23 µmol), HATU (21.9 mg, 57.5 µmol) and DIEA (7.4 mg, 57.5 µmol) in DMF (1 mL) was stirred for 20 min at room temperature. Boc-cystamine hydrochloride (19.9 mg, 69 µmol) in DMF (1 mL) was added to it and the final mixture was stirred at room temperature overnight in the dark. The solvent was then removed under reduced pressure to afford **10**, which was used in the next step without further purification.

11: To **10**, 3 mL of 50% TFA in DCM was added and the reaction mixture was stirred at room temperature for 2 hours. The solvent was removed under reduced pressure. The crude was further purified by HPLC equipped with a reverse-phase C-18 column to obtain **11** as a green solid. MS [ESI]: 820 $[M + H]^+$. Yield calculated was 88%.

12: A mixture of HATU (37.2 mg, 98 µmol), DIEA (12.7 mg, 98 µmol), DOTA-tris(*tert*-butyl)ester (34 mg, 58.8 µmol) in DMF (1 mL) was stirred for 20 min at room temperature. It was added to a suspension of **11** (18 mg, 19.6 µmol) in 20% DMSO in DMF (2 mL) and stirred at room temperature overnight in the dark. The solvent was then removed under reduced pressure. The crude was further purified by HPLC equipped with a reverse-phase C-18 column to obtain **12** as a green solid. Yield calculated was 75%.

6: To **12**, 2 mL of deprotecting mixture (TFA/H_2O/Phenol/Thioanisole; 85:5:5:5) was added and the mixture was stirred for 4 h. The solvent was removed under reduced pressure and the crude was further purified by HPLC equipped with a reverse-phase C-18 column to obtain **6** as a green solid. HRMS m/z calculated for $C_{63}H_{85}N_8O_{14}S_4$ $[M + H]^+$: 1305.5063, found 1305.4993. Yield calculated was 85%.

1: Molecule **6** was labeled with copper(II) using a previously use protocol for radioactive copper labeling.[41] Briefly, to a suspension of **6**, (0.2 mM) in 0.1 M ammonium acetate buffer (pH 5.5), copper (II) chloride (0.4-0.8 mM) was added. Small amounts of DMSO (<5%) was added to to increase the solubility of the compounds in the buffer. The reaction mixture was incubated at 40 °C for 1 h with shaking in the dark. The labeled compound was purified by HPLC equipped with a reverse-phase C-18 column to obtain **1** as a green solid. HRMS m/z calculated for $C_{63}H_{81}CuN_8Na_3O_{14}S_4$ $[M + 2Na]^{2+}$: 716.6867, found 716.6812. Yield calculated was 90%.

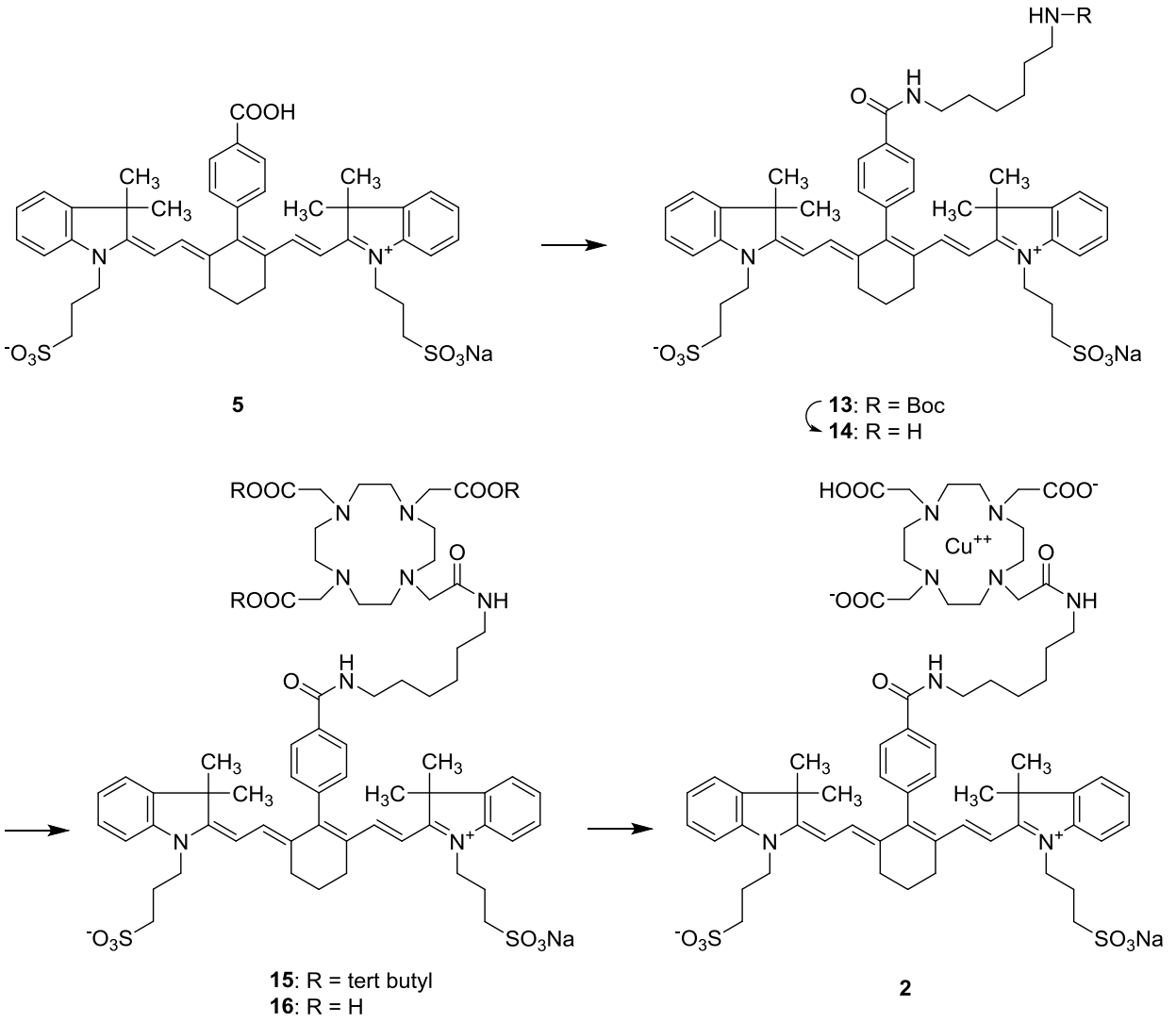

2: Molecule **2** was synthesized in a similar fashion as **1**, by replacing Boc-cystamine hydrochloride with N-Boc-1,6-hexanedimaine hydrochloride. HRMS m/z calculated for $C_{63}H_{85}CuN_8Na_3O_{14}S_2$ $[M + 2Na]^{2+}$: 698.7302, found 698.7265.

*Synthesis protocol of compound **3***

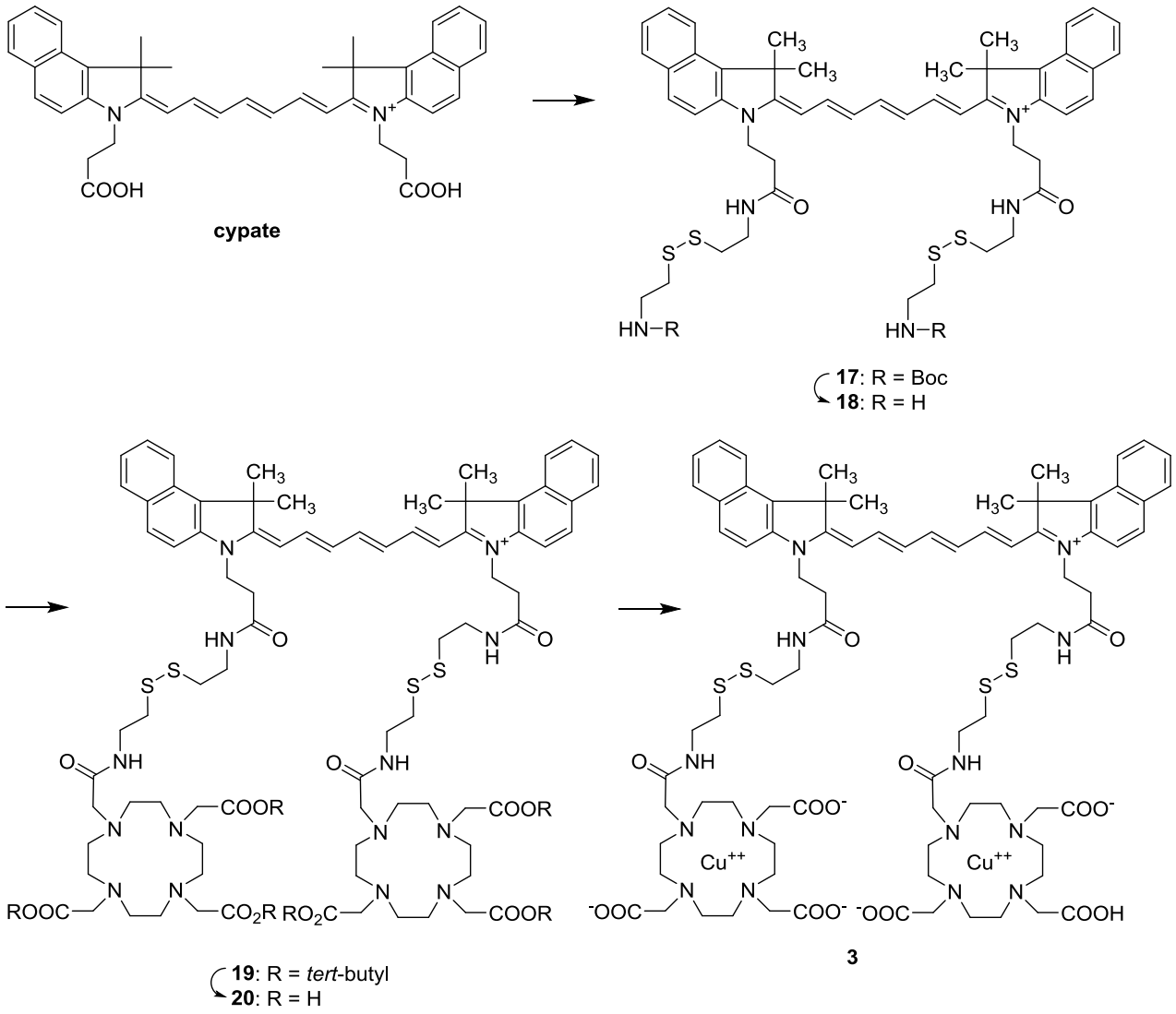

Cypate: It was synthesized using a previously reported protocol developed by the lab.

17: A mixture of Cypate (21 mg, 30 µmol) and DIC (22.7 mg, 180 µmol) in DMF (2 mL) was stirred for 20 min at room temperature. Mono-Boc-cystamine hydrochloride (34.7 mg, 120 µmol) in DMF (1 mL) was added to it and the mixture was stirred at room temperature overnight in the dark. The solvent was then removed under reduced pressure to afford **17**, which was used in the next step without further purification.

18: To **17** was added 3 mL of 50% TFA in DCM and the reaction mixture was stirred at room temperature for 2 h. The solvent was then removed under low pressure. The crude was further purified by HPLC equipped with a reverse-phase C-18 column to obtain **18**. MS [ESI]: 893 $[M + H]^+$. Yield calculated was 81%.

20: A mixture of HATU (19.1 mg, 50.3 µmol), DIEA (6.5 mg, 50.3 µmol) and DOTA-tris(*tert*-Butyl)ester (19.2 mg, 33.5 µmol) in DMF (1 mL) was stirred for 20 min at room temperature. It was added to a suspension of **18** (6 mg, 6.7 µmol) in DMF (2 mL) and the reaction mixture was stirred at room temperature overnight. The solvent was then removed under reduced pressure. The crude was further purified by HPLC equipped with a reverse-phase C-18 column to obtain **19** as a green solid. Yield calculated was 62%.

20: To **19**, 2 mL of deprotecting mixture was added and stirred for 4 h. The deprotecting mixture was removed under reduced pressure the crude was further purified by HPLC equipped with a reverse-phase C-18 column to obtain **20** as a green solid. MS [ESI]: 834 $[M + 2H]^+$, 595 $[M + 3H]^+$. Yield calculated was 79%.

3: Compound **17** was labeled with Cu(II) with the same method to label **16** to obtain 3. HRMS m/z calculated for $C_{81}H_{110}Cu_2N_{14}O_{16}S_4$ $[M + 2H]^{2+}$: 894.2844, found 894.2808. Yield calculated was 24%.

*Synthesis protocol of compound **4***

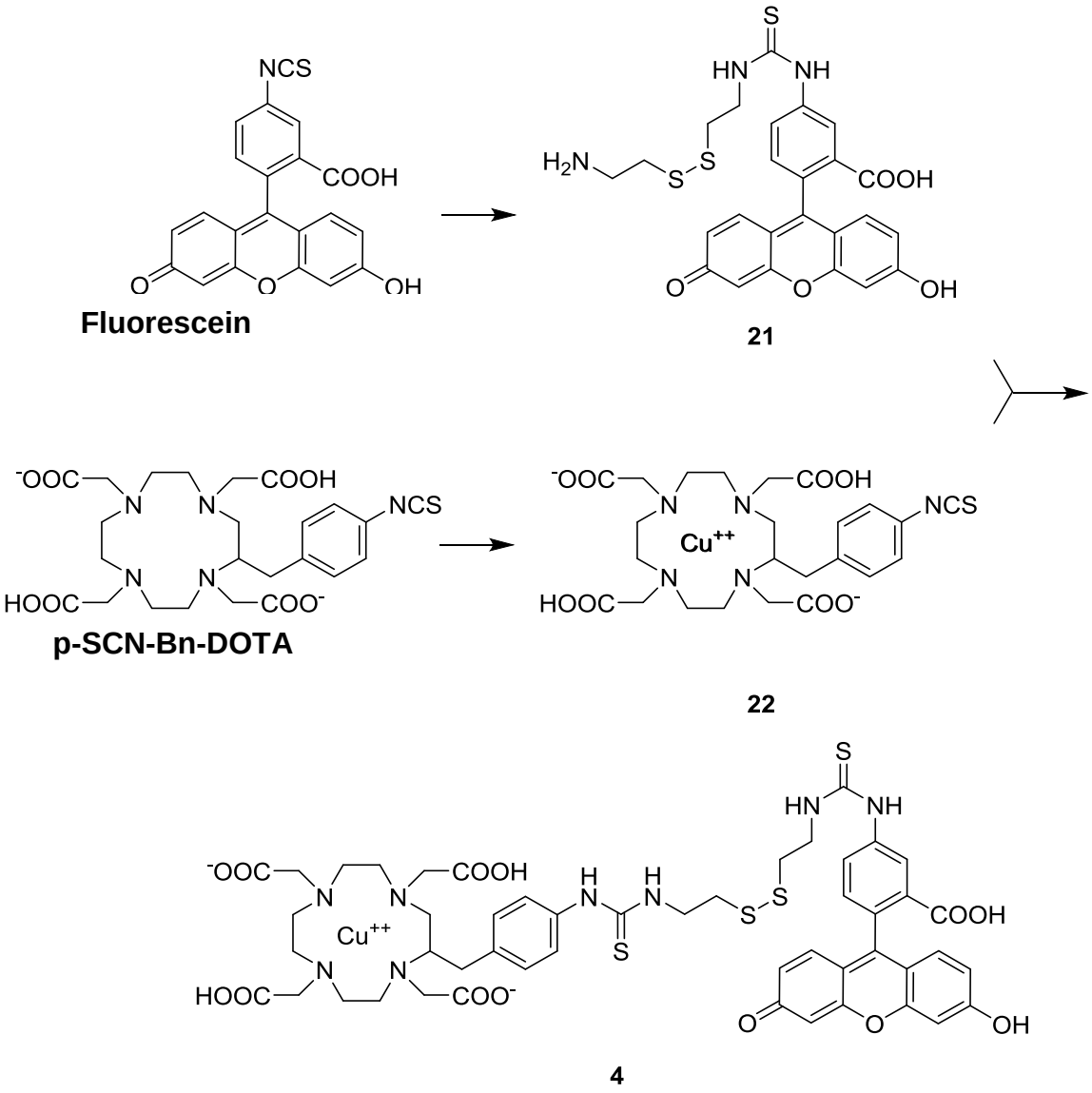

21: To a suspension of FITC (10 mg, 25.7 µmol) in sodium carbonate – sodium bicarbonate buffer solution (3 mL), cystamine hydrochloride (29.2 mg, 257 µmol) was added. The final pH was adjusted to 9.5. The mixture was stirred at room temperature overnight in the dark. The crude was further purified by HPLC equipped with a reverse-phase C-18 column to afford **21** as yellowish white solid. MS [ESI]: 542 $[M + H]^+$. Yield calculated was 89%.

2: To a suspension of p-SCN-Bn–DOTA in (1 mM) in 0.1 M ammonium acetate buffer (pH 5.5), copper (II) chloride (5 mM) was added. The solution was incubated at 50 °C for 1 h with shaking. The crude was further purified by HPLC equipped with a reverse-phase C-18 column to obtain **22** as a greenish blue solid. MS [ESI] : 613 $[M + H]^+$. Yield calculated was 95%.

4: To a suspension of the **22** (6 mg, 11 µmol) in sodium carbonate – sodium bicarbonate buffer solution (3 mL), **21** (18 mg, 33 µmol) was added. The final pH was adjusted to 9.5. The mixture was stirred at room temperature overnight in the dark. The crude was further purified by HPLC equipped with a reverse-phase C-18 column to obtain **4** as a pale yellow solid. HRMS m/z calculated for $C_{49}H_{55}CuN_8O_{13}S_4$ $[M + H]^+$: 1154.2062, found 1154.2029. Yield calculated was 78%.

The constructs were distance dependent quenching studies were synthesized as follows.

The overall molecular design consists of a cleavable disulfide linker that bridges the fluorescent dye and a metal chelating group (DOTA), a versatile chelating agent for many metal ions including Cu(II)[42]. Fluorescence quenching was achieved by chelating Cu(II) ions to DOTA. Furthermore, the cleavable disulfide linker can target elevated levels of intracellular reducing biomolecules and redox enzymes such as reduced glutathione and thioredoxin in cancer. This biochemical state has been used to design disulfide based activatable probes and prodrugs for targeted cancer imaging and therapy. [43] Thus, the versatility and selectivity of disulfide cleavage make it attractive for the development of Cu(II)-quenched activatable probes, which would be useful for *in vitro*, *in cellulo*, and *in vivo* imaging studies.

2.2.2. Spectroscopic characterization

The absorption spectra were measured on a DU 640 spectrophotometer (Beckman-Coulter, Brea, CA). For all fluorescence measurements, absorbance at the excitation wavelength was kept below 0.05. Fluorescence emission spectra were recorded on a FluoroLog 3 spectrofluorometer (Horiba Jobin Yvon, Edison, NJ) using 690 nm/705-900 nm, 720 nm/735-900 nm, or 450 nm/465-650 nm as excitation/emission wavelength with 5 nm slits for molecules containing **5**, cypate or FITC respectively. Quenching efficiency (QE) was calculated by quantifying the number of photons emitted (measured by the area under fluorescence emission curve) of the molecular probes before and after incorporation of Cu(II); with peak area normalized to absorbance at excitation wavelength. The following formula was used:

$$QE\ (\%) = \left[1 - \frac{\text{Normalized fluorescence peak area for } \mathbf{1}, \mathbf{2}, \mathbf{3} \text{ or } \mathbf{4}}{(\text{Normalized fluorescence peak area for } \mathbf{6}, \mathbf{16}, \mathbf{20} \text{ or } \mathbf{22}}\right] * 100$$

FLT were measured on the FluoroLog 3 spectrofluorometer using a 740 nm, 773 nm and 470 nm lasers for compounds containing **5**, cypate and FITC, respectively. The detection window was set to be centered at 790 nm, 823 nm or 530 nm with 20 nm, 20 nm or 10 nm bandpass respectively. The instrument response function was obtained using Rayleigh scatter of Ludox-40 (Sigma-Aldrich, St. Louis, MO). DAS6 v6.1 decay analysis software (Horiba) was used for FLT calculations. All decay curves except for those measured in PBS-BSA were fitted to two exponential decay curves unless otherwise stated. The major component (>97% relative amplitude) was reported or mean of components were reported. For measurements made in PBS-BSA, three exponential decay curves were used. The two major components (>95% relative amplitude combined) were reported.

Anhydrous trifluoroethanol was used to measure quenching efficiencies and lifetime of polyprine containing constructs for distance dependence study.

2.2.3. Spectroscopic study of probe activation

Solutions of the compounds 6 (0.4 μM), 1 (0.4 μM) and 2 (0.4 μM), 3 (0.2 μM) and 4 (1.4 μM) were prepared in 200 mM Tris-HCL buffer, pH 7.4 containing reduced L-Glutathione (GSH, 10 mM, final pH 6.9). Fluorescence emission spectra were taken from the resulting solutions at 2 min intervals. FLT was measured after 8 minutes of incubation. For calculate mean fluorescence recovery the fluorescence signal at 8 min post treatment were used.

2.2.4. Cytotoxicity assay

4T1-Luc cells (SibTech, Brookfield, CT) were cultured in Dulbecco's Modified Eagle Medium (DMEM) supplemented with 10% fetal calf serum, 100 units/mL penicillin, and 100 units/mL streptomycin. Cells were allowed to grow to 75% confluency and then detached from the plate using trypsin-EDTA to determine the number of cells. Approximately 8000 cells were seeded in the wells of a 96-well plate (BD Falcon). The respective compounds were added and the final volume in each well was kept 100 μL. Cells were incubated for 44 h at 37 °C in a 5% CO_2 atmosphere. Wells containing untreated cells were used as control.

Cytotoxicity assay reagent was obtained from a CellTiter96 non-radioactive cell proliferation assay kit (Promega).The reagent (20 μL) was added to each well and incubated for another 2.5 hours at 37 °C in a 5% CO2 atmosphere. Absorbance at 490 nm was measured using a Synergy plate reader (Biotek). Data were collected for four separate measurements and averaged.

2.2.5. Cellular fluorescence and lifetime imaging

4T1-Luc cells were cultured as mentioned before. About 10,000 cells were seeded per well in 8-well cell culture slides (BD Biosciences, San Jose, CA) and allowed to grow over-night. Before

microscopic imaging, cells were treated with 10 μM of the fluorescent dyes or molecular probes dissolved in DMSO, (final concentration of DMSO was kept < 0.8% v/v) and incubated for 0.5, 2, 4 and 12 hours cell culture incubator (37˚C, 5% atmospheric CO2). After incubation, cells were washed three times with PBS and covered with coverslip. The cells were visualized with an FV1000 confocal microscope (Olympus, Central Valley, PA) using 785 nm for excitation (Becker & Hickl, Germany) and emission passband at > 800 nm.

Fluorescence lifetime imaging was performed using a custom-built NIR FLIM system using the procedure described previously. [3] For each image, the decay data was collected for 120 s. The FLIM was performed using 0.921 mW of PW laser power at 50 MHz repetition rate.

2.2.6. Imaging data analysis

Confocal images were analyzed using ImageJ. Fluorescence was quantified by measuring the corrected whole cell fluorescence (CWCF) as follows:

CWFC = Total fluorescence signal detected from a single cell – (Mean fluorescence signal detected from adjacent background * Area of the cell)

For each image, mean CWFC was calculated by averaging CWCF from 10 cells. For independent experiments, the overall mean CWFC was calculated by averaging mean CWFC from each experiment.

For FLIM data, time traces acquired from the NIR FLIM system were analysed using the SPCImage software (Becker-Hickl, Germany). Images were binned to obtain more photon count pixel. Pixel by pixel time traces were fit to double exponential decay for 1 and single exponential decay for 6 and 2, assuming only probe 2 will have two fluorescent molecules before and after activation in cells. In all cases, background noise was eliminated by thresholding out decay traces

with less than 50 photons peak count. However the quenched probe 2 especially at lower time points showed very low photon counts. For it, the threshold value was reduced to 30 photons peak count. Curve fitting was performed by limiting expected lifetime values between 100-1600 ps as expected from the *in vitro* data. Chi squared values were used to determine goodness of fit. Mean FLT value for each image was calculated by averaging the corresponding FLT histogram (100-1600 ps) obtained. Global decays analyses was performed by obtaining the overall time trace from each image. Typical peak photon count >>3000 photons for all global decays.

All graphs were plotted using Prism software (GraphPad).

2.3 Results

2.3.1 Activatable fluorescent molecular probes

We synthesized four activatable probes **1**, **2**, **3** and **4** to demonstrate our idea [Figure 2-1]. Activatable probe **1** was synthesized using a hydrophilic NIR fluorescent cyanine dye with a reactive carboxylic acid function (**5**). We also synthesized a non-disulfide linker analogue **2**, to serve as the non-activatable control probe. To demonstrate the versatility of the Cu(II) quenching platform, we used a structurally different hydrophobic NIR dye cypate[44] to synthesize **3**. The two reactive carboxylic acid groups of cypate enabled the attachment of two Cu(II)-DOTA chelates

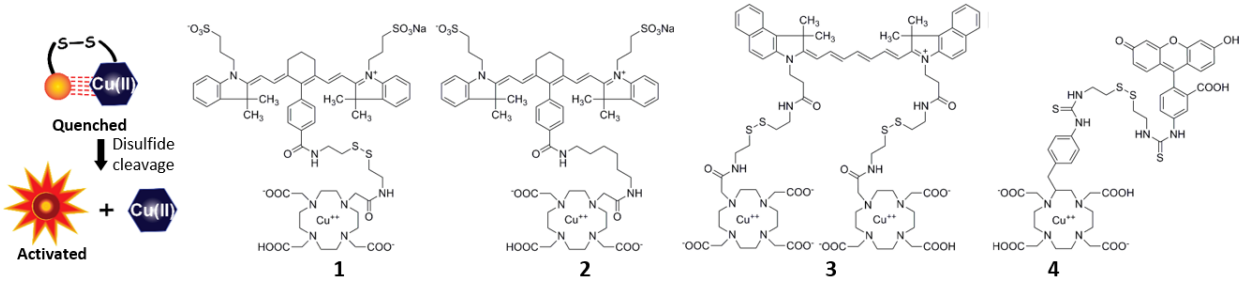

Figure 2-1: Design concept of disulfide based Cu(II) quenched activatable probe and molecular structures of the probes synthesized.

per dye molecule. Assessment of the Cu(II)-quenching of visible fluorescence was achieved by synthesizing activatable molecular probe **4** using fluorescein isothiocyanate (FITC, isomer 1). The ease of cleaving a disulfide bond in the presence of reducing reagents, such as reduced glutathione, dithiothreitol and 2-mercaptoethanol, creates a simple molecular platform for designing activatable probes. For cancer imaging, the high intracellular redox environment, due to elevated levels of intracellular reducing biomolecules such as reduced glutathione and thioredoxin, provides a mechanism for enhanced signal amplification in tumor cells. [43,45-48]

2.3.2. Spectral properties

We measured and compared the optical properties of the probes **1**, **2**, **3** and **4** and the corresponding non-Cu(II) containing reference molecules in dimethyl sulfoxide (DMSO), phosphate buffered saline (PBS; pH 7.4), and PBS with 1% (w/v) bovine serum albumin (PBS-BSA) (except for **4** which was insoluble in DMSO). In all cases, the incorporation of Cu(II) efficiently quenched the fluorescence emission intensity and decreased the fluorescence lifetimes (FLTs) of both NIR and visible fluorescent dyes (**Error! Not a valid bookmark self-reference.**, Table 2-1). These changes were also found to be solvent dependent. Compared to the quenching efficiencies of **1** and **2**, which have a single Cu(II) chelate per dye molecule, compound **3** with two Cu(II) chelates per molecule exhibited higher and relatively less solvent dependent fluorescence quenching. In PBS-BSA, the FLTs exhibited two decay components, which can be attributed to the presence of free and albumin-bound species.[8]

The broad spectrum fluorescence quenching by Cu(II) across visible and NIR wavelengths can be explained by the combination of photoinduced electron transfer and energy transfer processes. The significant overlap between the absorption spectrum of Cu(II)–DOTA and fluorescence emission

Table 2-2: Quenching efficiencies[a] of the molecular probes.

	DMSO	PBS	1% BSA in PB
1	74±3	84±1	82±1
2	71±1	80±1	80±1
3	92±4	93±5	95±3
4[b]	-	71±2	49±8

[a] Mean (%) ± s.d. (%) for three independent measurements (see ESI† for the formula of quenching efficiency). [b] Compound **4** is insoluble in DMSO.

spectra of the NIR fluorescent dyes suggests a strong contribution of energy transfer to the

Table 2-1: Fluorescence lifetimes[a] of the molecular probes and corresponding non-copper containing reference molecules.

	DMSO	PBS	1% BSA in PBS
6	1.44	0.41	1.28 [τ_a =1.53 (60%), τ_b = 0.75 (38%)]
1	0.64	0.22	0.69[τ_a =0.43 (70%), τ_b = 1.36(28%)]
2	0.66	0.21	0.66 [τ_a =0.43 (73%), τ_b = 1.35(25%)]
20	0.93	-	-
3[b]	0.23	-	-
22[c]	-	3.84	3.91 [τ_a = 4.08 (90%), τ_b = 2.35 (10%)]
4[c]	-	2.31	3.19 [τ_a = 3.85 (71%), τ_b = 1.58 (29%)]

[a] Denoted by τ (ns). Average lifetime with percentage components reported for measurements in the presence of BSA. Relative amplitudes of the exponential decay components in BSA-PBS are indicated as %. [b] Compound **3** had very low fluorescence for measuring FLT in aqueous media. [c] Compounds **22** and **4** were insoluble in DMSO. See ESI† for the structure of **6**, **20** and **22**.

quenching process. A relatively less overlap with the emission spectra of FITC indicates the dominance of electron transfer to the process. The lower quenching efficiencies of **4** probably reflect the lack of significant complementary energy transfer process in the visible region.

2.3.3. Spectroscopic probe activation

We assessed the fluorescence intensity and FLT recovery of the activatable probes after disulfide cleavage *in vitro*. We used time-dependent fluorescence emission measurement of a solution of 0.4 μM of 1, the non-activatable probe 2 or 6 (the corresponding non-Cu (II) containing molecule) in a typical intracellular concentration of reduced L-glutathione (GSH; 10 mM) in cancer cells. We observed a rapid increase in the fluorescence emission of 1 within the first 8 min (~4 fold; Figure 2-2A and B) in the solution. Insignificant changes in fluorescence emission of the corresponding non-Cu (II) containing molecule 6 and non-activatable probe 2 were observed. This result indicates fluorescence activation of 1 occurred by the cleavage of the disulfide bond (Figure 2-2C). Mass spectral analysis of the GSH-treated 1 and 2 confirmed the presence of the expected degradation products. The activation of 3 and 4 under similar conditions resulted in ~6.2 and ~4 fold increase in fluorescence emission, respectively. (Figure 2-2C). FLT analysis of the 1 and 4 post-GSH treatment showed an increase in FLT (Figure 2-2D), demonstrating the use of FLT to report probe activation. FLT increase for 3 is not reported as prior activation 3 has very low fluorescence emission for measuring FLT in the aqueous buffer. Treatment of the compounds with another reducing agent, dithiothreitol, exhibited similar fluorescence enhancement profiles as the

GSH-treated samples.

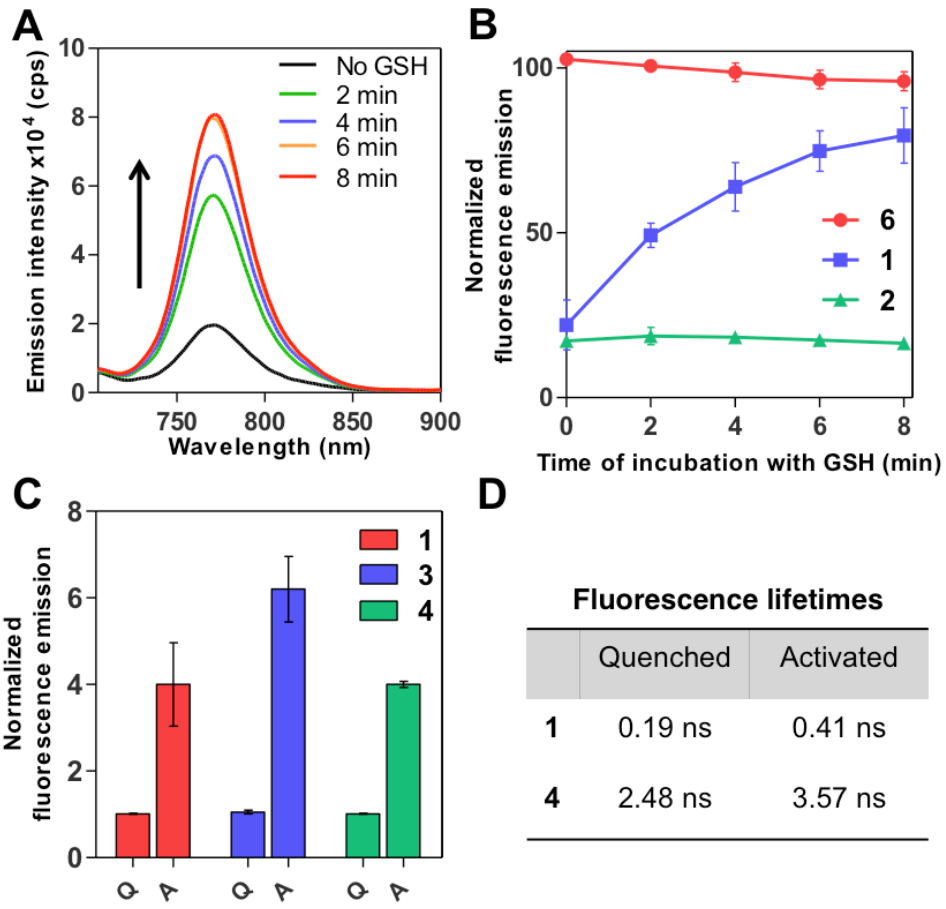

Figure 2-2: (A) Fluorescence spectral response of activatable probe 1 when incubated with 10 mM GSH showing fast recovery. (B) Fluorescence spectral response (mean fluorescence emission ± s.d.; three independent experiments) of 1 compared to the reference probe 6 and non-activatable probe 2 upon treatment with GSH. (C) Mean fluorescence recovery (mean ± s.d.; three independent experiments) upon GSH-mediated activation of all the activatable probes. (D) Recovery of FLT upon GSH-mediated activation of the quenched (Q) and activated (A, post GSH treatment for 8 min) states of the probes 1 and 4.

2.3.4. *In cellulo* fluorescence recovery

We then explored the feasibility of using the highly reducing intracellular environment of cancer cells to activate **1**. This required internalization of the activatable probe by cells and fluorescence enhancement via intracellular cleavage of the disulfide bond (Figure 2-3A). For this study, we used 4T1-Luc cells, a highly proliferative murine breast cancer cell line that exhibits high intracellular

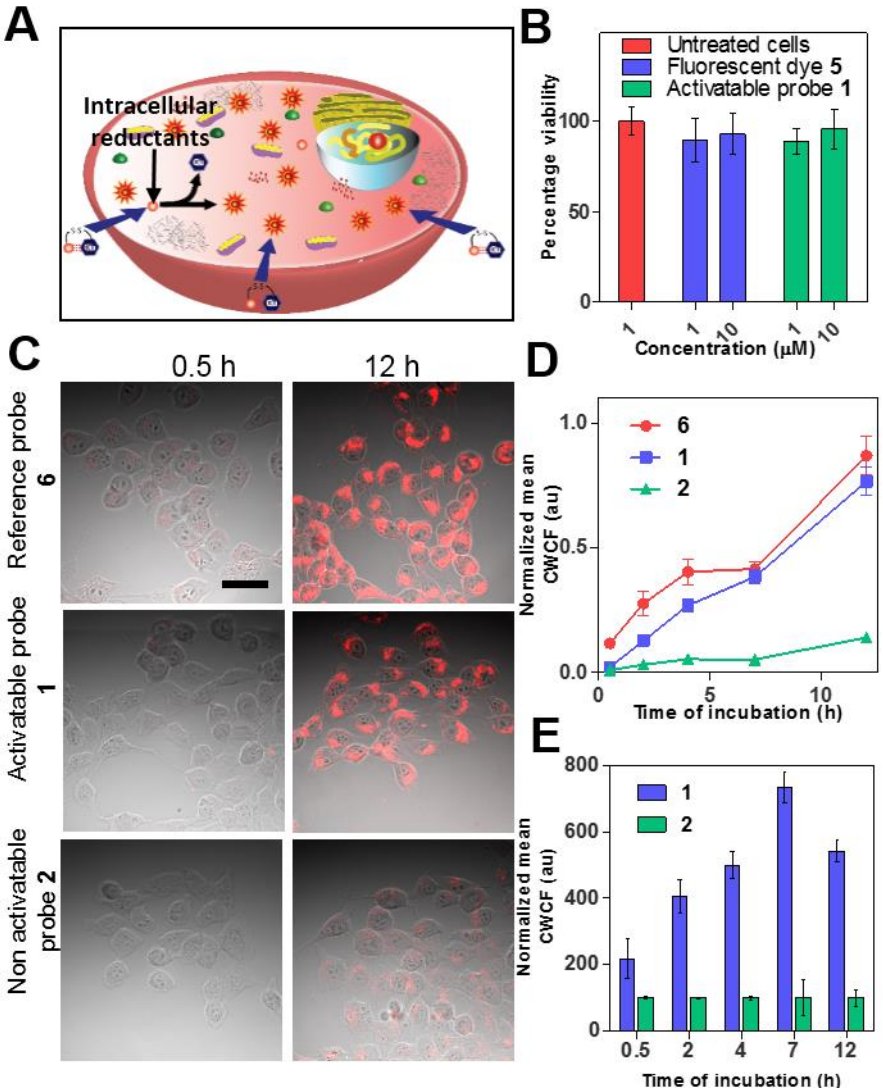

Figure 2-3: Cartoon representation of intracellular probe activation of 1. (B) Cytotoxicity assay for 5 and 1 (control = untreated cells). (C) Representative confocal fluorescence (red) images of 4T1-Luc cells treated with 10 μM 6, 1 and 2. (D) Time-dependent increase in normalized mean fluorescence emission from cells (corrected whole cell fluorescence (CWCF)) treated with the compounds. (E) Normalized fluorescence intensity for 1 and 2 at the same imaging time point. All data represent mean ± sem for at least three independent experiments. Scale bar: 50 μm.

redox potential.[49] Cytotoxic study with a non-radioactive cell proliferation assay did not show any detrimental effects of the fluorescent dye **5** and probe **1** on cell viability at the experimentally relevant concentrations (Figure 2-3B). Intracellular fluorescence was quantified by estimating the corrected whole cell fluorescence (CWCF) intensity profiles (Figure 2-3C). A plot of normalized mean CWCF vs. time for **6**, **1** and **2** showed a nearly linear increase in intracellular fluorescence

for **1** (Figure 2-3D). The non-Cu(II) containing reference compound **6** showed a non-linear enhancement of fluorescence emission. The non-activatable probe **2** showed a significantly relatively slow and small increase in fluorescence over time. CWCF for **1** was 2, 4, 5 and 7.4 and 5.4 fold higher than that of **2** at 2 h, 4 h, 7 h and 12 h respectively (Figure 2-3E).

2.3.5. Lifetime changes associated with probe activation

Although the increase in fluorescence emission is necessary to indicate probe activation, several other factors can affect intracellular fluorescence measurements, including the rate of internalization, local concentration of the molecules and stability of Cu(II)-DOTA chelate. To minimize this variability, we explored the application of fluorescence lifetime changes associated with probe activation by using fluorescence lifetime imaging microscopy (FLIM). Because FLT is less dependent on changes in the probe concentration, it can more accurately report the effects of molecular perturbation in a heterogeneous medium than fluorescence intensity measurements. Representative FLIM images of 4T1-Luc cells treated with 6, 1 and 2 are shown in Figure 2-4A. We calculated the mean FLTs at each time point by taking the mean from the histogram of FLTs for the corresponding image. Unlike the mean FLT of 6, which showed no significant variation with time, the mean FLT value of 1 remarkably increased from ~700 ps almost linearly over time before reaching the maximum value of >1000 ps at 7 h (Figure 2-4B). Comparatively, a much lesser variation was observed for mean FLT of 2. For further validation, we obtained global decay curves for individual compounds by treating the imaging field of view as a single pixel. Representative global decay curves reflect faster decays for probes 1 at 2 h and 2, while slower decay for 1 at 12 h and 6, as observed with mean FLTs calculated (Figure 2-4C). Any increase in FLT of 2 can be attributed to lose of Cu(II) from the chelator under intracellular conditions such

as trans-chelation with cellular proteins. Together these findings indicate that cleavage of disulfide bond induces the observed fluorescence increase in cells treated with 1.

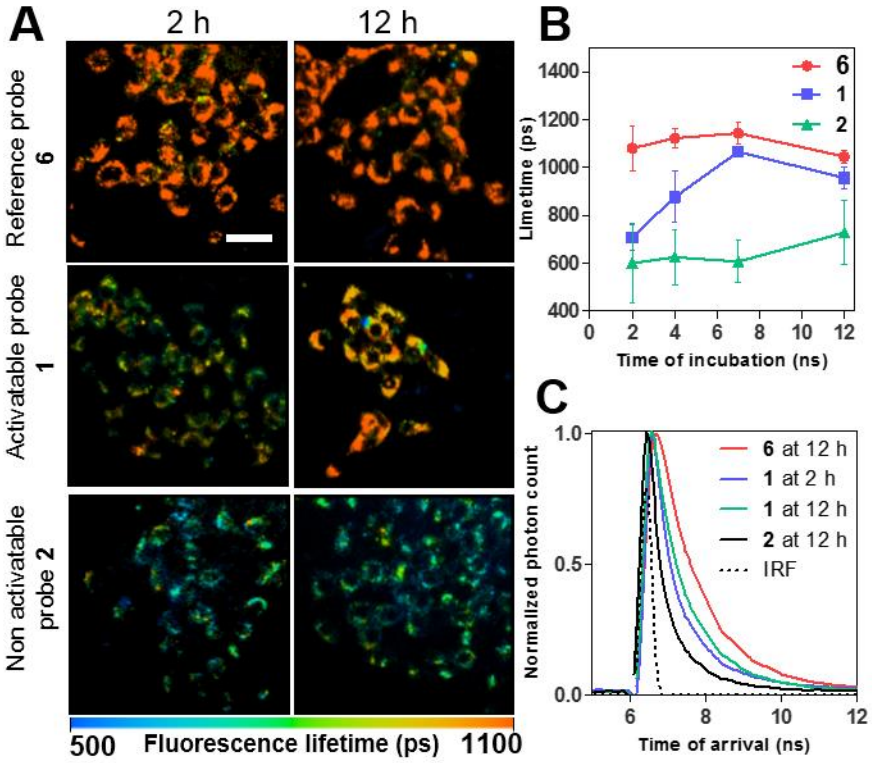

Figure 2-4: (A) Representative images from fluorescence lifetime imaging microscopy of 4T1-Luc cells treated with 6, 1 and 2. (B) Time dependent changes in FLTs (mean ± sem for at least three independent experiments) of 6, 1 and 2 in 4T1-Luc cells. (C) Representative global decay curves for 1, 2 and 6. IRF: Instrument response function. Scale bar: 50 µm.

2.3.6. *In vivo* imaging

Finally, we explored the *in vivo* behavior of the activatable probe 1 in tumor bearing mice. We hypothesized that the high intracellular reducing environment of tumor cells will facilitate rapid fluorescence activation in tumors. We injected equimolar quantities of 1, 2, and 6 in 4T1-Luc tumor bearing mice. Representative whole-body dorsal images are shown in Figure 2-5. Compound 6 rapidly distributed throughout the body, with high whole body fluorescence. In contrast, fluorescence in mice treated with the non-cleavable compound 2 was significantly low. Activatable

probe 1 showed a time-dependent increase in whole body fluorescence, with high tumor-to-background signal. We attribute the rapid increase in 4T1-Luc tumor fluorescence to higher permeation and activation of 1 in the tumors.

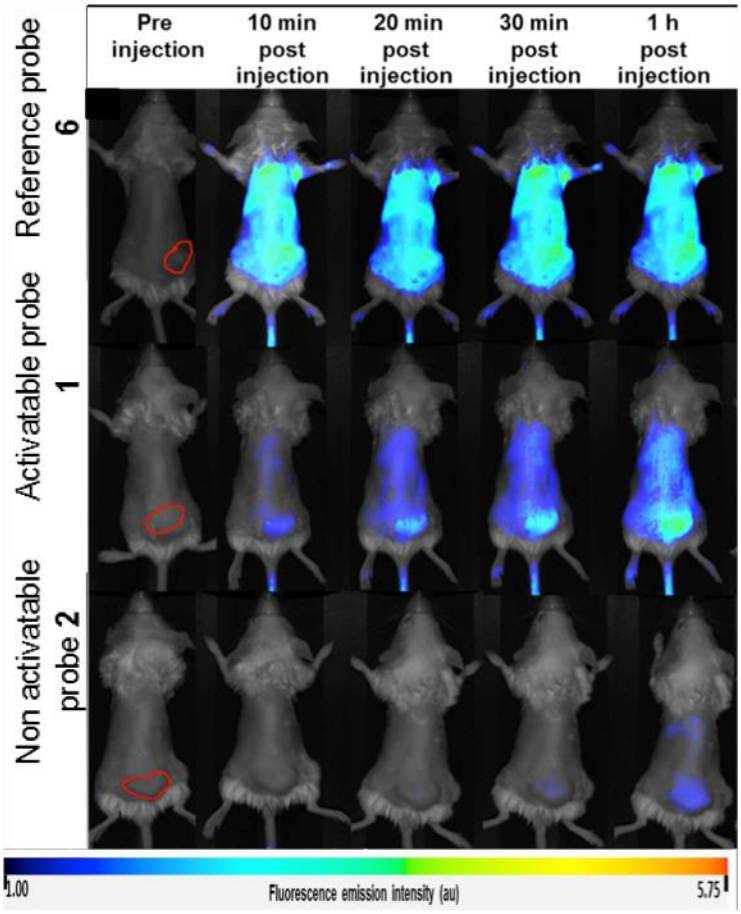

Figure 2-5: *In vivo* imaging of cancer with molecular probes in mouse xenograft models of cancer. Representative whole body (dorsal) fluorescence images of 4T1-Luc tumor bearing mice injected with 6 (top), 1 (middle) and 2(bottom). Red circle indicates the tumor region.

2.3.7. Distance dependence of quenching efficiency

The spectral overlap between the emission spectra of the fluorescent dyes tested and the absorption spectra of copper(II) ions indicates that FRET may play a major role in the fluorescence quenching mechanism [Figure 2-6a]. As distance dependence is characteristic of FRET, we studied the distance dependence of the fluorescence quenching by copper (II) ions. For this purpose we used

constructed a library of probes by flanking a NIR dye LS641 and chelated copper (II) by varying lengths of rigid polyproline linkers. Fluorescence quenching efficiency and fluorescence lifetime were found to decrease rapidly with increasing distance between dye and quencher as expected from FRET induced quenching.

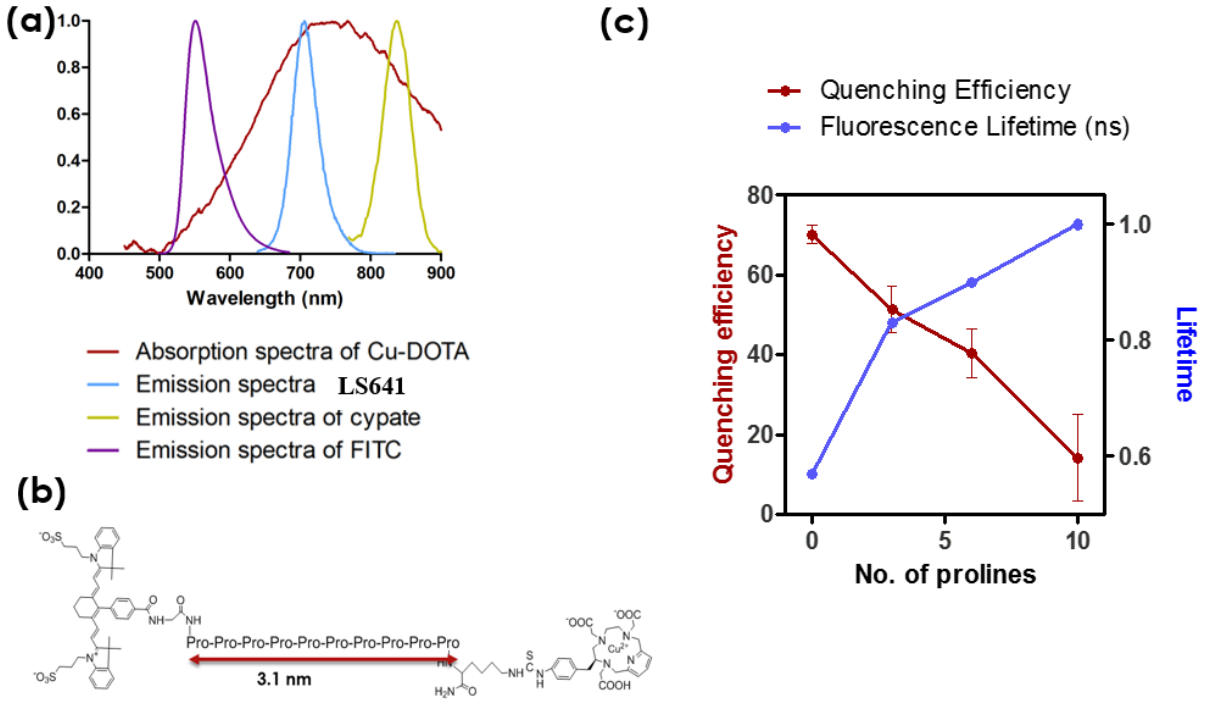

Figure 2-6 (a) Spectral overlap between Cu(II) –DOTA and fluoresce cent used in the activatable probes dyes indicate existence of FRET interaction. (b) Polyproline linker was used a rigid linker to create varying distance between the dye and quencher (c) Both quenching efficiency and quenching induce decrease in fluorescence lifetime shows heavy distance dependence.

2.4 Discussions

A major limitation of optical molecular imaging is the absence of efficient, versatile, and biocompatible fluorescent activatable molecular probes which can provide high signal to background contrast without longer wait times for imaging. This problem is exacerbated by the scarcity of an efficient, non-fluorescent and versatile quencher molecule for fluorescent dyes in the NIR region, which is essential for deep tissue and *in vivo* optical imaging. Application of Cu(II) as a universal fluorescence quencher is attractive for molecular imaging be-cause it provides a

modular approach for the synthesis of visible and NIR molecular probes. Its dual photoinduced electron transfer and FRET based fluorescence quenching mechanisms create a versatile quenching platform that is not entirely dependent on spectral overlap or distance between the fluorescent dye and the quencher. Since Cu(II) is a non-fluorescent quencher, interference with imaging signal is not a concern, facilitating the detection of fluorescence with high sensitivity. Moreover, the molecular weight of chelated Cu(II) is relatively small, which minimizes steric effect that hinders molecular recognition of cleavable domains in conventional activatable probes. Together, these features favor the use of Cu(II) to develop rapid and selective activatable probes for interrogating molecular processes in cells and living organisms.

To demonstrate this strategy, we used two NIR fluo-rescent cyanine dyes (1 and cypate) and a visible fluorescent dye (FITC) to synthesize disulfide based Cu(II)-quenched activatable probes (Chart 1). We demonstrated that the same synthetic approach could be readily adapted to visible and NIR fluorescent dyes. The disulfide bond is readily cleavable under the intracellular reducing conditions of cancer cells. The modular nature of the synthesis allows the use of other biologically relevant cleavable domains, such as enzyme cleavable peptides, for monitoring the functional status of diagnostic enzymes. Spectroscopic studies showed high fluorescence quenching efficiencies (>70%) when Cu(II) was present in an equalmolar ratio as the dye (Table 1). Attaching multiple Cu(II) ions to one dye molecule gave higher quenching efficiencies (>90%). These quenching efficiencies are significantly better than previously reported for molecular beacon constructs, which achieved 85% quenching efficiency in the presence of 50 fold excess of free Cu(II).20 We further supported these results by measuring the decrease in FLT of the molecular probes before and after incorporating Cu(II) (Table 2). Both fluorescence emission and FLT were recovered after disulfide cleavage *in vitro* and *in cellulo* in cancer cells. The lower concentration

de-pendency of FLT measurements allowed us to uncouple probe internalization from fluorescence activation in cells.

We successfully replicated our *in vitro* results *in vivo* in tumor-bearing mice, which showed rapid probe activation leading to enhanced fluorescence emission from the tumors. Our *in vivo* results suggest that the high permeability of the 4T1-Luc tumors facilitated the uptake and subsequent activation of 2 relative to the control compounds. We attribute the rapid increase in 4T1-Luc tumor fluorescence to higher activation of 2 in the tumors as well as greater permeation of 2 into the tumors.

We also demonstrated that the fluorescence quenching and associated decrease in lifetime are dependent on the distance between the fluorescent dye and chelated copper (II). This suggests a strong influence of FRET in the fluorescence quenching mechanism of copper (II). While this limits the applications of the strategy to short linkers, however, the existence of unique lifetime values with each construct will be still useful for identification and complementary reporting.

Our results indicate that using multiple Cu(II) chelates improves the fluorescence quenching efficacy and gives a further reduction in FLT of the probes. Therefore, a strategy to enhance contrast is to employ a dendrimer-based approach, where multiple Cu(II)-ions can be conjugated for quenching one fluorescent dye molecule. An alternative approach is to attach the disulfide based acti-vatable probe to a small tumor-targeting moiety, such as a tumor specific affibody or peptide. This will enhance tumor cell specific accumulation /retention of the activatable probes, facilitating selective and further enhanced fluorescence activation in tumor cells. Moreover, this approach can also eliminate high levels of activation of the probes in hepatic cells, as observed in the case of molecular probe 2. Coupling fluorescence emission intensity with FLT imaging can

delineate fluorescence activation from fluorescence enhancement arising from con-centration increase caused by cellular internalization and tumor tissue perfusion. Also, a more efficient and stable Cu(II) chelator can be used in the design of these activatable molecular probes to avoid the *in vivo* instability of Cu(II)-DOTA. We anticipate that the relevance of Cu(II) to other imaging modalities, such as nu-clear and Cherenkov luminescence imaging, can pave the way for multimodal imaging applications of Cu(II)-quenched fluorescent activatable molecular probes.

2.5 Conclusions

In summary, we successfully developed a novel, simple and unified strategy for designing activatable probes encompassing both visible and NIR fluorescent dyes. Significant fluorescence quenching and decrease in FLT were observed after Cu(II) chelation. Our results indicate that using multiple Cu(II) chelates further improves the fluorescence quenching efficacy and decrease in FLT, suggesting the potential use of multiple Cu(II) chelates to optimize quenching. Both fluorescence intensity and FLT were restored after disulfide-cleavage mediated dissociation of Cu(II)-DOTA chelates from the dye used in the *in vitro* studies. NIR activatable probe **1** showed time-dependent fluorescence intensity and FLT enhancement in cancer cells. The versatility of the simple Cu(II) chelate provides a new paradigm for designing novel activatable probes for imaging cellular and physiological processes across both visible and NIR spectral regions. Moreover, these probes are both emission intensity and lifetime-sensitive, which can be used for complementary reporting.

In the following chapter, we will describe an unusual chemical reaction that was discovered while working with cyanine dyes with cold copper (II) ions.

Chapter 3

Cu (II) catalyzed dimerization of cyanine dyes and their potential applications in biological imaging

3.1 Introduction

A few examples of cyanine dyes forming covalently linked dimers via chemically induced radical cations have been reported in literature.[50] In this chapter, we show similar behavior exhibited by some heptamethine and pentamethine dyes when present in aqueous buffer solutions. Particularly, we demonstrate this conversion is more pronounced in heptamethine dyes and is facilitated in the presence of excess Cu(II) ions. This phenomenon was discovered while working with the cyanine dye based fluorescent activatable probes in the preceding chapter, which required exposure of the dyes to Cu (II) ions in aqueous solution. We isolate these dimer molecules and show all of them exhibit preserved absorption with near zero emission indicating enhanced non-radiative relaxation. We confirm this by measuring and comparing photoacoustic signal generated by the monomer and dimer of a cyanine dye cypate. Finally, we demonstrate of feasibility of using these non-fluorescent dimer molecules as a photoacoustic contrast agents in vivo. We use the dimer of LS301[51], a tumor targeting bioconjugate of cypate for in vivo photoacoustic imaging in tumor bearing mice. Photoacoustic imaging part of this study was done in collaboration with Dr. Chulhong Kim, Seung-Hyun Lee and Dayoon Kang at Postech, South Korea.

3.2 Materials & Methods

3.2.1 Synthesis of cyanine dye dimers

Solutions of cyanine dyes (0.1 - 1mM) were prepared in 10% organic solvent (DMSO or DMF) in 0.1 M ammonium acetate buffer, pH 5.5. Copper (II) chloride (5- 10 fold excess) was added to this solution and incubated at room temperature or at 70°C for 1-24 h to make the respective cyanine dye dimers. The crude were purified by HPLC equipped with a reverse-phase C-18 column and the final product was characterized by mass spectrometry (MS-ESI).

3.2.2. Spectroscopic characterization

We measured and compared the optical properties of the dyes and their monomers probes in methanol, water and dimethyl sulfoxide (DMSO). The absorption spectra were measured on a DU 640 spectrophotometer (Beckman-Coulter, Brea, CA). Fluorescence emission spectra were recorded on a FluoroLog 3 spectrofluorometer (Horiba Jobin Yvon, Edison, NJ) using 620 nm/635-900 nm, 690nm/705-900, and 720 nm/735-900 nm, as excitation/emission wavelength with 5 nm slits for molecules containing cypate-3, HITC, and cypate respectively.

3.2.3. Photoacoustic imaging

Photoacoustic amplitude of cypate and its dimer were measured at concentrations 6.5-200 µM in 10% DMSO in water. For in vivo imaging a 150 µl of 200 µM solutions of LS301 dimer was injected into two A549 tumor bearing mice. The mice were imaged at 6 h, 12 h and 24 h after injection using a system as described before36. Images were acquired at excitation wavelengths 800 nm and 890 nm.

3.3 Results

3.3.1. Molecular characterization

Figure 3-1 shows the pentamethine and heptamethine dyes used to synthesize respective dimers.

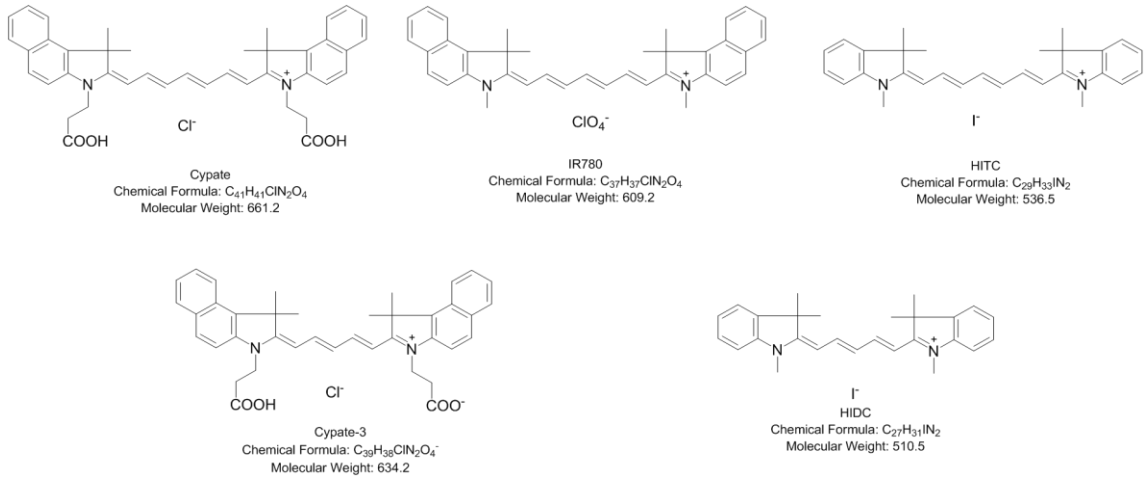

Figure 3-1: Chemical structures of cyanine dyes which demonstrate Cu(II) facilitated dimerization

We isolated and characterized cypate dimer using high resolution mass spectrometry and high resolution 2D NMR analysis as follows:

a. High resolution mass spectroscopy of cypate dimer

The full mass spectra are shown in Figure 3-2. Expansion of the peak show the corresponding to a molecular formula of $C_{82}H_{79}N_4O_8$, which is double of the monomeric mass of cypate ($C_{41}H_{41}N_2O_4$) with the loss of 2 protons [Figures 3-3, 3-4 and 3-5].

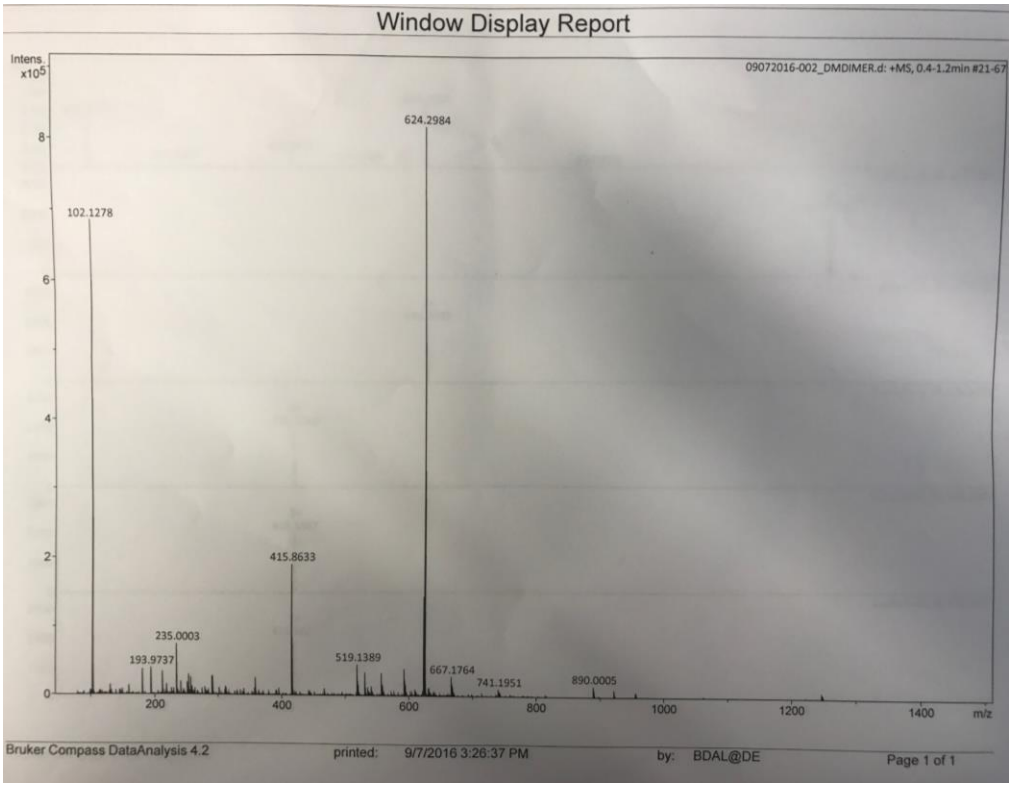

Figure 3-2: Observed HMRS spectra for the dimer compound.

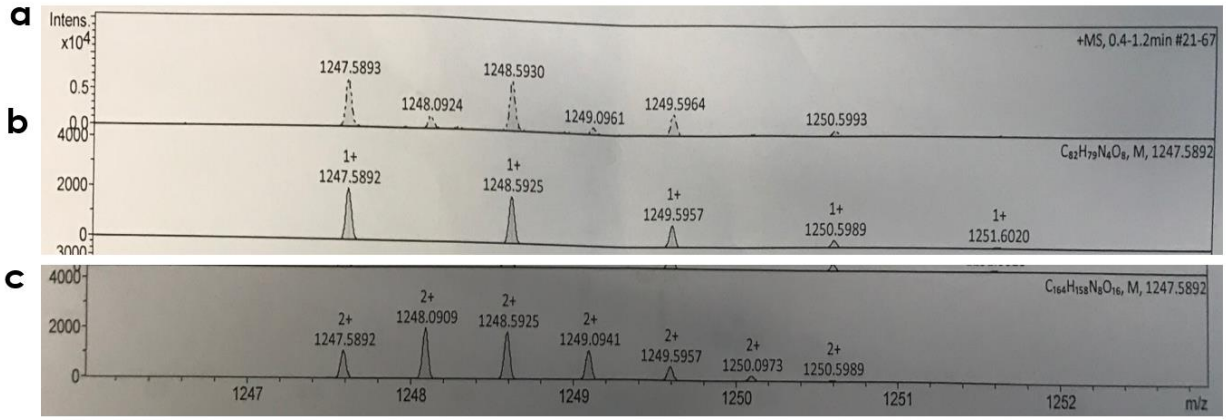

Figure 3-3: Expanded region of $[M+H]^+$. (a) Observed spectra. (b) Taller peaks observed correspond to $[M+H]^+$ for $C_{82}H_{79}N_4O_8$. (c) Smaller peaks observed correspond to $[M+2H]^+$ for a dimeric form of $C_{82}H_{79}N_4O_8$.

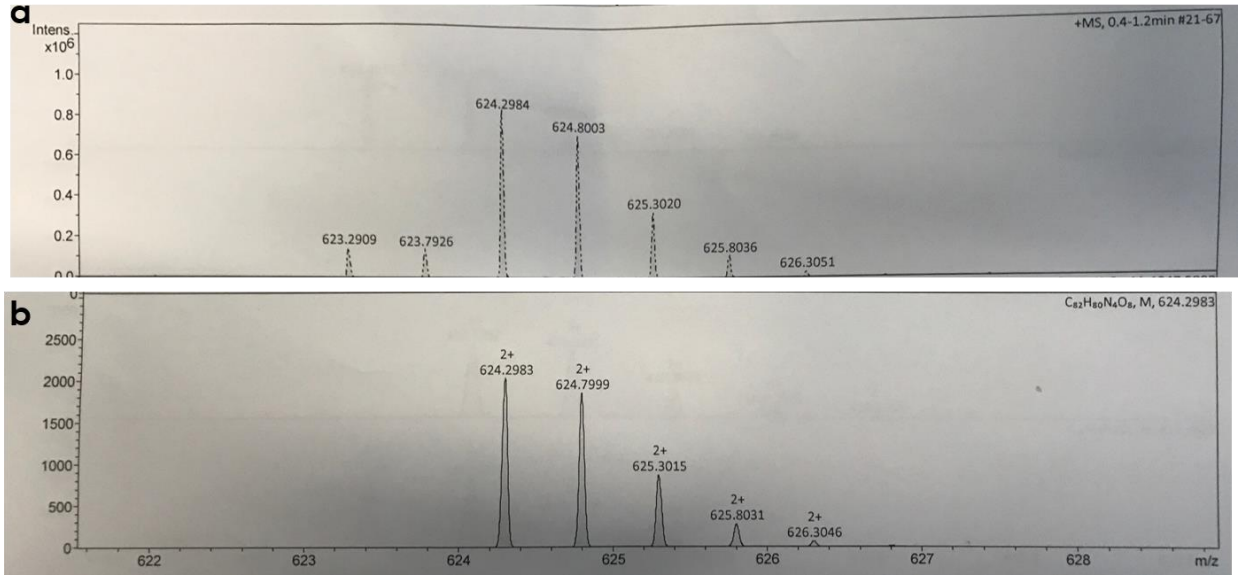

Figure 3-4: Expanded region of $[M+2H]^+$. (a) Observed spectra. (b) Peaks observed correspond to $[M+2H]^+$ for $C_{82}H_{79}N_4O_8$.

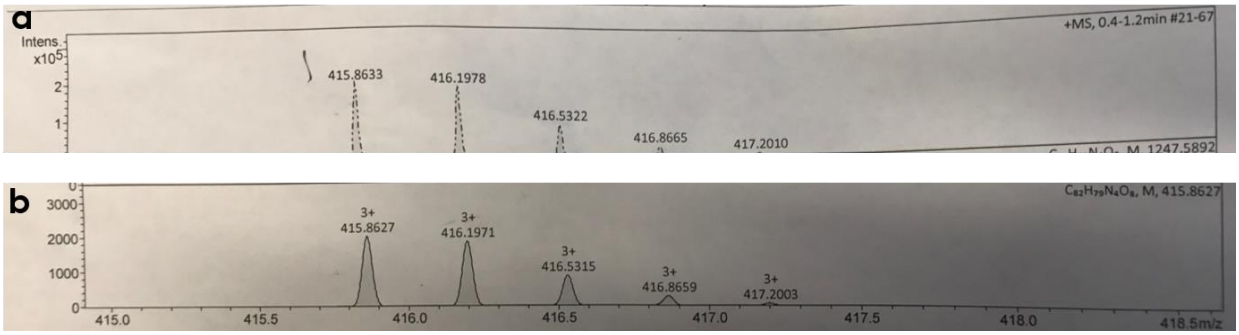

Figure 3-5: Expanded region of a peak at ~415.(a) Observed spectra. (b) Peaks observed can be attributed to the $[M+3H]^{3+}$ for $C_{82}H_{76}N_4O_8$, i.e., to the species for after loss of 2 protons from the molecule for $C_{82}H_{79}N_4O_8$.

Mass spectra of the other dye tested show similar properties, indicating similar phenomena.

- IR780: $[M+H]^+$ = 509.3 (predicted), 509.5 (observed). IR780 Dimer: $[M+H]^+$ = 1015.6 (predicted), 1015.8 (observed).

- HITC: $[M+H]^+$ = 409.3 (predicted), 409.4 (observed). HITC Dimer: $[M+H]^+$ = 815.5 (predicted), 815.7 (observed).

- Cypate-3: $[M+H]^+$ = 599.3 (predicted), 599.5 (observed). HITC Dimer: $[M+H]^+$ = 1195.6 (predicted), 1195.8 (observed).

- HIDC: $[M+H]^+$ = 383.2 (predicted), 383.4 (observed). HITC Dimer: $[M+H]^+$ = 763.5 (predicted), 763.7 (observed).

b. NMR analysis of cypate dimer

Figure 3-6 shows the numbering system used for NMR analysis of cypate and its dimer.

Proton integration for cypate spectra indicates there are seven protons in the polymethine chain of

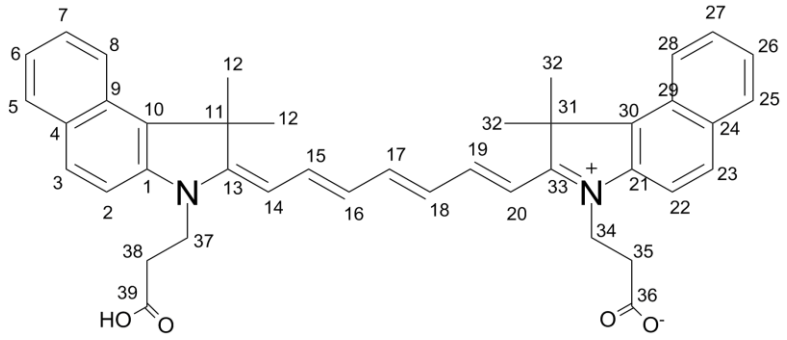

Figure 3-6: Numbering of protons and carbons on cypate for use in NMR analysis

cypate [Figure 3-7]. Overlapped protons H14-H20, H15-H19 and H16-H18 showed symmetrical polymethine chain structure. TOCSY experiment reveals continuous spin propagation from H14 to H20 in vinyl bridge [Figure 3-7]. HMQC H1-C13 correlated resonances indicated seven C-H carbons in the polymethine chain [Figure 3-8].

In comparison, the polymethine chain in the dimeric molecule displays an unsymmetrical structure, particularly with H20 showed an upfield shift of 1.2 ppm from H14 [Figure 3-9]. Proton H17 also showed a 0.5 ppm downfield shift as compared to Cypate H17 resonances. Furthermore, TOCSY resonances in dimer breaks to two sections of spin propagation, H19 -H20 and H14 – H17

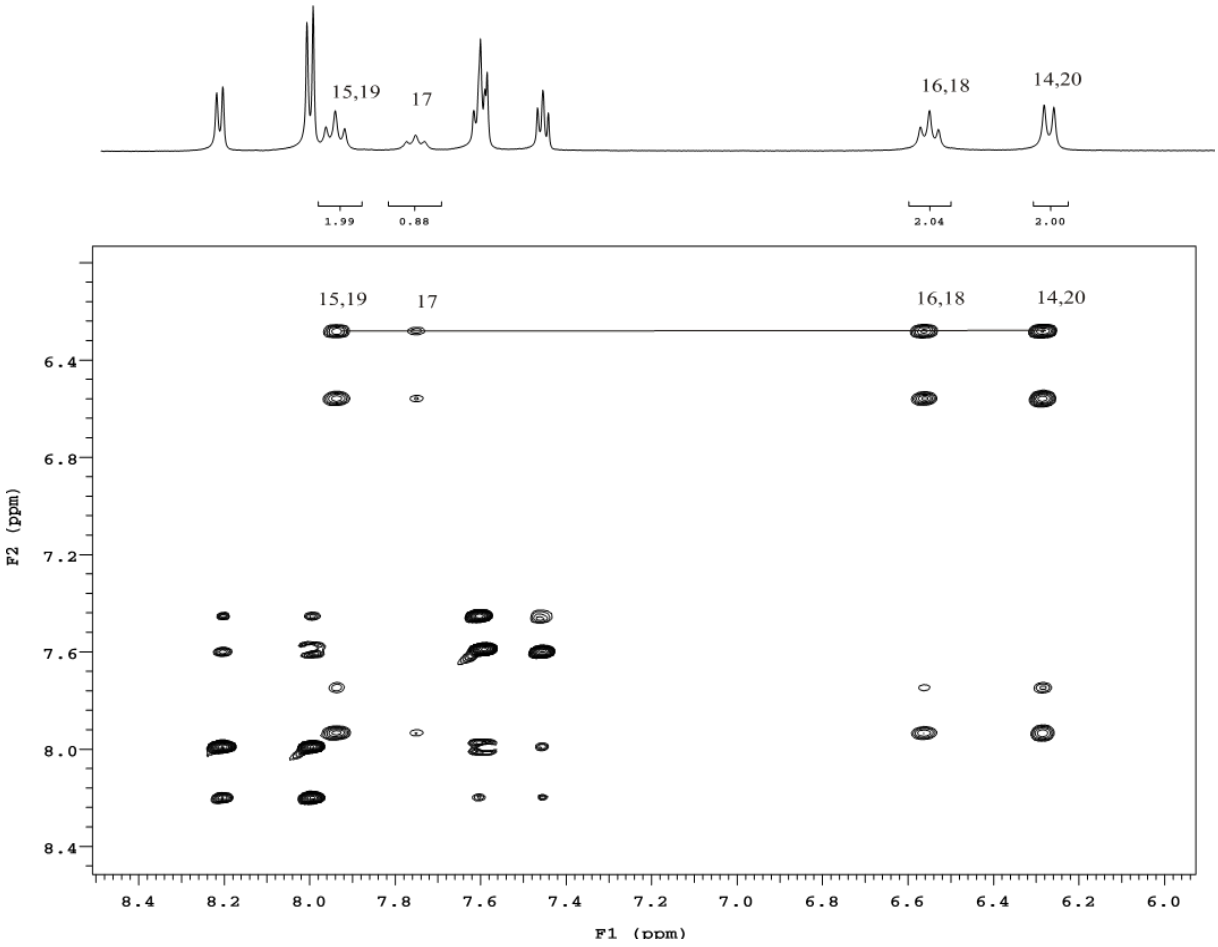

Figure 3-7: TOCSY spectrum of Cypate vinyl bridge in DMSO-d6.

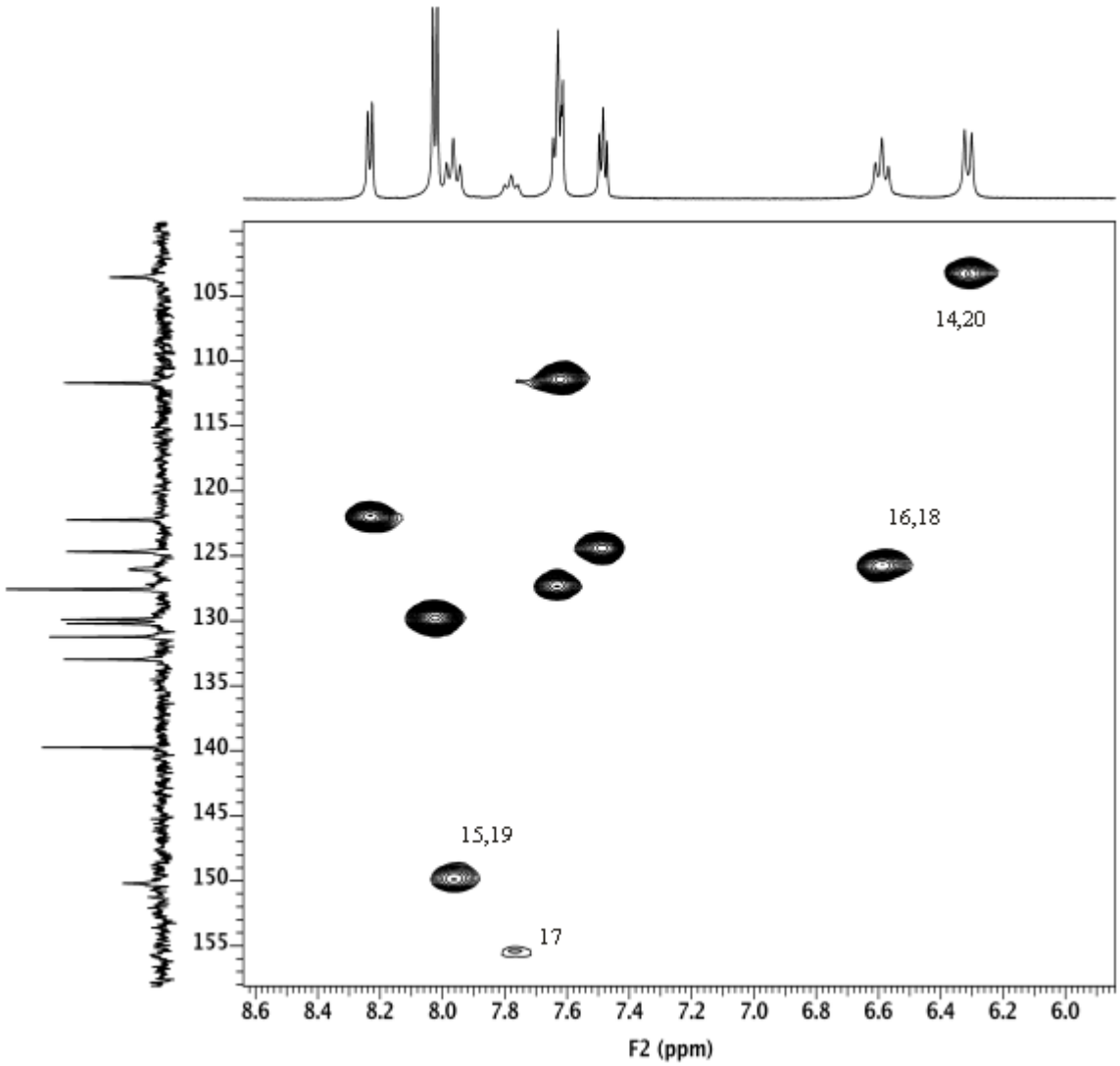

Figure 3-8: HMQC spectrum of Cypate in DMSO-d6.

with the absence of H18 [Figure 3-9]. Quaternary carbon C18 was confirmed by the absence of H1-C13 correlation in HSQC [Figure 3-10]. Moreover, multiple bonds correlations between C18 and H16, H17, H19 and H20 in HMBC indicating C18 is still residing in the chain and the substitution of H18 may contribute to the formation of Cypate-dimer. A full spectrum of C13 assignments are shown in Figure 3-11.

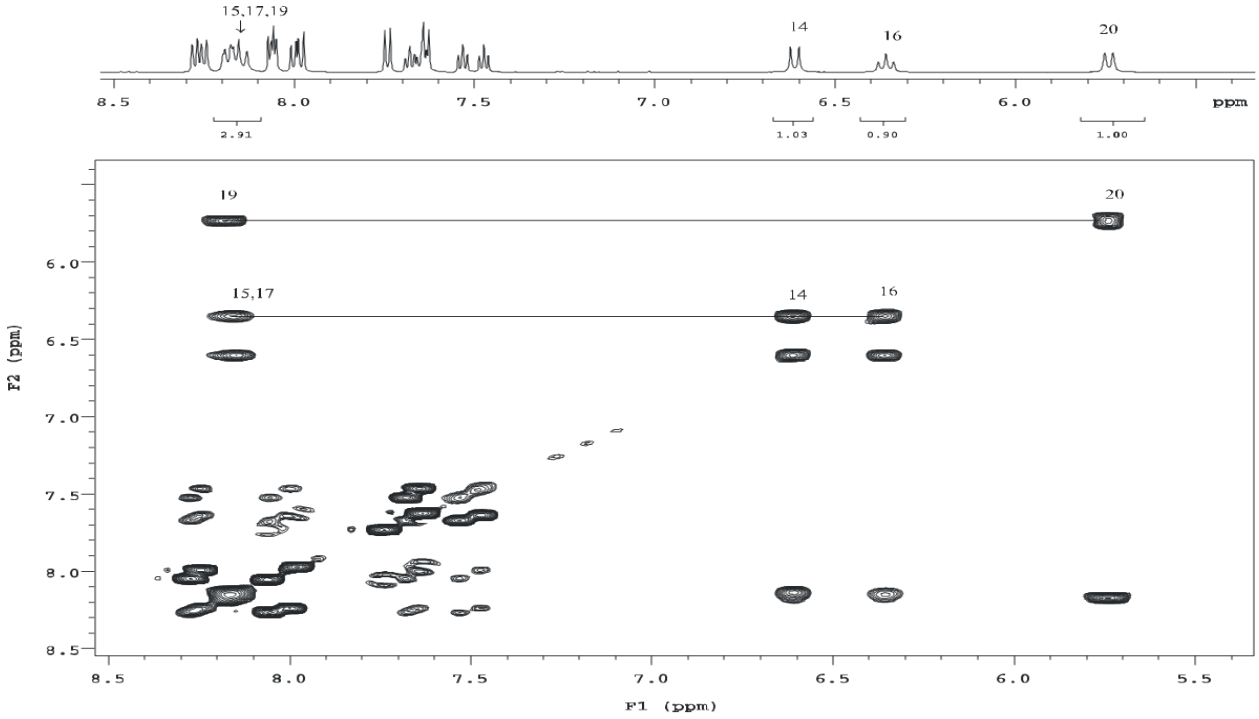

Figure 3-9: TOCSY spectrum of Cypate-dimer in DMSO-d6.

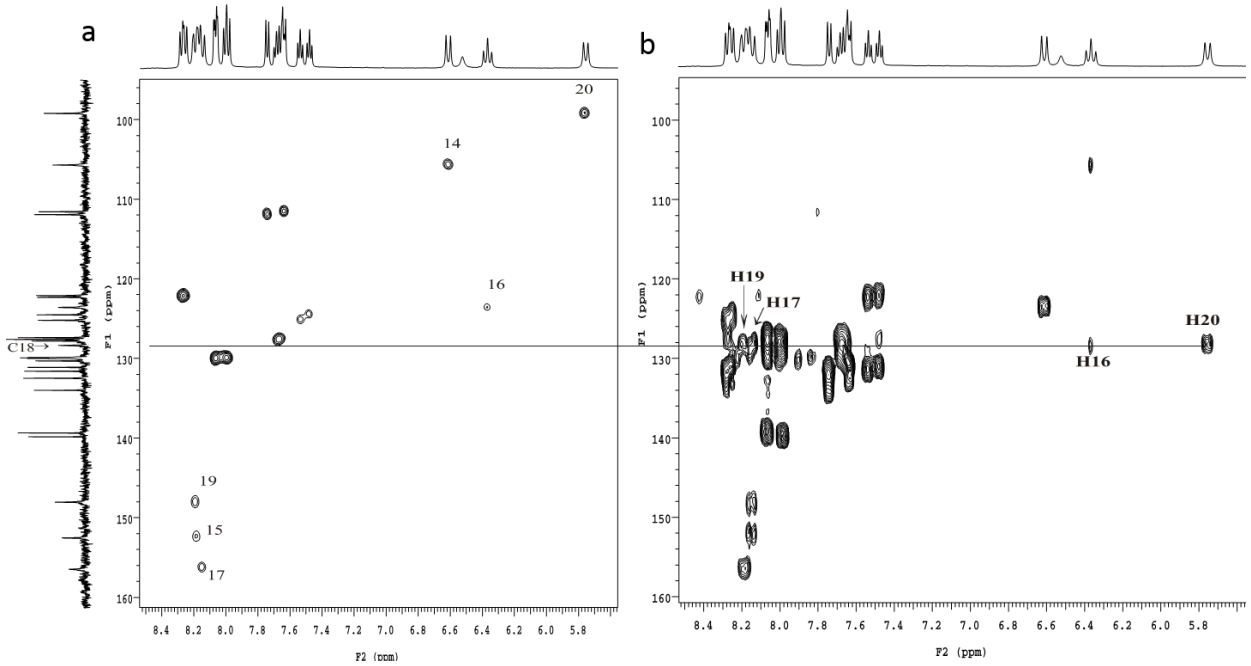

Figure 3-10: HSQC(a) and HMBC(b) spectra of Cypate-dimer in DMSO-d6.

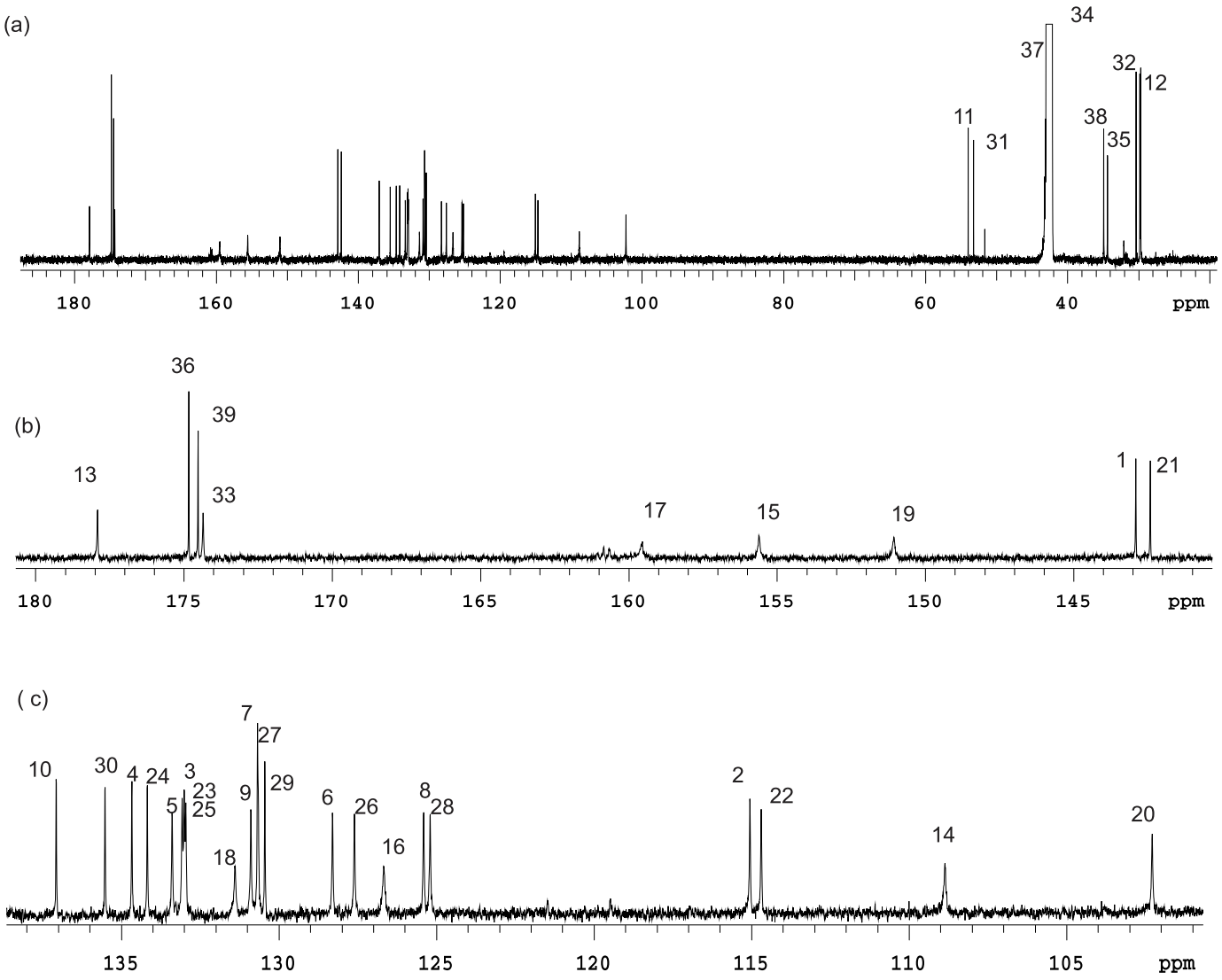

Figure 3-11: C13 assignments of Cypate-dimer in DMSO-d6. (a) Full spectrum. (b,c) Expanded region of aromatic regions.

NMR and HRMS data indicates the formation of a new C-C between two cypate monomers by the loss of two protons. NMR predicts the position of this new bond to be between the C18s of respective dimers, indicative of the structure as shown in Figure 3-12.

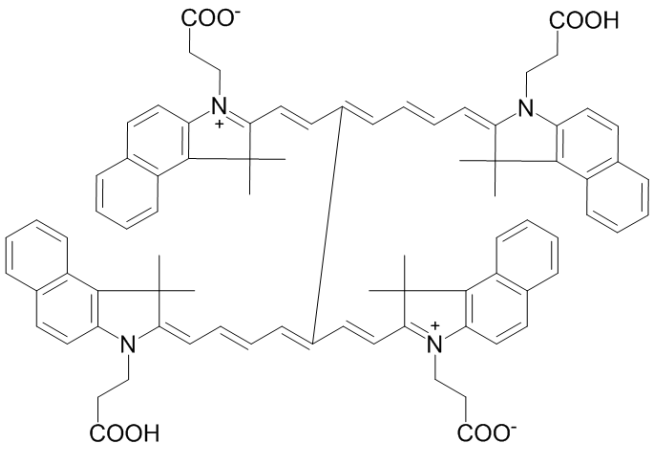

Figure 3-12: Structure of Cypate Dimer

3.3.2. Spectroscopic properties

The absorption spectra of all the dimeric molecules were very similar to that of the respective monomers [Figure 3-13]. There was a consistent hypsochromic shift of the peak absorption for ~3-5 nm, and relatively more pronounced aggregate peaks. . The molar extinction coefficient of cypate dimer was 1.7 times that of the monomer (measured in methanol). There was almost complete loss of fluorescence in all cases which is expected due to self-quenching.

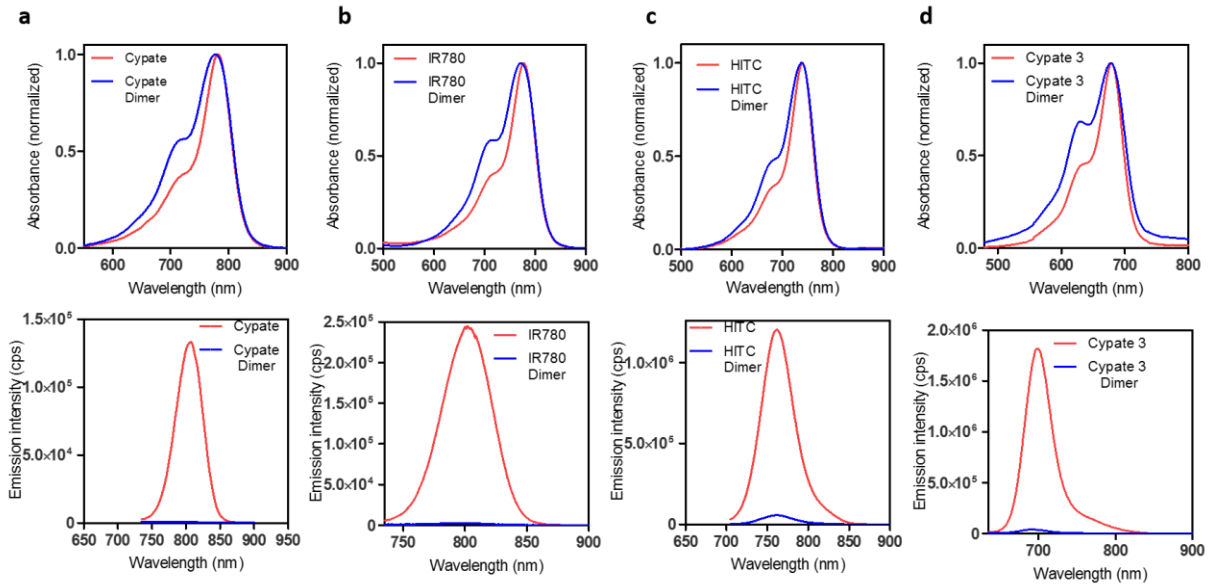

Figure 3-13: Absorption (top) and fluorescence emission (bottom) spectra of the dyes cypate (a), IR780 (b), HITC (c) , Cypate-3 (d) and their respective dimers.

3.3.3. Dimerization of heptamethine dyes is facilitated by Cu (II) ions.

The dimerization reaction for hepamethine dyes cypate, HITC and IR0780 were facilitated by the presence of Cu (II) ions. HITC showed highest yields (Table 3-1). Figure 3-a shows that dimerization of IR780 dye is greatly increased when an excess (10X) is present. Also, the dimerization process is not affected by the organic solvent DMSO or DMF used for enhanced solubilization of the dyes the dye into the aqueous buffer.

Table 3-1: Percentage yields of cyanine dye dimers in absence and presence of excess Cu (II)

	Cypate	**IR780**	**HITC**	**Cypate-3**	**HIDC**
No Cu(II)	12 %	5	32 %	< 1%	< 1%
+ Cu(II)	67 %	63%	80 %	< 1%	< 1%

3.3.4. Dimerization of cypate is pH independent:

The cyanine dye cypate has two acidic carboxyl groups. We tested if these groups affect the dimerization reaction. Figure 3-**14**b shows that dimerization at different pH shows that the reaction is pH independent. Because basic pH has been shown to degrade the dye molecules, the dimerization reaction could not be followed for long in basic conditions.

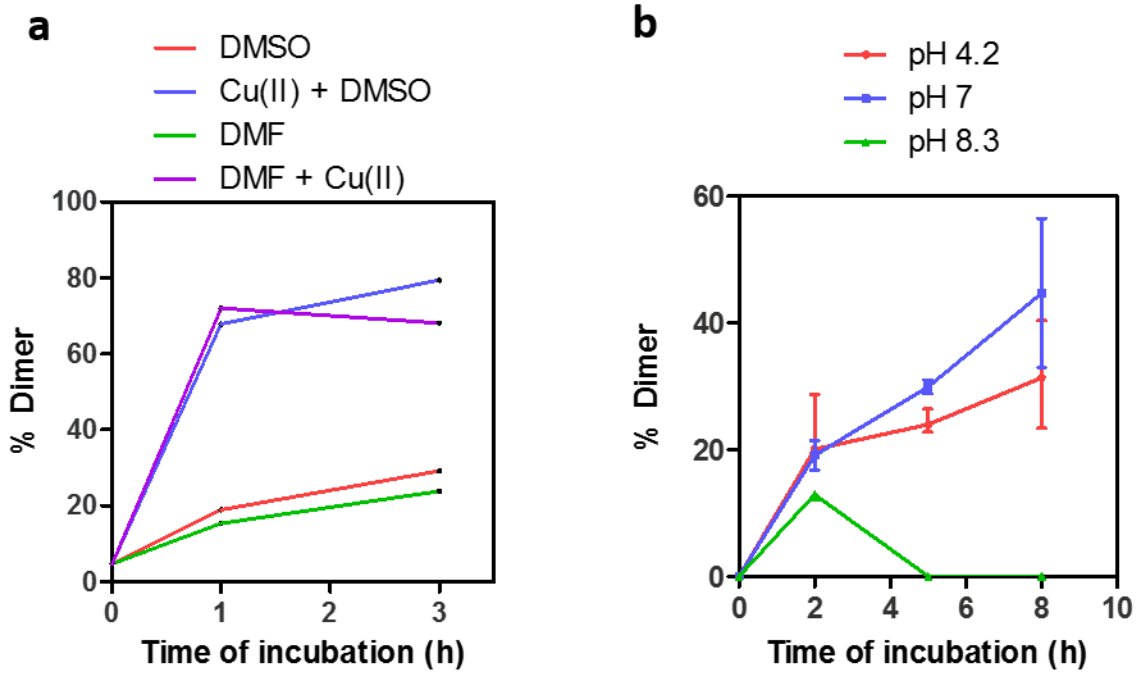

Figure 3-14: (a) Dimerization of HITC is facilitated in presence of excess Cu(II) ions and is independent of the organic solvent used for solubilizing the dye in the aqueous buffers. (b) Dimerization of cypate is independent on the pH (acidic vs. neutral). The dye degrades at basic pH so it is suitable for dimerization.

3.3.5. Photoacoustic imaging with cyanine dye dimers.

Absorptive molecules undergo both radiative (fluorescence) and non-radiative (vibrational and collisional relaxations) relaxations upon excitation. The non-radiative relaxations coverts the excited state energy into heat which in turn increase in pressure and subsequent generation of acoustic waves. These acoustic waves can be detected when traveling to the surface, and used as

contrast for photoacoustic (PA) imaging [52]. Previous studies have shown experience with *in vivo* PA imaging with cypate and other NIR dyes has shown that free dyes do not produce sufficient PA signal at biologically relevant concentrations, while a much higher PA signal can be achieved when the molecules are at a quenched such as when incorporated on a nanoparticle[53]. We envisioned higher PA signals from cyanine dye dimers due to a combined effect of enhanced molar absorptivity and enhanced non-relative relaxations. The photoacoustic spectrum of cypate and its dimer shows greater PA amplitude of the dimer compared to the monomer at equimolar concentrations. (Figure 3-15a). Maximum PA absorption was detected at 800 nm for both molecules. At 200 µ M concentration, the dimer generated 3.6 times PA amplitude than the monomer (Figure 3-15b).

3.3.6. Photoacoustic imaging with cyanine dye dimers.

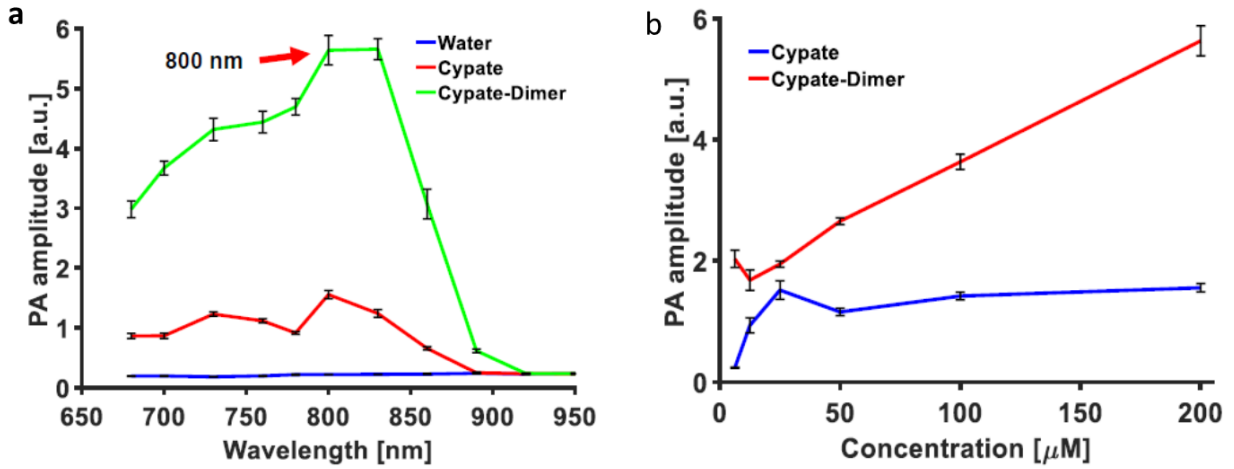

Figure 3-14: (a) Photoacoustic spectrum of cypate and dimer in 10%DMSO in water. (b) Concentration dependent PA amplitude.

We then tested feasibility to image tumors using PA contrast from molecularly targeted dimers. For this purpose, we used the dimer of a bio-conjugate of cypate (LS301 dimer) which has been shown to have highly specific in vivo tumor targeting capacity. When injected in to a A549 tumor bearing mouse, in vivo PA imaging shows time dependent enhancement of contrast in

liver and tumor areas of the mouse, demonstrating feasibility of using dimer molecules for in vivo. PA imaging (Figure 3-16).

3.4 Discussions

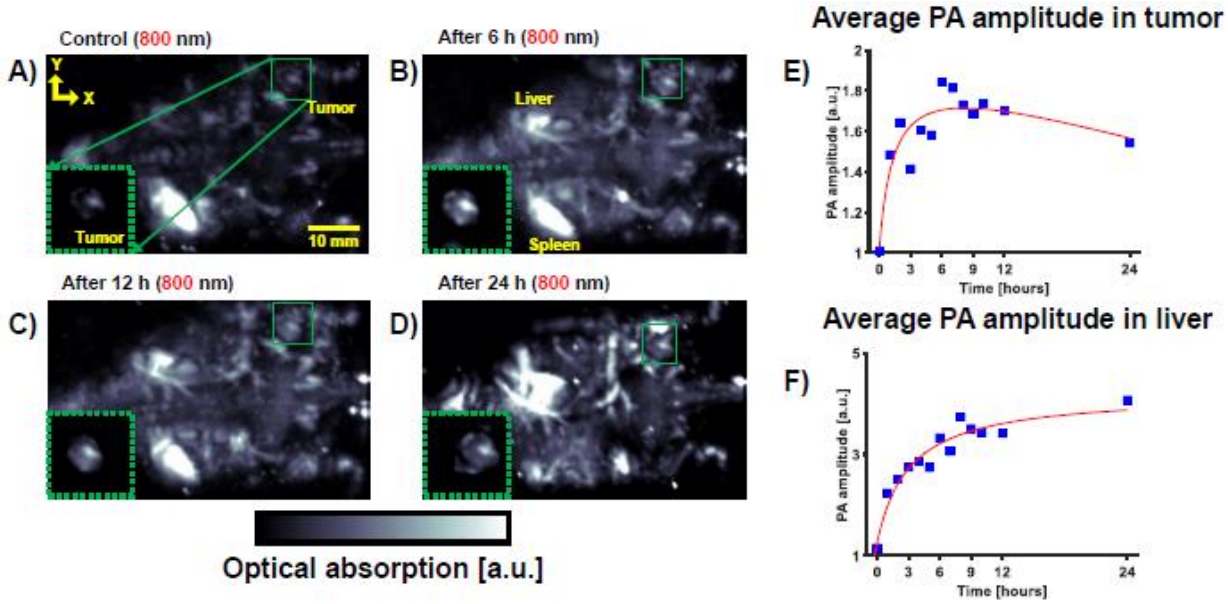

Figure 3-16: A549 tumor bearing mouse whole body PA images with LS301 dimers. (a)Control PA map image before injecting materials. PA images after injecting 200 µM of LS301 dimer after (b) 6h, (c) 12 h and (c) 24 h. Average PA amplitude in the (e) tumor region and (f) liver region over time.

While working with cyanine dyes and Cu (II) ions in solution in the preceding chapter, we observed that the later facilitates irreversible dimerization of these dyes. We show at least five cyanine dyes (and their bioconjugates) that demonstrate this phenomena. NMR and HRMS characterization of the dimer of cyanine dye cypate indicates the stable dimer has a new symmetric C18-C18 bond between the polymethine chains. Dimerization of few cyanine dyes have been reported earlier, and shown to be formed via oxidation and radical cation formation of the dye monomers.[50] The radicle cations then can dimerize and deprotonate forming the final irreversible dimer molecule. As observed in this study, presence of Cu(II) may facilitate oxidation of the dye monomers and stabilization of the intermediate cation, leading higher yield of the dimer. Spectroscopic studies showed higher molar absorptivity of the dimers and preservation of

absorption properties with the near complete loss of fluorescence. Loss of fluorescence leads to higher non-radiative relaxation of the excited molecules, which was manifested as enhanced photoacoustic signal generated by the dimer than the monomer. Cyanine dyes have been used photoacoustic contrast agents, we envisioned the cyanine dye dimers would be more potent photoacoustic contrast agents and showed feasibility of performing *in vivo* tumor imaging using the dimer of a tumor targeted bioconjugate of cypate. Future studies with this new class of molecules will test them as fluorescence quenchers and as fluorescent reporters for chemical processes that can revert the reaction.

3.5 Conclusions

We have synthesized, isolated and characterized dimers of some pentamethine and heptamethine cyanine dyes. We dimerization in aqueous solutions is favored in heptamethine dyes than pentamethine dyes under similar conditions. Also presence of Cu(II) ions in 5-10 fold excess facilitates dimerization in heptamethine dyes. We demonstrate feasibility of using these non-fluorescent dimers for generating photoacoustic contrast in tumor bearing mice.

In the preceding two chapters we have worked with fluorescent probes and stuSdied fluorescence quenching for developing activatable probes. In the next chapters we will demonstrate the development of a use a broad spectrum dual-emission fluorescent molecular probe and use it to estimate the depth of a fluorescent inclusion *in vitro* and *in vivo*.

Chapter 4

Dual emission fluorescent molecular probe for depth estimation

4.1. Introduction

Using light to evaluate disease is increasingly common for both preclinical and clinical applications[54]. This increase is partly due to advances in fluorescent molecular probes that have diverse emission wavelengths as well as the ability to bind specific biological structures[55,56]. Fluorescence method allows for real-time imaging without the use of ionizing radiation, and shows promise in translational applications such as intraoperative imaging[57,58]. Currently, planar optical imaging relies on the intensity of the fluorescent signal to determine the extent of the pathology[59]. Many factors can impact the relative intensity of a signal, including tissue optical properties, dye concentration, and depth of the overlying tissue. The ability to assess the extent of a biological structure, such as a tumor or blood vessels, using a fluorescent dye will improve disease detection and monitoring disease progression[60].

The challenge in determining the depth of a fluorescent signal stems from the ill-posed nature of the inverse problem. If the depth of a fluorescent object is known, we can readily correlate the intensity of the signal with the depth. However when the depth is unknown, there are insufficient parameters available that can describe the system in order to accurately calculate the depth based on the fluorescent signal. Approaches that have demonstrated depth resolution include analyzing the point-spread function of light[61], temporal based imaging[62], and structured illumination[63-65]. Currently, the mainstay of depth profiling is fluorescence molecular tomography (FMT)[66-70]. FMT uses source-detector pairs, and solves the inverse problem based on relative changes in light intensity. FMT has proven to be useful in depth profiling for both preclinical and clinical applications. However the complexity of solving the numerous equations makes it computationally expensive and less practical for some imaging applications, particularly those that require real-time feedback.

In an attempt to measure fluorescence depth in a less complicated manner, we investigated wide-field dual-wavelength imaging. Previous studies demonstrated the ability to depth-profile in a turbid medium by imaging at multiple wavelengths[71,72]. The intensity of the fluorescence light detected varies as a function of depth due to the attenuation of light at that wavelength in a specific medium. Light attenuation is dependent on the optical properties of the medium, μ_a (absorption coefficient) and μ'_s (reduced scattering coefficient). When imaging is conducted in the same medium at two different wavelengths, the attenuation coefficients are constant for each wavelength. The natural log of the ratio of the detected light at two wavelengths varies linearly with depth[73].

To implement this approach, we developed a dual emitting fluorescent molecular system consisting of two different fluorescent molecules covalently linked in a 1:1 molar ratio. Spectrally distinct signals are important to ensure non-overlapping signal collection. Our results demonstrate the feasibility of dual-wavelength imaging for determining the depth of blood vessels and characterizing the sub-surface depth of tumors *in vivo*.

Part of this work was done in collaboration with Jesse Lam and Bruce Tromberg and University of California, Irvine.

4.2 Materials & Methods

4.2.1 Synthesis and spectral characterization of dual fluorescence imaging agents:

The dual-wavelength fluorescent imaging agent LS903 was synthesized using cypate[74] and fluorescein isothiocyanate (FITC, Sigma). Briefly, an octapeptide with 6 proline residues flanked by glycine and lysine residues was synthesized on solid support using standard Fmoc chemistry. One of the free carboxylic acid group on the dye cypate was conjugated to the free N-terminal

amine on glycine. The product was cleaved from resin, deprotected, and purified by high performance liquid chromatography (HPLC). Fluorescein isothiocyanate (FITC) was conjugated to the free epsilon amine on lysine. The resulting product (LS903; Fig. 1a) was purified by HPLC and characterized by ESI-MS: m/z for $[M + H]^+$: 1,781.6 (calculated), 1781 (observed); $[M + 2H]^{2+}$: 891.3 (calculated), 891 (observed). To increase the water solubility and enhanced circulation in mice, PEG2000 (Laysan Bio, Inc.) was conjugated to the free carboxylic acid group of LS903, and the resulting product (LS904; Fig. 1a) was characterized by MALDI-TOF, which showed the expected uniform mass distribution around M = 3763.

For spectral characterization, the compounds were diluted in phosphate buffered saline (PBS, pH 7.4) containing 1% bovine serum albumin (BSA) to simulate the interaction of the molecules with proteins *in vivo*. Absorption spectra were measured on a DU 640 spectrophotometer (Beckman-Coulter, Brea, CA). Fluorescence emission spectra were recorded on a FluoroLog 3 spectrofluorometer (Horiba Jobin Yvon, Edison, NJ) using 475 nm/490-900 nm and 720 nm/735-900 nm as excitation/emission wavelength with 5 nm slits for FITC and cypate, respectively.

4.2.2 *In vitro* Imaging

All dyes were prepared in a 1% BSA in PBS prior to *in vitro* imaging. *In vitro* imaging was conducted using LS903 obscured by various materials layered on top. In our initial study, we used lunchmeat (turkey breast, Budding; 0.65 mm thick) to obscure a 32 μM LS903 sample in an Eppendorf tube. To obtain higher depth resolution we switched to silicone and plastic sheets of 0.254 mm and 0.13 mm thick, respectively (Mc. Master-Carr, Elmhurst, IL). Simulated vessels were created using polyurethane tubing 0.015” ID x 0.033” OD (Braintree Scientific, Braintree, MA), and LS903 was imaged at two different concentrations (25 and 50 μM) for vessel studies.

All dual-wavelength imaging was conducted using the Optix MX3 system (ART Advanced Research Technologies, Montreal, CA) with excitation and emission wavelengths at 480/535 nm for the FITC channel, and 785/810 nm for the cypate channel. Normalized fluorescence was used for dual-wavelength image analysis, with the fluorescence signal normalized by the excitation power for each pixel. Image analysis was conducted using custom developed code in MATLAB® (The Mathworks, Inc., Natick, MA).

4.2.3 *In vivo* Imaging

All mouse studies were conducted in compliance with the Washington University Animal Welfare Committee's requirements for the care and use of laboratory animals in research. Balb/c mice were injected with 1 x 10^6 4T1 murine breast carcinoma cells on the flanks and the resulting subcutaneous orthotropic tumors were allowed to grow until they were approximately 10 mm in diameter. Mice were shaved prior to injection and imaging. The Optix was used to acquire tumor fluorescence for dual-wavelength analysis, and the Pearl small animal imaging system (Licor, Lincoln, NE) for NIR-specific analysis. For intra-tumor injections (n = 3), LS903 was prepared in a 1% mouse serum albumin (MSA) solution in PBS, for a final dye concentration of 60 μM in 20 μL of solution per tumor. For intravenous injections (n = 2) LS904 was prepared in a 1% MSA in PBS, for a final dye concentration of 60 μM in 100 μL of solution per mouse. Animals were imaged both before and after injection for intra-tumor injections, and at 0, 2, and 4, hours post injection for intravenous injections. The maximum *in vivo* contrast was detected at 2 hours post injection, and images at this time point were used for depth analysis.

4.2.4 Optical Parameter Measurement

White silicone rubber sheets 0.010, 0.015, and 0.020 inches in thickness (86435K121, 86435K13, and 86435K15, respectively, McMaster-Carr, Elmhurst, IL) with 35A durometer were divided into

2x2 inch sections. Three samples per thickness were measured using a custom integrating sphere setup (Beckman Laser Institute, University of California, Irvine, CA). By placement of the samples at the entrance or exit ports of an integrating sphere (4P-GPS-033-SL, Labsphere, North Sutton, NH), transmittance and reflectance values were measured using a broadband light source (HL2000 20W Quartz-Tunsten-Halogen lamp, Ocean Optics, Winter Park, FL), and spectrometer (Prime-X, B&W Tek, Newark, DE). Optical properties from 500 to 1000 nm were calculated with a MATLAB-based (MathWorks, Natick, MA) inverse adding-double algorithm (IAD) assuming a refractive index of 1.43, and anisotropy factor of 0.9. In brief, given transmittance and reflectance values, the IAD algorithm obtains absorption and scattering properties by iteratively solving the radiative transport equation until transmittance and reflectance values are matched[75].

4.3 Results

4.3.1 Structures and optical properties of dual fluorescent dyes

(Figure 4-1a) shows the structures of LS903 and LS904, with red and green colors representing the NIR and visible fluorescent dyes cypate and fluorescein, respectively. The absorption spectrum of LS903 showed the existence of both the cypate and FITC moieties (Figure 4-1b). FITC peak emission was at 518 nm (Figure 4-1c) and cypate peak emission was at 812 nm (Figure 4-1d). The presence of two distinct fluorescent peaks allowed for imaging at dual-wavelengths, which was used to calculate the depth of the fluorescent signal.

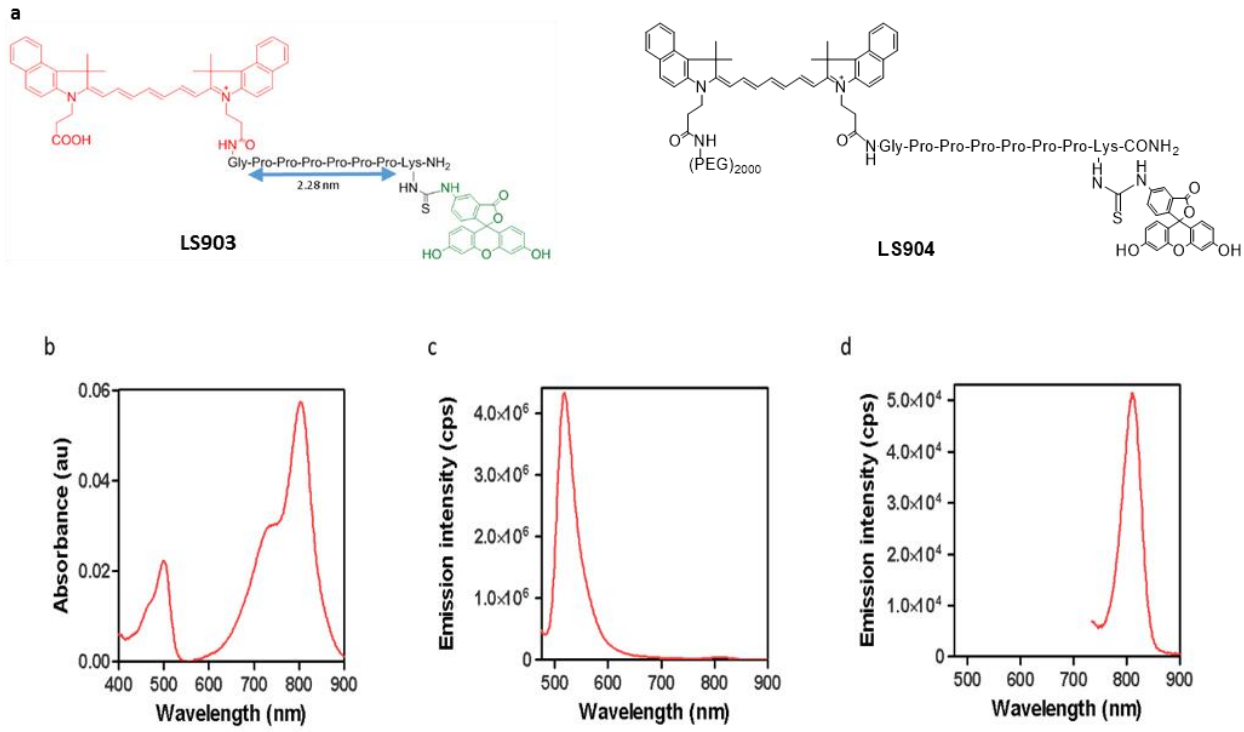

Figure 4-1: Properties of dual fluorescent dyes. (a) Molecular structure of LS903 and LS904; (b) absorption spectra of LS903; and emission spectra of LS903 at (c) 460 nm and (d) 720 nm excitation. All spectra were taken in a solution of 1% BSA in PBS, pH 7.4.

4.3.2 Simulation of *in vitro* tissue depth estimation

Description of tumor depth involves multiple depths that are of clinical significance. In the case of intraoperative imaging, the distance from the edge of the tumor to the edge of the healthy tissue is important in margin determination in the vertical direction. This distance is analogous to the sub surface depth (d_{ss}) when delineating the tumor margin in the z-direction (Figure 4-2a), or locating the depth of a fluorescent vessel under a tissue surface. There is also a depth of the tumor itself (d_{obj}), and the overall depth of the tumor from the surface of the tissue (d_{total}). The d_{total} depth is important in tumor staging for malignancies that invade deeper structures. For our analysis we quantified the signal from dual-wavelengths as a function of depth to determine the d_{ss} for the application of *in vivo* tumor margin estimation, and *in vitro* simulated vessel depth determination.

We obscured a solution of LS903 in a 1.5 ml Eppendorf tube under an increasing number of lunchmeat slices to represent increasing depth of a fluorescent inclusion below the surface. Figure 4-2b shows the NIR signal (cypate) was visible at greater depths than the signal in the green channel (FITC). We plotted the signal for each channel vs. depth (Figure 4-2c). The natural log of the ratio was plotted as a function of depth (Figure 4-2d), and the linear equation of the relationship was obtained (slope = 3.44, y-int = -0.27).

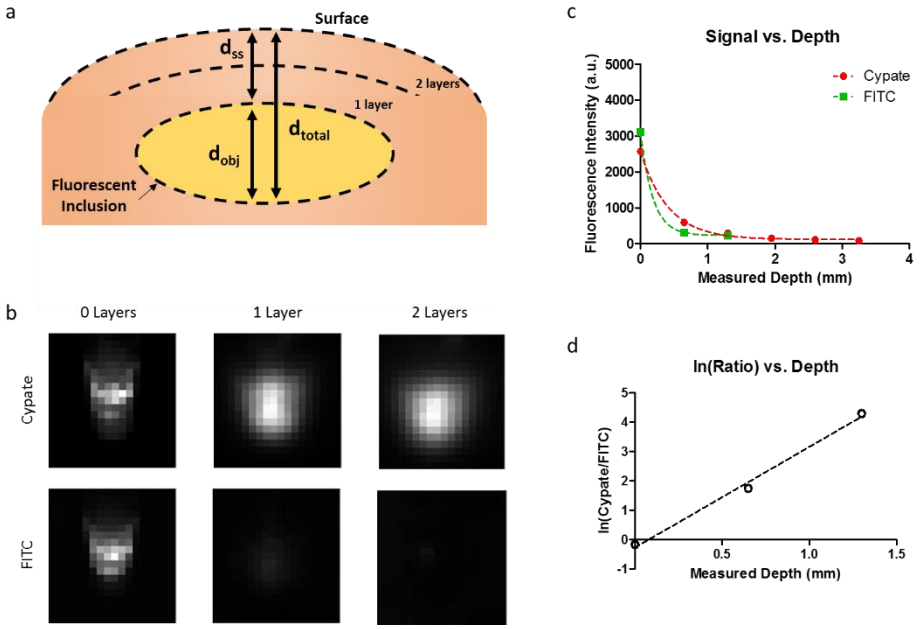

Figure 4-2: (a) Diagram showing depth configuration of fluorescent inclusion overlaid by a medium (lunchmeat, silicone, plastic, or skin). The layers represent the depth layers used for *in vitro* testing, the absolute number of layers varied depending on the test. (b) Images in both the cypate and FITC channels (rows) of an Eppendorf tube obscured by increasing layers of lunchmeat. No overlying lunchmeat in the left column, 1 layer of overlying lunchmeat in the middle column, and 2 layers of overlying lunchmeat in the right column. (c) Fluorescence signal vs. depth curve for the fluorescent ROI for LS903. (d) Natural log of the ratio of cypate-to-FITC for LS903.

4.3.2 *In vitro* vessel depth estimation

We simulated a vessel running beneath a layer of tissue by using silicone as our tissue phantom and polyurethane tubing as our vessel model. LS903 was flowed through the vessel at varying concentrations (25 μM and 50 μM) and curves for the natural log of the ratios were generated (slope = 2.08, y-int = 0.43; slope = 2.10, y-int = 0.37). Next, we tested the performance of our method using a different material of unknown depth to obscure our vessel and imaged at both wavelengths (Figure 4-3a). The predicted depth values for the vessel were mapped by using the ratio-curves previously generated (Figure 4-3b). The average estimated depth was 0.40 mm and the measured depth was 0.52 mm.

Varying the optical properties, by changing the overlying material, impacted our depth estimate (Figure 4-3c). Materials that attenuated light more produced a higher slope value than materials that attenuated light less. Ideally this slope would be predictable prior to estimating the depth. We quantified the difference in accuracy of our depth estimates using average parameters from different materials and specific parameters using the same material (Figure 4-3d). There was a significant difference when using the different values ($p < 0.001$), thus indicating the importance of calibration studies with the same material used to perform the depth estimate. To translate this approach to *in vivo* imaging, we needed to generate a curve fit equation using the same material intended for the imaging study. To accomplish this goal, we layered mouse skin at varying depths to obtain a tissue-specific curve (slope = 3.08, y-int = 0.05) (Figure 4-3e).

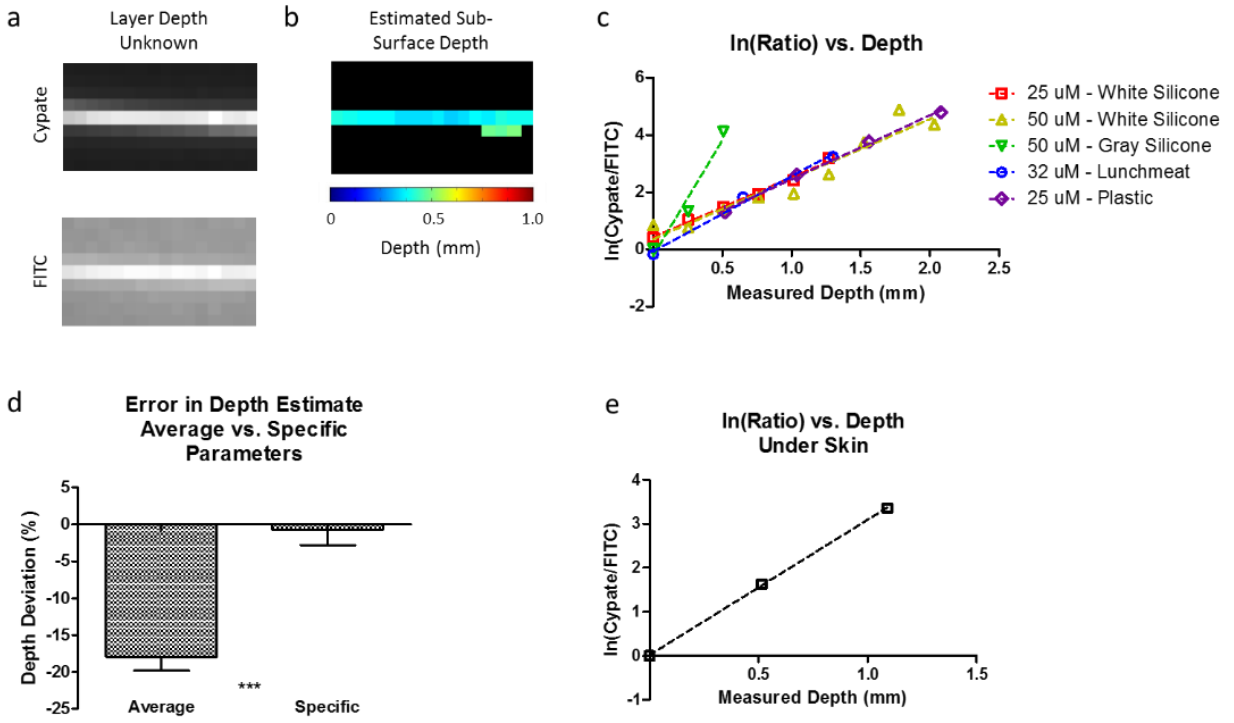

Figure 4-3: a) Dual-wavelength images of the fluorescent vessel under layers of plastic with unknown depth and optical properties. b) Depth map of estimated depth of vessel below the surface. c) Natural log of the ratio of dual signals vs. measured depth for different overlying materials and concentrations showing differing slopes depending on the medium. d) Comparison of the method accuracy for estimating depth in when using the average slope parameters and the specific slope parameter for a given medium. e) Calibration curve using the fluorescent vessel under *ex vivo* mouse skin to determine the curve fit parameters for skin.

4.3.3 *In vivo* Tumor Depth Estimation

For *in vivo* depth estimation, we injected LS903 directly into 4T1 mouse flank tumors. Mouse 1 (M1) was injected bilaterally, and mouse 2 (M2) was only injected in the left flank tumor. The two mice were imaged using a NIR-specific imaging system, and a dual-wavelength imaging system. The NIR-specific imaging system shows the fluorescence distribution of LS903 in the mice (Figure 4-4b,c). The dual-wavelength imaging system shows the fluorescence in the tumors in both the cypate and FITC channels (Figure 4-4d-f). The relative tumor signals were calculated in Fig. 4g, and in both channels the treated tumors had higher fluorescence signal than the untreated control tumor (M2-RF – not shown).

Figure 4-5 outlines the image processing method used in this study. Briefly, to estimate the depth of the fluorescence in the tumors, regions of interest (ROIs) were generated that included only the tumor in both the cypate (Figure 4-6a) and FITC channels (Figure 4-6b). The cypate image was thresholded to create the tumor ROI. This ROI was then applied to the FITC channel, and the auto-fluorescence was subtracted by using a pre-injection image. The ratio of the images obtained at two wavelengths was used to create a map of the tumor depths for each of the tumors (Figure 4-6c).

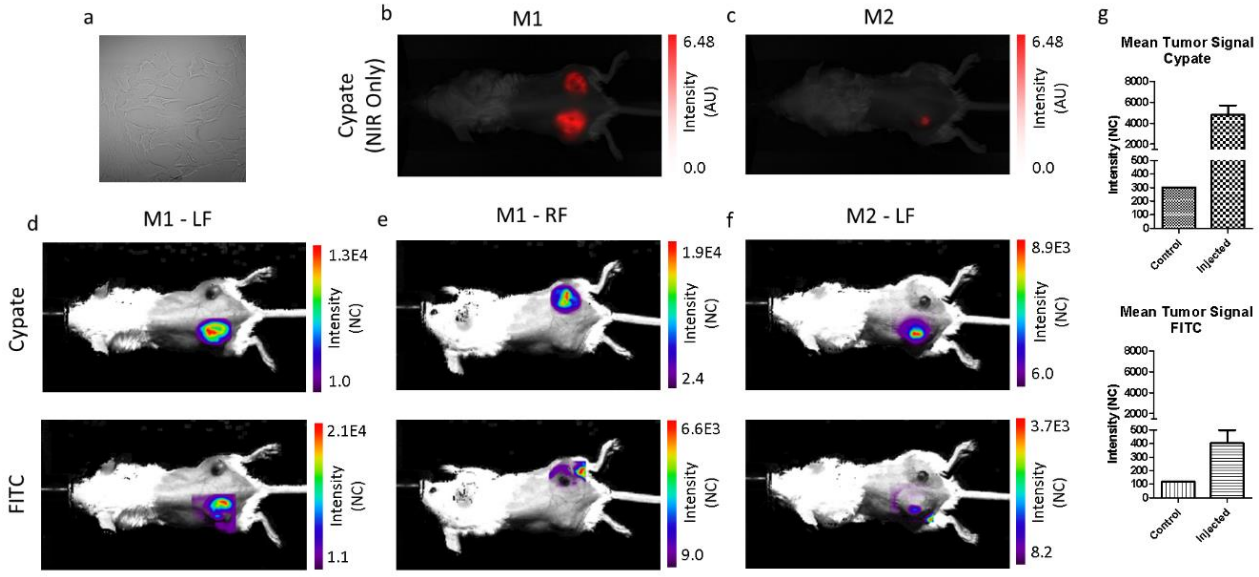

Figure 4-4: (a) Bright field image of 4T1 cells injected for xenograft model. NIR image of LS903 distribution using the cypate channel for (b) M1 and (c) M2. Dual-wavelength images of the tumor ROI in the cypate channel (top row) and FITC channel (bottom row) for column (d) M1-left flank, (e) M1-right flank, and (f) M2-left flank. (g) Quantification of the *in vivo* tumor ROI signals for the cypate channel (top) and FITC channel (bottom).

The depth values for each pixel were plotted in Figure 4-6d showing the distribution throughout the ROI. The tumor was then excised and prepared for histological analysis. The cypate and FITC channels were imaged, and areas of co-localization were analyzed (Figure 4-6e). The apparent

outline of the co-localized fluorescence region was determined by visual analysis, then 10 measurements from this outline of the co-localized area to the surface were taken. The average measured tumor sub-surface depths were 1.31 ± 0.442 mm, 1.07 ± 0.187 mm, and 1.42 ± 0.182 mm, compared to the average estimated depths of 0.972 ± 0.308 mm, 1.11 ± 0.428 mm, 1.21 ± 0.492 mm, respectively Figure 4-6f).

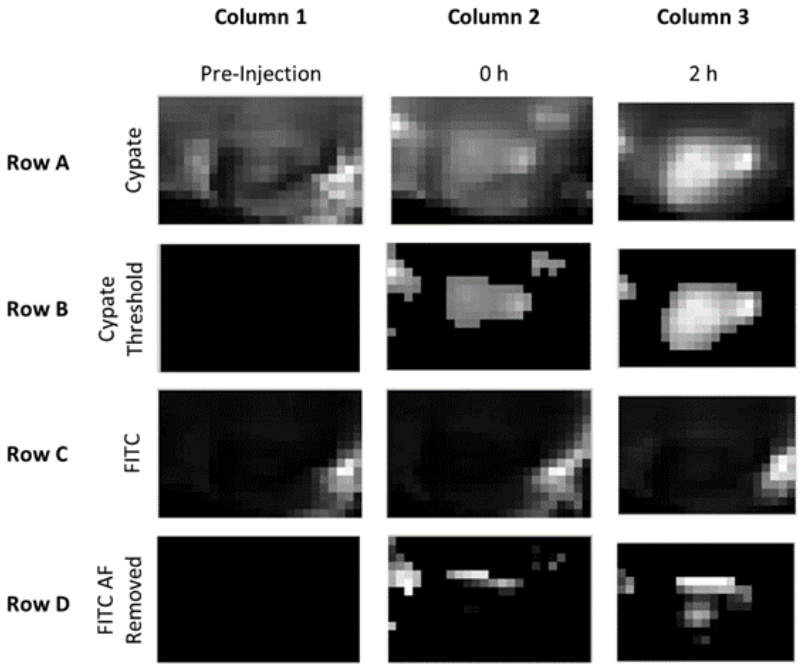

Figure 4-5: Overview of method for depth map generation from dual-wavelength imaging. Columns represent the (1) pre-injection image, (2) image immediately following the injection of the dye, and (3) image two hours following the injection of the dye. For intravenous probe administration, tumor accumulation of the dye was apparent at 2 hours post injection in the cypate channel (Row A, Column 3), so the 2 hour image was thresholded to determine the tumor ROI (Row B, Column 3). The FITC channel images contained high levels of auto-fluorescence from the hair and moderate levels in the skin (Row C). The tumor signal was not visible on a 0 – 255 grayscale until the high signal from the fur was removed. To remove the unwanted regions from the analysis, the pixels identified as the ROI using Cypate were applied to the FITC images (not shown). The remaining pixels were then compared to the average pre-injection FITC image values within the ROI. The pre-injection FITC image values were considered background and subtracted from the 2 hour FITC image, resulting in a FITC image that was of the ROI of interest with the pre-injection background values subtracted to remove auto-fluorescence (Row D, Column 3). The dual-wavelength images for cypate (Row B, Column 3) and FITC (Row D, Column 3) were used to calculate the depth estimate maps.

To evaluate if the dual emitting imaging agent dye could be used to estimate depth when administered systemically, we increased the water solubility of LS903 by conjugating it to

PEG2000, to obtain LS904. The signals were measured in both channels as a function of depth and the natural log of the ratios for LS903 and LS904 were comparable.

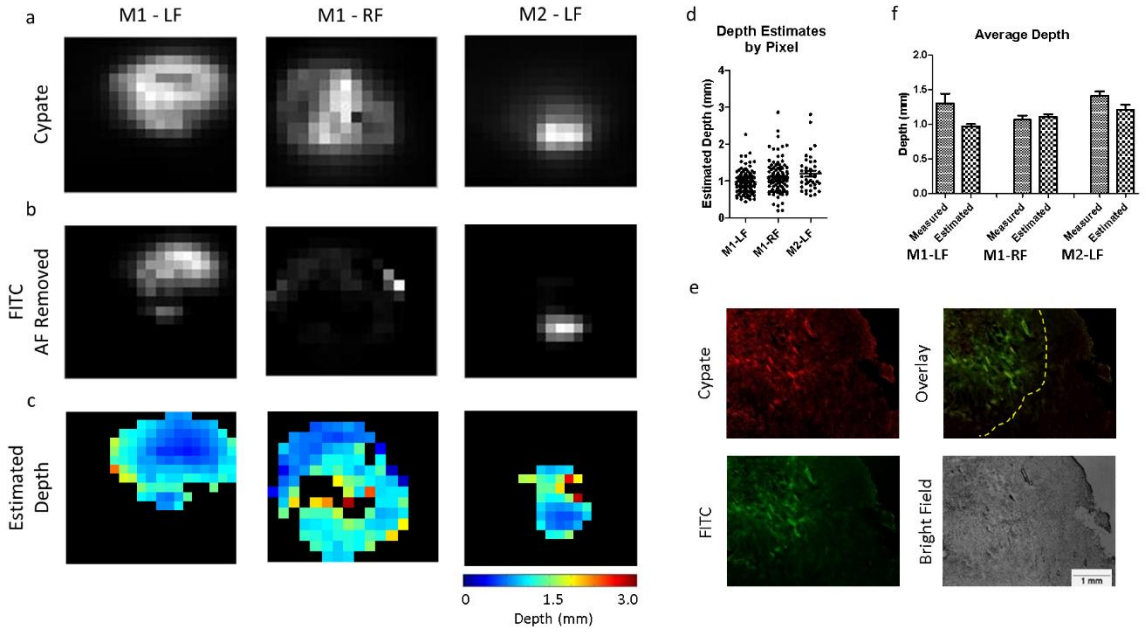

Figure 4-6: *In vivo* tumor images used for post processing. (a) Cypate images (top row), and (b) FITC images (bottom row) of the tumor region. The FITC image has the pre-injected auto-fluorescence subtracted from the tumor ROI. (c) Depth estimate maps for each of the tumors. (d) Pixel-by-pixel depth estimates for each tumor ROI. (e) Representative tumor histology (M2-LF) showing cypate fluorescence (top left), FITC fluorescence (bottom left), overlay of both channels (top right), and bright field image (bottom right). (f) Comparison of average measured depth vs. average estimated depth for each tumor.

A 4T1 tumor bearing mouse was injected via the tail vein with LS904 and then imaged using the NIR-specific and dual-wavelength imaging systems. The cypate image shows that LS904 was present in the tumor region, as well as at the injection site in the tail. Dorsal view of the non-invasive image shows accumulation of the agents in the kidneys (Figure 4-8a). The dual-wavelength images show that there was signal present in the tumor ROI in both channels (Figure 4-8b,c). The kidney was likely not visible in the FITC channel because it was deeper in the tissue than the green light could penetrate. *Ex vivo* imaging of major organs and tissues showed the

compound was primarily in the tumor, as well as the clearance organs, the kidney and liver (Figure 4-8d). Fluorescence from different tissues was quantified (Figure 4-8e). Similarly, the *ex vivo* signals were measured in both channels for a control and the injected tumors (Figure 4-8f), and the signals were quantified in Figure 4-8g.

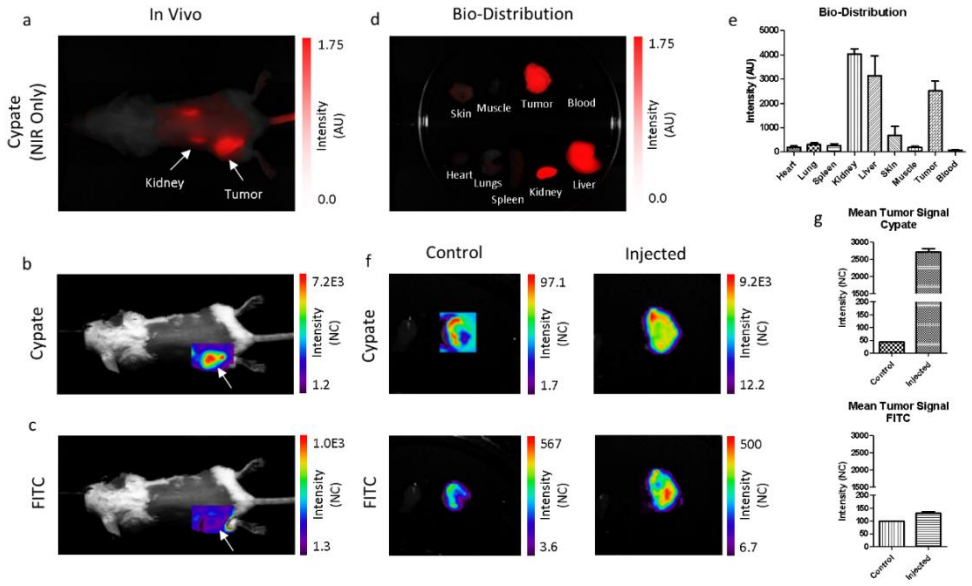

Figure 4-7: (a) NIR image of LS904 distribution using the cypate channel. Dual-wavelength images of the tumor ROI in the (b) cypate, and (c) FITC channel. (d) Cypate *ex vivo* bio-distribution showing organ distribution of the dye, with (e) quantification. (f) *Ex vivo* tumor images of a mouse that was not injected with dye (left) and injected with LS904 (right). (g) Quantification of the *ex vivo* image signals for cypate and FITC.

Depth maps were created for two tumors using the dual-wavelength images shown in Figure 4-8. Figure 4-8a shows the cypate images with the FITC images of the tumor ROIs in Figure 4-8b. Depth maps were created using our dual-wavelength images (Figure 4-8c). Figure 4-8d shows a pixel-by-pixel representation of the depth estimates, and Figure 4-8e shows the dual-wavelength histological analysis used for validation. The average measured depth values vs. the average estimated depth values for each of the tumors are shown in Figure 4-8f. The measured tumor sub-

surface depths were 1.28 ± 0.168 mm, and 1.50 ± 0.394 mm, and the estimated depths were 1.46 ± 0.314 mm, and 1.60 ± 0.409 mm, respectively (Figure 4-8e).

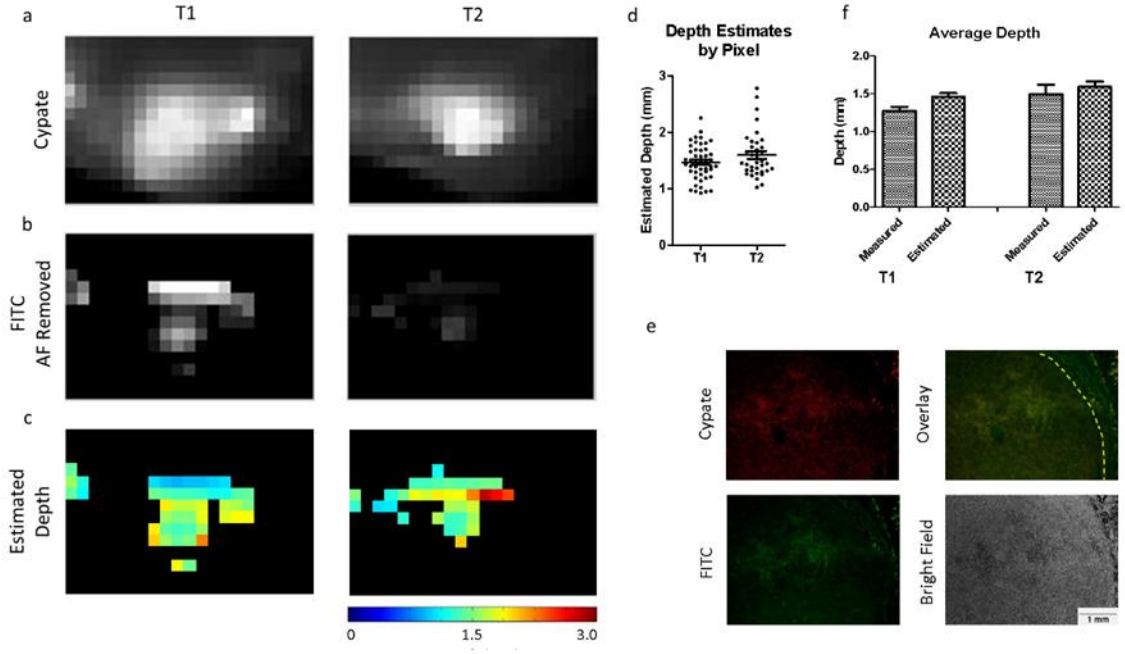

Figure 4-8: *In vivo* tumor images used for post processing. (a) Cypate images (top row), and (b) FITC images (bottom row) of the tumor region. The FITC image has the pre-injected auto-fluorescence subtracted from the tumor ROI. (c) Depth estimate maps for each of the tumors. (d) Pixel-by-pixel depth estimates for each tumor ROI. (e) Representative tumor histology (T2) showing cypate fluorescence (top left), FITC fluorescence (bottom left), overlay of both channels (top right), and bright field image (bottom right). (f) Comparison of average measured depth vs. average estimated depth for each tumor.

In previous trials, we assigned the slope of our curve based on empirical data. To lay the translational framework for this dual-wavelength approach, we next focused on a method for estimating the slope given the optical parameters of the material. We used an integrated sphere approach to calculate the absorption and scattering properties of silicone sections[76]. Figure 4-9a shows the silicone sections tested. Materials A, B and C were white silicone sections of different thicknesses and durometers, and Material D was a gray silicone section. Because the materials were each of different durometers, and therefore had different material properties, they each had different absorption and scattering coefficients that could be measured. Figure 4-9b and Figure 4-9c show the absorption and reduced scattering coefficients as a function of wavelength. Material

D did not allow enough light to pass through to calculate the optical parameters, and was therefore excluded from subsequent analysis. We then measured the Cypate and FITC signals obtained at both wavelengths of interest for each material, and used these values to calculate the coefficients of a transformation matrix. The coefficients of this matrix represented the transformation that could be used to determine the slope when the optical parameters were known. Equation 1 was used to represent the linear system of equations.

$$\Phi * x = m \qquad (1)$$

Where Φ is a matrix of measured optical parameters for materials A, B and C at the wavelengths of interest, and m is a vector of the desired slopes for an optimized depth estimate. In expanding Equation 1, the individual optical parameter values for Φ were entered for each material (A, B and C), and the series of equations represented by Equation 2 was solved for each coefficient (x)

$$\mu a_{518} x_{FITC\_ab} + \mu a_{812} x_{Cyp\_ab} + \mu' s_{518} x_{FITC\_rs} + \mu' s_{812} x_{Cyp\_rs} = m \qquad (2)$$

Table 4-1 outlines the individual optical parameter values used to solve the system of linear equations represented by Equation 2.

Table 4-1: Measured optical parameters used for the matrix Φ to solve for the transform coefficients. 518 nm used for material properties for FITC fluorescence and 812 nm used for material properties for Cypate fluorescence.

(mm^{-1})	**μa_{518}**	**μa_{812}**	**$\mu' s_{518}$**	**$\mu' s_{812}$**
Material A	0.09	0.080	6.20	4.40
Material B	0.07	0.058	7.05	5.15
Material C	0.05	0.041	6.20	4.60

In solving the system of linear equations in the form of Equation 1, we found each x value (transform matrix coefficients). These coefficients allowed us to calculate the slopes in systems with known or measured optical parameters: $x_{FITC\_ab} = 0$; $x_{Cyp\_ab} = 336.51$; $x_{FITC\_rs} = -26.56$; x_{Cyp_rs}

= 33.37. The depth of the simulated vessel was estimated using only the transform coefficients to calculate the slope. The silicone slices were stacked and the depths for the various materials were estimated (Figure 4-9d). The deviations for each material are shown in Figure 4-9e, with each material falling within 0.1 mm error. Table 4-2 shows a summary of the results.

Table 4-2: Summary of estimated depths of simulated vessel under silicone obtained using the slope calculated from the measured optical parameters.

Material	**A**	**B**	**B**	**C**	**C**
Estimated Depth (mm)	0.318	0.302	0.695	0.481	0.986
StDev (mm)	0.116	0.269	0.394	0.350	0.414
Measured Depth (mm)	0.254	0.381	0.762	0.508	1.016
Deviation (mm)	0.064	-0.079	-0.067	-0.027	-0.030

The approach was then repeated using our previously obtained mouse tumor images along with optical parameter values reported in the literature for mouse skin. Mouse skin values at 518 nm and 812 nm were used to conduct this analysis with the absorption coefficients at approximately 0.175 and 0.070 mm^{-1}, and the reduced scattering coefficients at approximately 1.65 and 0.70 mm^{-1}, respectively[77]. Using these optical parameter values, and our calculated transform coefficients, we calculated a slope of 3.09 to use for the fluorescence depth estimates. The results obtained using this slope are shown in Figure 4-9f, and the deviations from the depths obtained using histology are shown in Figure 4-9g.

Using the forward model of optical parameters to estimate depth yielded results within 0.38 mm for the intra-tumor injections, and 0.63 mm for the intravenous injections. A summary of the results is shown in Table 4-3.

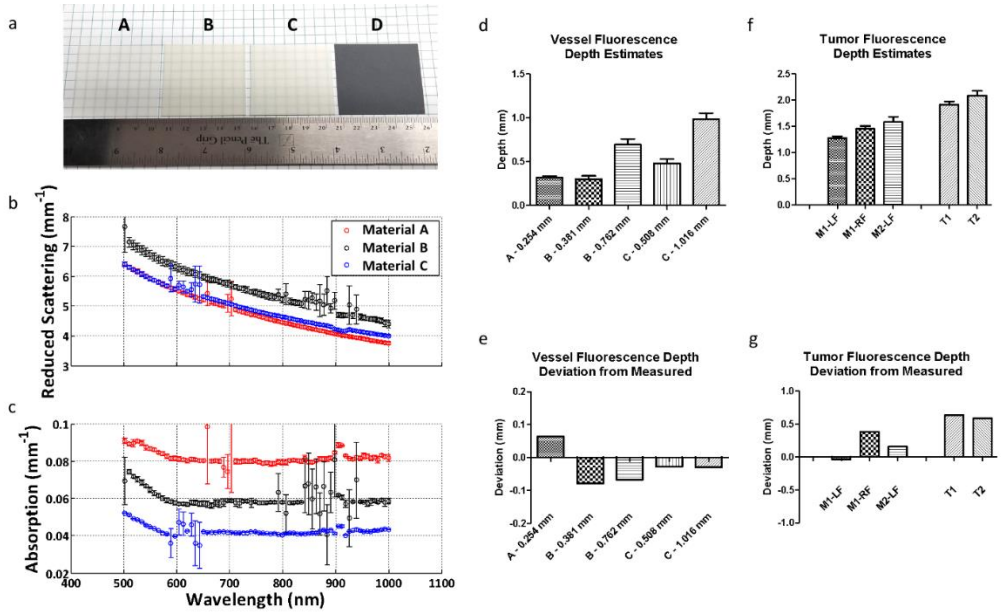

Figure 4-9: (a) Images of silicone sections used to calculate absorption and reduced scattering coefficients at multiple wavelengths. Materials A, B, and C were white silicone sheets of different thicknesses and durometers. Material D was gray silicone, however it was too opaque to obtain optical parameter data. (b) Reduced scattering coefficients as a function of wavelength for each material tested. (c) Absorption coefficients as a function of wavelength for each material tested. (d) Average fluorescence depth estimates of the simulated silicone vessel under the silicone sheets for each material using the optical parameter approach. Materials B and C were each stacked to show multiple depth estimates for the same material. (e) Average depth estimate deviation from measured for each material. (f) Average fluorescence depth estimates *in vivo* using the optical parameter approach. (g) Average depth estimate deviation from measured for each tumor.

Table 4-3: Summary of estimated depths of tumor fluorescence *in vivo* obtained using the slope calculated from literature optical parameters.

Tumor	**M1 - LF**	**M1 - RF**	**M2 - LF**	**T1**	**T2**
Estimated Depth (mm)	1.271	1.448	1.578	1.913	2.085
StDev (mm)	0.401	0.557	0.641	0.408	0.532
Measured Depth (mm)	1.310	1.070	1.420	1.280	1.500
Deviation (mm)	-0.039	0.378	0.158	0.633	0.585

4.4 Discussion

We have outlined a method for determining the sub-surface depth of a fluorescent inclusion obscured by a scattering medium for the applications of depth determination of blood vessels and tumors. Using a monomolecular dual-wavelength probe eliminates errors caused by the difficulty

in accurately determining the concentration of different dyes, because the dyes are present in equimolar quantities. As such, the ratio of the signal obtained from each dye is predictable and can be used to calculate the depth. Because our green light signal attenuates rapidly in the tissue, we were only able to apply this technique to determine the sub-surface depth when the fluorescent inclusion was near the surface. By conjugating a red or NIR dye to cypate, we would be able to obtain deeper tissue imaging.

Our method is beneficial because it is non-invasive, and it can be used in situations where a physical measurement is not possible. In the case of the tumors containing the fluorescence, the distance of the fluorescence below the surface could not be measured using calipers because there was no defined physical surface to measure from. Assessing the tumor sub-surface depth using calipers would require perturbing the tissue, and would be difficult to execute since skin and subcutaneous tissue deform when physically contacted. We attempted this, however we were only able to obtain measurements of the skin itself (which was also distorted). This measurement was not representative of the system because the fluorescence in our tumors was localized to tissue deeper than just the skin layer. Because a physical measurement was not possible, we relied on fluorescence histology to validate our approach. We conducted 10 measurements from the co-localized signal to the surface, however additional measurements over a larger area would be needed to report the robustness of the method.

Others in optical imaging have investigated FMT for depth estimation. The depth resolution that we were interested in was on the order of tenths of a millimeter as we were interested in the sub-surface depth. The spatial resolution of FMT is on the order of millimeters to tenths of a millimeter in an idealized situation, however imperfect fluorophore localization to the tumor makes FMT impractical for this application given the desired spatial resolution. FMT is suited for

understanding the spatial distribution of a fluorescent inclusion where the dimensions of the inclusion itself are of interest such as d_{obj} in Figure 4-2a. Because our approach relies on the location of the fluorescence signal for depth determination, the targeting moiety must be specific to the structure of interest. We employed the EPR effect to deliver our probe, and demonstrated higher tumor signal compared to surrounding tissue Figure 4-7. Many tumor targeting probes are under development, and these probes have the potential to improve the accuracy of the method.

The dual-wavelength approach for sub-surface depth estimation is also impacted by tissue optical properties. As such, *a priori* knowledge of the type of tissue could be applied in a feed-forward manner for translational imaging. Our method involved a preliminary calibration study to correlate the expected signal at measured depths in a specific medium. Other researchers have developed methods for estimating tissue optical properties including parameterized mathematical models[78] and *in vivo* spatial-frequency domain imaging[79]. By combining these techniques with a dual-wavelength probe, accurate depth-resolved tissue imaging may be achievable in many different tissue types.

We have demonstrated the feasibility of using a dual-wavelength custom developed fluorescent probe to determine the sub-surface depth of structures in tissue. An advantage of using an optical probe over auto-fluorescence spectral data alone, is that dyes also can be readily targeted to specific biologic structures using cellular receptors. The specificity of optical imaging allows for flexibility in the approach for different preclinical and clinical uses, such as when a physical depth measurement would disrupt the tissue or be difficult to obtain. The simplicity of real-time planar optical imaging is advantageous for applications such as intraoperative imaging; allowing for the same fluorescent probe to be used for both the identification of and the depth characterization of structures in tissues. By understanding the sub-surface depth of a tumor,

positive margins in the z-direction may be reduced. Further, once a gross pathological specimen is removed from the body, real-time margin assessment can be performed via imaging prior to histological evaluation.

4.5 Conclusions

We demonstrated the feasibility of using a dual-wavelength custom developed fluorescent probe to determine the sub-surface depth (d_{ss}) of structures in tissue. We used a dual-wavelength method utilized LS903 with a green-emitting, and a NIR-emitting portion for this purpose.

In the previous chapters, we have discussed about fluorescence imaging agents and used emission signal in various ways to gather information. In the next chapter, we will explore fluorescence lifetime properties of such imaging agents and describe one application of lifetime imaging for tracking intracellular processes.

Chapter 5

Molecular probes for fluorescence lifetime imaging

5.1. Introduction

This chapter briefly introduces molecular probes used for generating fluorescence lifetime contrast as published before,[80] and describes synthesis and application of a molecular probe which shows protein binding dependent changes in fluorescence lifetime. Singlet-state fluorescence occurs when a fluorophore absorbs radiation of specific energy followed by the emission of photons as the molecule returns to the ground state. Because energy is lost between the excitation and emission processes, fluorescence is emitted at a higher wavelengths than those of the excitation radiation.[8] Several factors affect molecular fluorescence, including the molecular structures and associated vibrational energy levels as well as the physical and chemical environment of the fluorophores.[8] Perturbation of the fluorescence of many organic molecules could decrease the quantum yield at the same emission wavelength or cause spectral shift. Both effects are useful for biological applications. Within linearity, changes in the fluorescence intensity can be used to determine the concentration of fluorophores in a medium. Shifts in the spectral profile of fluorophores can provide quantitative data via ratiometric measurements at two different wavelengths. Although these approaches are highly reliable for reporting biological events in solutions or shallow surfaces, enhanced light scattering and absorption in heterogeneous mediums such as cells and tissue can adversely affect the fluorescence intensity in a less predictable manner. For these reasons, most fluorescence measurements in cells and tissue are typically reported in a relative intensity measurement using calibration standards or by self-referencing.

Unlike fluorescence intensity-based imaging, fluorescence lifetime (FLT) of molecular probes is less dependent on the local fluorophore concentration or the method of measurement, which minimizes imaging artifacts and provides reproducible quantitative measurements over time.[8] The

FLT of fluorophores is the average time a molecule spends in the excited state between absorption and emission of radiation before returning to the ground state.[8] Accurate determination of the FLT of fluorophores and application in biological imaging and spectroscopy depend on both instrumentation and understanding of the fluorophore system. The FLT of a fluorophore can be measured by spectroscopic, microscopic, or *in vivo* imaging methods. Several FLT instruments are commercially available for spectroscopic and microscopic FLT measurements. For *in vivo* imaging, many studies rely on custom-built FLT systems[81] because the only company (ART, Advanced Research Technologies, Canada) producing a commercial system is no longer operational. Because several papers have reviewed advances in FLT measurement methods and devices, this review will focus on fluorophore systems and how changes in their FLT contribute to our understanding of biological events. FLT of a molecule changes with small changes in the immediate microenvironment of the molecules and therefore can be used to report cellular and molecular processes with very high sensitivity. [8]

5.2. Classification of molecular probes for lifetime imaging

Classification of molecular probes used for FLT imaging can be based on their FLT properties, emission wavelengths, or response to specific biological microenvironment.[81] Figure 5-1 shows some fluorophore systems commonly used for lifetime imaging and the range of their photoluminescence lifetimes. Broadly, molecular probes used in FLT imaging can be classified into endogenous fluorophores and exogenous contrast agents. Exogenous agents can then be grouped according to their response mechanism and applications. Comprehensive reviews and classification for these molecules can be found in literature. [80,81]

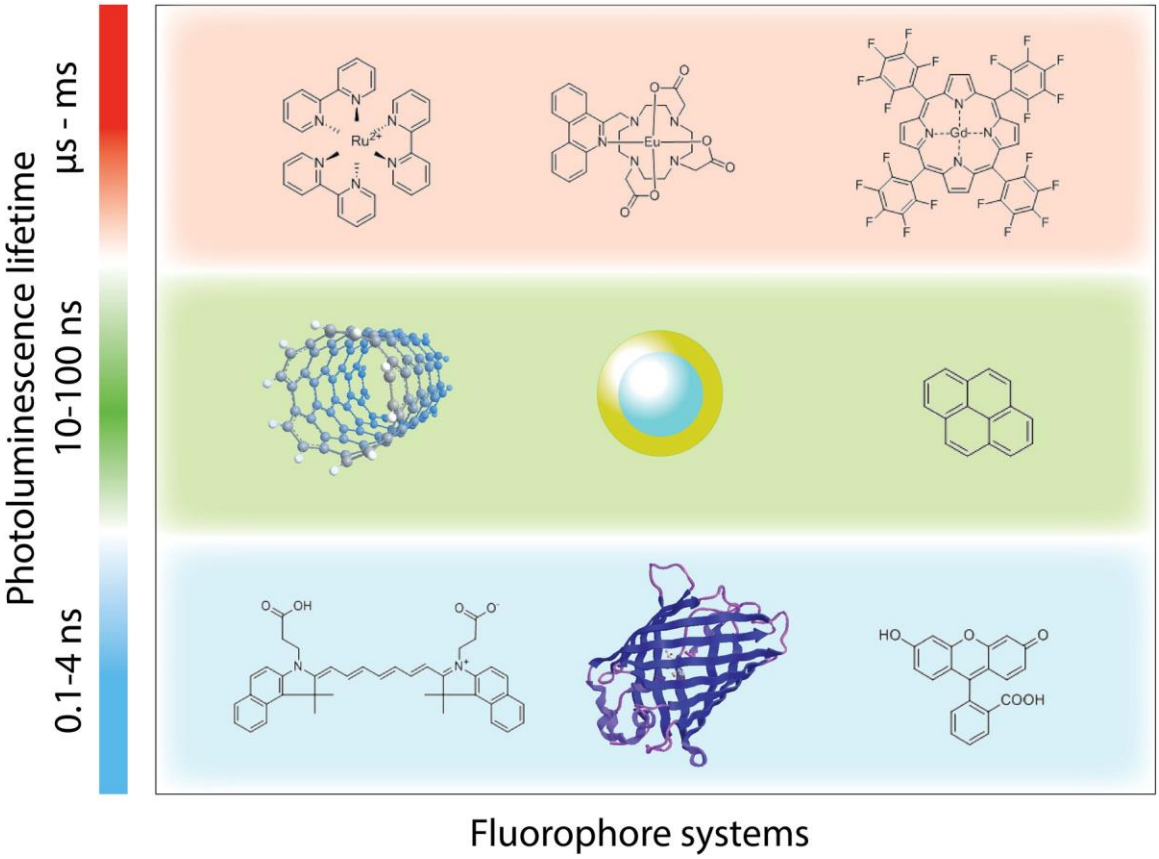

Figure 5-1: Representative fluorophore systems commonly used in lifetime imaging and associated photoluminescence lifetimes. These fluorophores can be used in their native forms and/or after conjugation to other entities.

5.2.1. Endogenous fluorophores

Most biospecimen possess intrinsic fluorescence because of the presence of some fluorescent biomolecules such as aromatic amino acids, fluorescent pigments, reduced nicotinamide adenine dinucleotide (NADH), flavin adenine dinucleotide (FAD), porphyrin, and some structural proteins.[82] The expression levels or locations of these biomolecules can inform investigators on the functional status of cells and tissue. Below is a summary of the application of the most commonly reported endogenous fluorophores in FLT imaging.

Melanin. Melanin (ex/em: 340-400/360-560 nm) is a pigment produced by melanocytes and widely present in living organisms.[83] FLTs of melanin range up to ~8 ns.[82] Current literature has

focused on studying FLT of melanin in healthy and cancerous skin. One such study has shown that the mean FLT of melanin can discriminate between healthy skin, basal cell carcinoma (BCC), and melanoma in fresh biopsies.[84] Another work demonstrated a significant difference in FLT between keratinocytes and melanocytes, information that was used to characterize melanoma.[85] FLT of melanin has also been shown as the baseline indicator for detecting oxidative stress conditions in retinal pigment epithelial cells.[86] With the miniaturization of FLT systems, it is expected that FLT measurements can be used to screen suspicious lesions at point-of-care settings in future.

NADH/FAD. NADH and its phosphate derivative NADPH (ex/em: 350/450 nm) are the dominant endogenous fluorophores in cells participating in cell metabolism, reductive biosynthesis, antioxidation, cell signaling, aging, and regulation of apoptosis.[87] They have a mean FLT ~2.3-3.0 ns when bound to proteins and a short FLT ~0.3-0.4 ns in free form.[82] Their FLTs are sensitive to solvent polarity and viscosity, and affected by their dynamic quenching in the presence of adenine moiety.[88,89] FAD is another endogenous fluorophore that plays the role of redox cofactor in cells. FAD emits at a longer wavelength (ex/em: 450/535 nm) than NAD(P)H. Only the unbound form of FAD is fluorescent, with an FLT of 2.3-2.9 ns.[82] The complementary metabolic functions of FAD and NAD(P)H allow the use of their FLT changes to report the metabolic state of cells. Physiologic parameters such as pH and O_2 levels, as well as changes in tyrosine or tryptopham concentrations and local temperature are readily obtained from NAD(P)H/FAD FLT measurements.[90]

FLT of NADH has been extensively studied in early detection and diagnosis of skin cancer. A recent study reported measuring the FLT of NADH at different depths from the tissue surface in fresh biopsies of both healthy skin and BCC. A different mean FLT was measured along different healthy skin layers, ranging from 800-950 ns. This is attributable to differences in the metabolic

state of different layers of healthy tissue. In contrast, negligible variation of FLT was observed in BCC skin layers because BCC is characterized by hyper-proliferation of basal cells inside the epidermis, obviating the cellular differentiation typical of healthy skin.[91] The inverse relationship between the FLT of protein-bound FAD and NAD concentration (a non-fluorescent oxidized form of NADH) has been used to determine NAD level in cells.[92] Imaging of brain activity has become an exciting field of research because of the potential to predict a variety of neurological diseases *via* imaging. In optical imaging, absorption mode is currently used to map brain activity, but this method relies heavily on subtle changes in the ratio of oxy- and deoxy-hemoglobin. To improve detection sensitivity, the FAD/NAD(P)H fluorescence ratio can be used for determining changes in cellular metabolism during neuronal activity. However, FLT measurements may provide more stable longitudinal data in high throughput format by measuring the FLT of either NAD(P)H or FAD at a single wavelength. This information can then be correlated with other factors without the need to measure multiple FLTs.

5.2.2. Exogenous molecular probes

The shallow penetration of light in the UV and visible light regions of the electromagnetic spectrum, as well as the low expression of a target endogenous fluorophores in tissues of interest confine the applications of these measurements to specialized cases of pathophysiology. In addition, the weak and nonspecific nature of the endogenous fluorescence further requires long signal acquisition time and sophisticated image analysis software to enhance detection sensitivity and decipher different types of tissue. These limitations can be overcome by the use of exogenous contrast agents.[81]

The FLTs of some fluorophores are minimally affected under diverse biologically relevant conditions. These molecules provide stable FLT imaging data in different tissues. In many cases,

the local environment can alter the FLTs of other fluorophores. To achieve specific response, changes in FLTs can be induced through diverse molecular designs.

Static FLT Probes. Fluorescent molecular probes and nanoparticles that do not exhibit significant changes in their FLT in biological medium are static FLT probes. Stability of the FLTs provides reliable imaging signal over time and can be used to improve the spatial resolution of the molecular probe distribution without distortion from intractable FLTs in different compartments. For example, the stable FLT of fluorescent nanodiamonds, which is distinct from tissue autofluorescence FLT, was successfully used to track lung stem cells *in vivo*.[93] Static FLT molecular probes are particularly useful in information multiplexing. By targeting different biomolecules with molecular probes exhibiting different FLTs, quantitative ratio-imaging can readily be achieved without compensating for imaging artifacts encountered in intensity-based measurements. A unique feature of this approach is the potential to image fluorophores with similar excitation and emission wavelengths, but with different FLTs. Not only will this approach overcome wavelength-dependent attenuation of light that affects fluorescence intensity readouts, but it also facilitates rapid data acquisition and analysis. Furthermore, the limited number of emission channels in regular confocal microscopes or *in vivo* imaging systems limits the scope of intensity-based multiplex imaging or cell sorting. In contrast, it is possible to track different types of cells labeled with fluorescent dyes of distinct FLTs in small animals or cell culture to understand disease pathology.[94,95]

Responsive FLT Molecular Probes. Unlike stable FLT molecular probes, the need to quantitatively interrogate molecular processes without resorting to ratiometric imaging techniques has stimulated the design of reporter molecules that changes FLT as a function of their environment. These designs utilize similar approaches used to develop intensity-based activatable

molecular probes.[96] We have classified these FLT imaging agents on the basis of the response mechanism – biomolecular, biochemical, and biophysical. Below we have discussed biomolecular binding responsive FLT probes and described synthesis, characterization nd application of such probe.

Biomolecular Binding-Responsive FLT Molecular Probes.

Many fluorescent probes are designed to alter their FLTs in response to biological events. For imaging molecular interactions, structural features that utilize Förster resonance energy transfer (FRET) technique is used. Adjacent fluorophores can perturb the residence time of fluorescent molecules in the excited state, leading to a decrease in the average residence time in this state. Although FLT is less dependent on fluorophore concentration, detectable fluorescence signal is still required to measure this parameter. In molecular designs where the fluorescence is completely quenched, FLT imaging would resemble traditional fluorescence enhancement *via* activatable probe method. However, instead of reporting an increase in fluorescence intensity, a well calibrated FLT decrease relative to the distance of the quenching or acceptor molecule could be used to determine distance-dependent molecular interactions with high accuracy. Here, energy transfer from a fluorescent donor to an acceptor molecule is expected to decrease the donor FLT and increase the acceptor FLT. In this section, we discuss FRET-based studies that alter FLTs through biologically-induced disruption of interaction between the acceptor and donor fluorescent molecules.

FLTs of fluorescent proteins (0.1–4 ns) used to design donor-acceptor FRET pairs provide excellent FLT maps of biomolecular interactions or activities by fluorescence lifetime imaging microscopy (FLIM). Examples of fluorescent protein pairs for FRET-based FLIM include green

fluorescent protein (GFP)–DsRed (ex/em: 395/509–554/586 nm),[97] GFP–mCherry (ex/em: 395/509–587/610 nm),[98] cyan fluorescent protein (CFP)–Venus (ex/em: 435/485–515/528 nm),[99] and CFP–yellow fluorescent protein (YFP) (ex/em: 435/485–514/527 nm).[100] Small organic dyes (FLT: 0.1-90 ns) that undergo FRET are also used for FRET-based FLIM. Examples of such pairs include Alexa Fluor (AF) 488–Cy3 (ex/em: 495/519–550/570 nm),[101] AF488–AF647 (ex/em: 495/519–650/665 nm),[102] Cy3–Cy5 (ex/em: 550/570–650/670 nm),[103] and AF700–AF750 (ex/em: 702/723–749/775 nm).[104] Lanthanides paired with organic dyes[105] or with fluorescent proteins,[106] have also been used as FRET donors because of their stable and long FLTs (μs to ms).[81]

FRET-based FLT molecular designs have been used to report the activity of enzymes, such as proteases. This approach is particularly useful for endoproteases, where the amide cleavage site is flanked by several amino acids, allowing the incorporation of donor-acceptor fluorescent molecules at both ends of a peptide substrate without disrupting the enzyme activity. Examples include imaging the use of caspase-3 FRET-FLT substrate to image the up-regulation of caspase-3 in cancer.[107] Similarly, a FRET pair consisting of fluorescein (donor)-bovine serum albumin (BSA; acceptor) conjugate, was used to determine intracellular proteolysis of BSA *via* FLT increase from 0.5 to 3.0 ns.[108]

Instead of using dynamic donor-acceptor fluorophore quenching for FRET, some investigators prefer static quenching using macro-molecular self-quenched probe designs. Here, multiple fluorescent molecules are linked to a polymeric or large molecule to alter the absorption and, most often, quench the dye fluorescence. By using FLT instead of intensity measurement, high fluorescence quenching, which could affect enzyme recognition of the substrate, is not necessary. A change in FLT from the initial value will then be used to track biological activity. Recently, Goergen *et al.*[109] synthesized cathepsin B activatable macromolecular probe, consisting of IRDye

800CW (ex/em: 778/794 nm). Spectroscopic analysis showed FLT increase upon cleavage of specific amide bonds by cathepsin B. *In vivo* FLT imaging of cathepsin B activity in mouse infarcted myocardium was achieved with the molecular probe. FLT imaging was able to distinguish nonspecifically accumulated molecular probe in the liver from the cathepsin B activated reporter system in the infarcted regions.[109] A similar study by Solomon *et al.* employed a self-quenched enzyme cleavable FRET probe, MMPSense750 FAST (ex/em: 749/775 nm), for imaging the expression of matrix metalloproteinases in tumor bearing mice.[110]

As described above, FLT imaging can add valuable and complementary information to that provided by regular emission intensity measurements. Several near-infrared cyanine dyes demonstrate fluorescence lifetime sensitivities to changes in hydrophobicity of the immediate microenvironment.[111] The same is manifested as two distinct lifetimes of the dyes when bound to two different pockets of albumin with varying hydrophobicity. We hypothesized that the same will be demonstrated by a molecularly targeted version of such dyes. The targeted molecular probe will have distinct lifetime changes associated with binding to the target protein and thus longitudinal lifetime imaging with such a construct may potentially allow us to follow the behavior of the target proteins in cells or *in vivo*. To demonstrate this, we constructed a molecular probe containing NIR dye cypate which was targeted the folate receptor (FR) using a folic acid moiety. FRs have prominent roles in several types of aggressive cancers. We used lifetime imaging of our molecular probe to study the kinetics of internalization of FR in KB cells and were able to differentiate specific vs. non-specific uptake.

5.3. Materials & Methods

5.3.1. Synthesis protocols

All chemicals and reagents were purchased from commercial sources and were used without further purification. Each step was characterized by liquid chromatography-mass spectrometry (LC-MS) using electrospray ionization (ESI) as the ionization method).

Synthesis of molecule 2: Folate acid (**1**, Sigma Aldrich) was functionalized with and primary amine as indicated using hydrazine. Folic acid (44.14 mg, 100 µmoles) was dissolved in 3 mL anhydrous DMSO with sonication over few hours. 1-Ethyl-3-(3-dimethylaminopropyl)carbodiimide (28.76 mg, 150 µmoles) and N-Hydroxysuccinimide (12.66 mg, 110 µmoles) were added to this solution and left overnight on a shaker. Hydrazine (36 mg, 1.1 mmoles).The crude mixture was further purified by HPLC equipped with a reverse-phase C-18 column to obtain **2** as a pale yellow solid. Yield calculated was 73%. MS(ESI) m/z calculated for 2 [M + H]+: 455.4, found 456.

Synthesis of LS872: All solids were dried overnight under vacuum to get rid of moisture. Cypate (66 mg, 100 µmoles) was dissolved in 3 mL anhydrous DMF. N,N′-Diisopropylcarbodiimide (12.8 mg, 100 µmoles) and N-Hydroxysuccinimide (11.7 mg, 100 µmoles) were added to this mixture

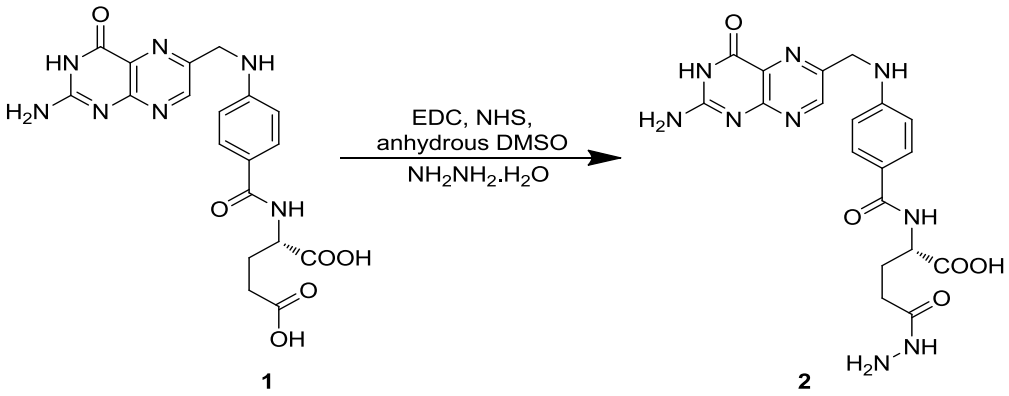

Chemical Formula: $C_{19}H_{21}N_9O_5$
Molecular Weight: 455.4

and shaken overnight. Next day, compound **2** (46 mg, 100 µmoles) was added and shaken overnight. The crude mixture was further purified by HPLC equipped with a reverse-phase C-18 column to obtain **LS872** as a yellowish green solid. Yield calculated was 63%. MALDI TOF m/z calculated for LS872 $[M + H]^+$: 1063.2, found 1063.43.

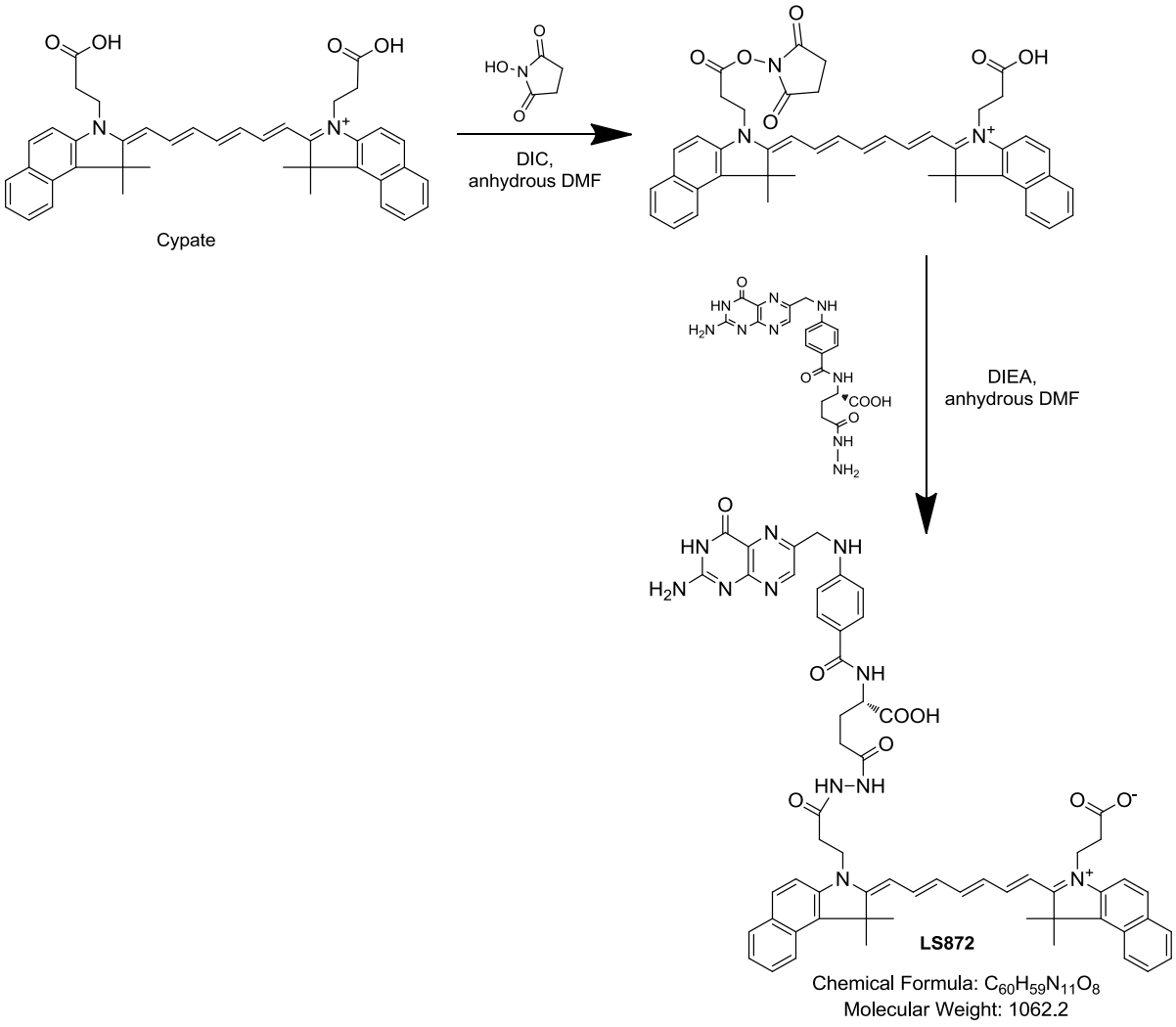

5.3.2. Spectroscopic characterization

For spectral characterization, the cypate and LS872 diluted in DMSO. Absorption spectra were measured on a DU 640 spectrophotometer (Beckman-Coulter, Brea, CA).

5.3.3. Cell studies

Folate receptor (FR) expressing KB cancer cell line was obtained from ATCC. The cells were maintained in MEM supplemented with 10% fetal bovine serum and 1% Pen-Strep. For the cell experiments, the cells were culture in RPMI without folic acid supplemented similarly. This was done for enhanced expression of folate receptor by the cells.

For establishing specificity of LS872, about 10,000 FR+ KB cells per well were plated in 8-well cell culture slides (BD Biosciences, San Jose, CA) and allowed to grow over-night. FR+ KB cells were treated with 1 µM LS872 with and without 100uM folic acid. FR- A549 cells were also treated with 1 µM LS872. To observed membrane receptor binding, cells were incubated at 4°C for 15 min with 5 µg/mL Hoechst 33342 (ThermoFisher Scientific) for nuclear staining. Cells were washed and replenished with fresh media before imaging.

For lifetime imaging studies, about 40,000 KB cells were plated on glass bottom dishes (35 mm, No.1, MatTek Corporation) allowed to grow over-night. For initial studies, cells were treated with 1 µM LS872 or cypate and incubated for 1 hour at 37°C. Cells were washed thrice and replenished with fresh media and imaged immediately. For tracking lifetime changes associated with receptor mediated endocytosis of LS872, cells were incubated with 1 µM LS872 at 4°C for 10 to allow binding with cells surface FR. Cells were washed thrice and replenished with fresh media and imaged over time.

Cells were imaged with Olympus BX51 upright fluorescence microscope (Olympus America, PA, USA). LS872 was imaged using 775/50 nm excitation and 845/55 nm emission. Hoechst 33342 was imaging using 330-385 nm excitation and 420 long pass emission. Images were processed on ImageJ.

5.3.4. Fluorescence lifetime spectroscopy and microscopy

Lifetime data collection was performed on a Picoquant Micrtotime200 microscope. For spectroscopy, solutions of 1.32 µM LS872 or cypate in PBS, or PBS containing 6.6 µM FR or bovine serum albumin were used. The protein – dye solutions were allowed to incubate for at least 2 minutes to allow to maximum binding. The final mixtures were excited using a 785 nm laser at 40 MHz pulse rate with instrument response function below 300 ps. Emission was collected with an 819 nm long pass emission filter. Spectroscopic data was collected with a 40X objective.

For tracking lifetime changes associated with receptor mediated endocytosis, after washing cells were maintained in a stage top incubator (W. Nuhsbaucm Inc.) at 37°C with 5% CO_2 for imaging over hours.

5.3.5. Lifetime data analysis:

Spectroscopy and microscopy data was analyzed on the SymphoTime software (Picoquant). Decay data fitted to exponential decay equations using n-exponential tail-fit method. Chi square values were used to judge goodness of fit.

5.4. Results

5.4.1. Imaging agent LS872:

Absorption spectra of FR targeted LS872 [Figure 5-2a] shows cypate spectra and additional peaks at ~283 nm and ~368 nm due to absorption by the folic acid moiety [Figure 5-2b]. The binding

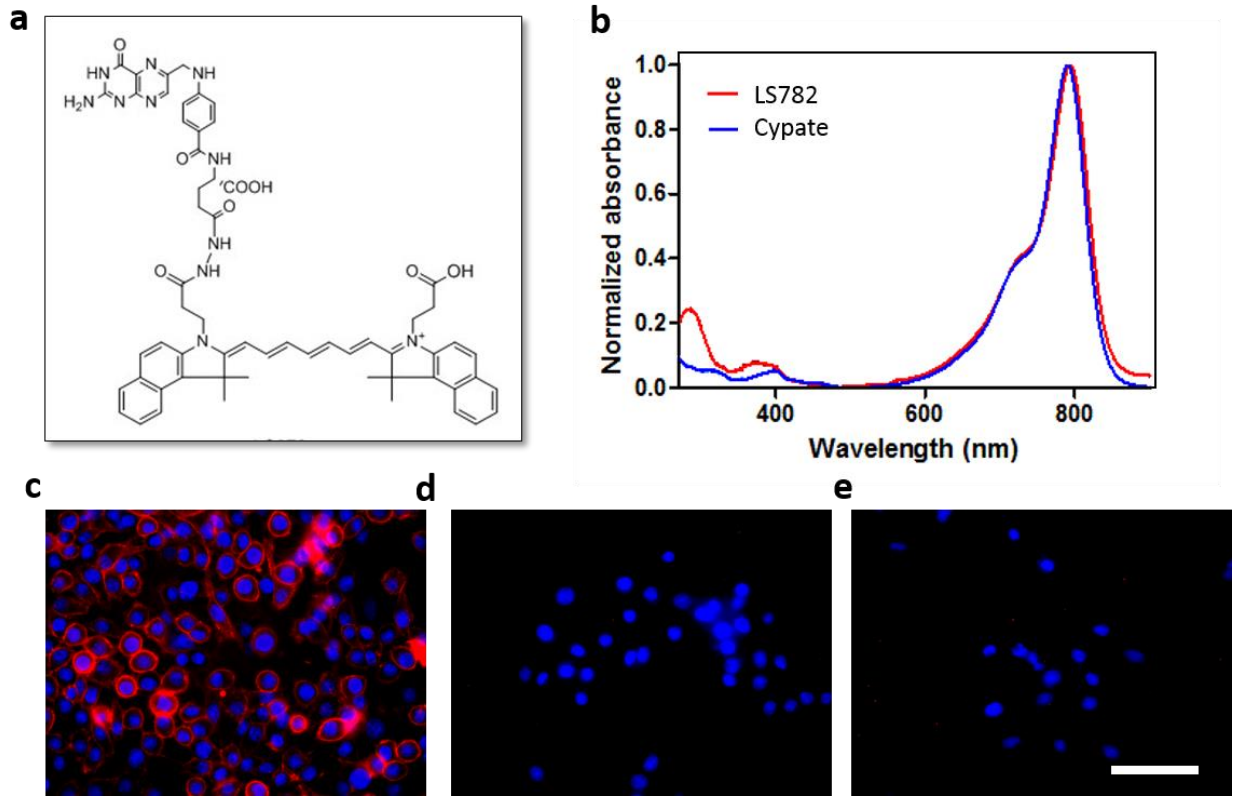

Figure 5-2: (a) Molecular structure of LS872. (b) Absorption spectra of LS872 and cypate in DMSO. The unique peaks for LS872 at 283 nm and 368 nm are due to absorption by folic acid. Specificity of LS872 (red) to cell surface FR is shown by cell membrane binding of LS872 in FR+ KB cells, (c) inhibition of binding in presence of 100X excess folic acid and (d) absence of binding in FR- A549 cells. Blue (Hoechst 33342, nuclear stain). Scale: 100 µm.

specificity of the LS872 to cell surface FR is demonstrated using FR+ KB cells and FR- A549 cells [Figure 5-2c-e] Cell membrane binding can be observed in KB cells in presence of 1 µM LS872 [Figure 5-2c] which could be blocked by co-incubation with 100 µM folic acid [Figure 1d]. No cell membrane is observed in FR – A549 cells [Figure 5-2e].

5.4.2. Fluorescence lifetime properties of LS872 and Cypate

Next we explored if the binding of LS872 to FR results in distinct changes in its fluorescence lifetime. As a control we used cypate which would not bind to the folate specific binding pocket of the receptor i.e. would not show specific binding. We measured the fluorescence lifetime of LS872 and Cypate in the presence of 5X molar excess of the folate receptor in PBS. Excess FR was used in order to ensure no free LS872 in the solution. Decay curves from LS872-FR and Cypate-FR could be fitted to a double exponential decay curves with amplitude average lifetime τ_{avg} = 450 ps ± 30 ps and τ_{avg} = 350 ps ± 40 ps [Figure 5-3a]. LS872 in PBS with no FR gave a much shorter lifetime τ_{avg} = 320 ps ± 10 ps [Figure 5-3a]. The significant difference between LS872-FR and cypate–FR and between LS872-FR and LS872-PBS can be attributed to the specific binding interaction of LS872 with FR which manifests as a unique lifetime value. Free LS872 can thus be distinguished from FR bound LS872 using deviation from this unique lifetime. We also used bovine serum albumin (BSA) which is not expected to interact with folate but it interacts with cypate.[111] We showed that the lifetime of both LS872 and Cypate in excess (5X) BSA are similar (difference is insignificant) which again indicates lack of folate specific binding to BSA [Figure 5-3b]. Fluorescence lifetime of cypate in the presence of FR is different from that seen in PBS only [Figure 5-3c]. This indicates cypate interacts non-specifically with FR but the difference between lifetimes of LS872-FR and Cypate-FR confirms that this interaction is different from the folate binding pocket in FR.

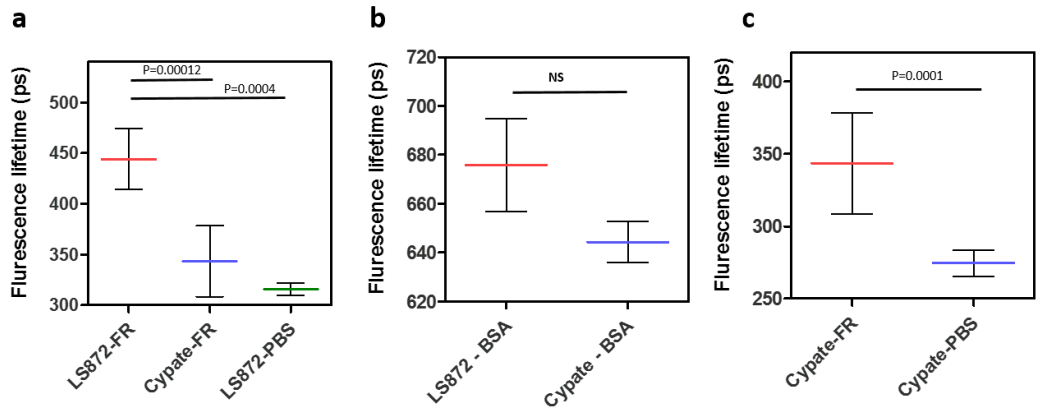

Figure 5-3: (a) Mean fluorescence lifetime of FR bound LS872 shows significant difference from that of FR-Cypate and of LS872 in PBS only. (a) Fluorescence lifetime of BSA-LS872 and BSA-Cypate are similar (difference not significant). (c) Cypate shows some changes in lifetime in presence of FR which can be attributed to non-specific interaction with FR. Plot shows mean±sd (n=3).

5.4.3. Fluorescence lifetime properties of LS872 and Cypate in cells

We wanted to explore if the unique lifetime of FR bound LS872 can be observed in a biological system. For this purpose we incubated FR+ KB cells with LS872 and Cypate (as control) at 37 degrees for 1 hour and performed fluorescence lifetime imaging microscopy. Intensity images of LS872 treated cells show signal from plasma membrane and punctate intracellular, indicating endocytosed material [Figure 5-4a]. In contrast cypate shows no membrane binding [Figure 5-4d]. It shows both diffused and punctate fluorescence inside the cells indicative of internalization of passive diffusion as well as endocytosis. Decay data from multiple KB cells' plasma membrane with bound LS872 could consistently fit to a double exponential decay with showed an amplitude average lifetime τavg = 460 ps ± 30 ps, which coincides to that observed with LS872-FR in the preceding spectroscopic studies. This indicates LS872 on the plasma membrane is bound to FR as expected, and that its unique lifetime is consistent between solution and on cell surface. Intracellular lifetime of LS872 showed two populations. Majority of intracellular vesicles show a high lifetime (τavg = 750 ps ± 40 ps) and few vesicles with low lifetime corresponding to FR bound LS872 (460 ps ± 30 ps) [Figure 5-4b-c]. Interestingly, decay data from cypate from

intracellular vesicles showed a lifetime τavg = 730 ps ± 30 ps similar to the high lifetime component from LS872 [Figure 5-4e-f]. The higher lifetime components from LS872 and its similarity to that of cypate's lifetime indicates absence of FR bound LS872 in these intracellular structures. In other words, in these vesicles the lifetime of both cypate and LS872 is determined the cypate moiety of LS872 and its interactions and not by the binding properties folic acid moiety. The vesicles still showing low lifetime components can be attributed to FR still binding bound LS872. Figure 5-4g shows representative lifetime distribution histogram from the images.

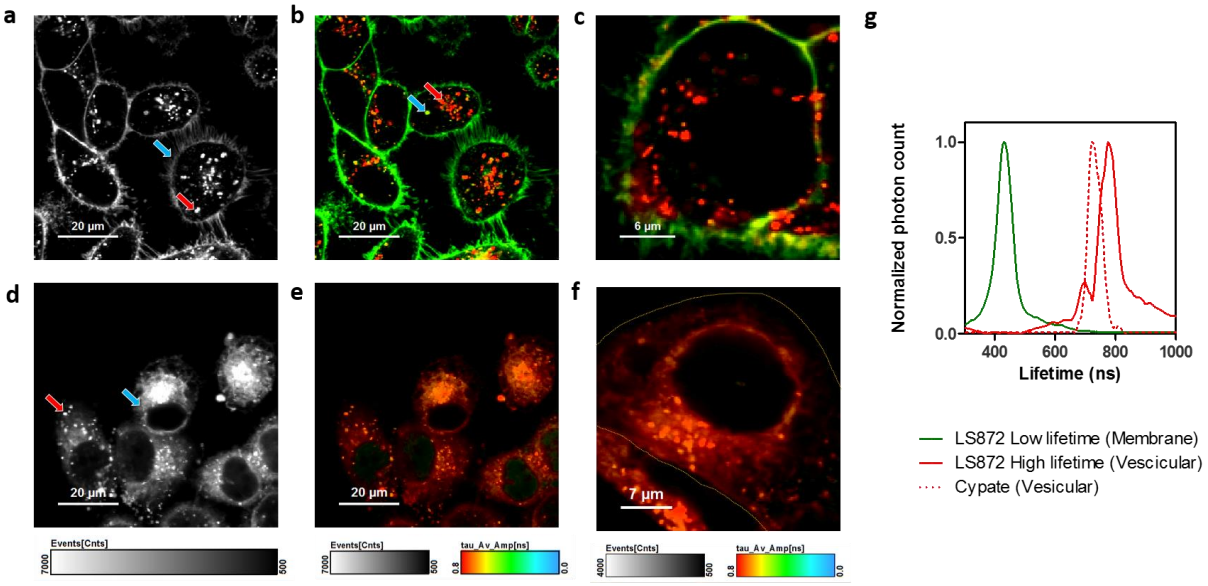

Figure 5-4: Fluorescence lifetime imaging of LS872 (a-c) and cypate (d-f) in KB cells. Intensity images of LS872 (a) shows membrane binding and distinct intracellular vesicular signal, while cypate (d) shows no membrane signal but diffused cytoplasmic and vesicular signal. Lifetime images LS872 (b,c) show distinct lifetimes with lower lifetime components (~460 ps) on the membrane and some vesicles, and a high component (750 ns) restricted to only vesicles. .Lifetime images of cypate show the absence of the lower component. Representative lifetime histograms show the existence bimodal distribution in LS872 and only one lifetime in cypate close to the higher component.

5.4.4. Live cell lifetime imaging of endocytosis of LS872

We then exploited the distinct lifetime associated with FR bound (460 ps) and free LS872 (750 ps) in cells to track them through the endocytosis process in KB cells. In order to limit cellular internalization of only FR bound LS872 (and prevent endocytosis of LS872 in the culture media by non-specific processes such as pinocytosis) we incubated KB cells in the presence of LS872 for 10 min at 4 degrees. We then washed the cells to remove all unbound dye and then replenished it warm media and live cells imaging. Decay data obtained from single cells were fit using a double exponential decay model 460 ps and 750 ns as initial values. Fluorescence lifetime images show cells immediately after washing show only membrane signal corresponding to the lower lifetime or the bound fraction [Figure 5-5a]. Cells till ~1.5 h of warm incubation show only bound fraction components both in the plasma membrane and intracellular structures, and some free fraction components appear intracellularly after that [Figure 5-5b-d]. In early time points (t<2h) several intracellular structures are seen with peripheral fluorescence with lifetime corresponding to bound fraction [Figure5-5e]. These structures appear to be recently endocytosed vesicles with FR bound LS872 still on the membrane. Although they appear to be endocytosed we cannot differentiate if they ate receptor mediated or pinocytosis/phagocytosis. A plot of the relative amplitudes of the free and bound fraction show changing of the bound fraction to free fraction over time.

5.5. Discussions

We have developed a fluorescent molecular imaging agent that shows distinct fluorescent lifetime depending upon its binding state with the targeted molecule. We exploited lifetime sensitivity of the probe to image its endocytosis and quantified changes in the bound and free fraction of the imaging agent over time in cells. We showed that the imaging agent LS872 remains bound to the

target protein FR in internalized fractions till about 2 h and them free fraction begin to appear. A

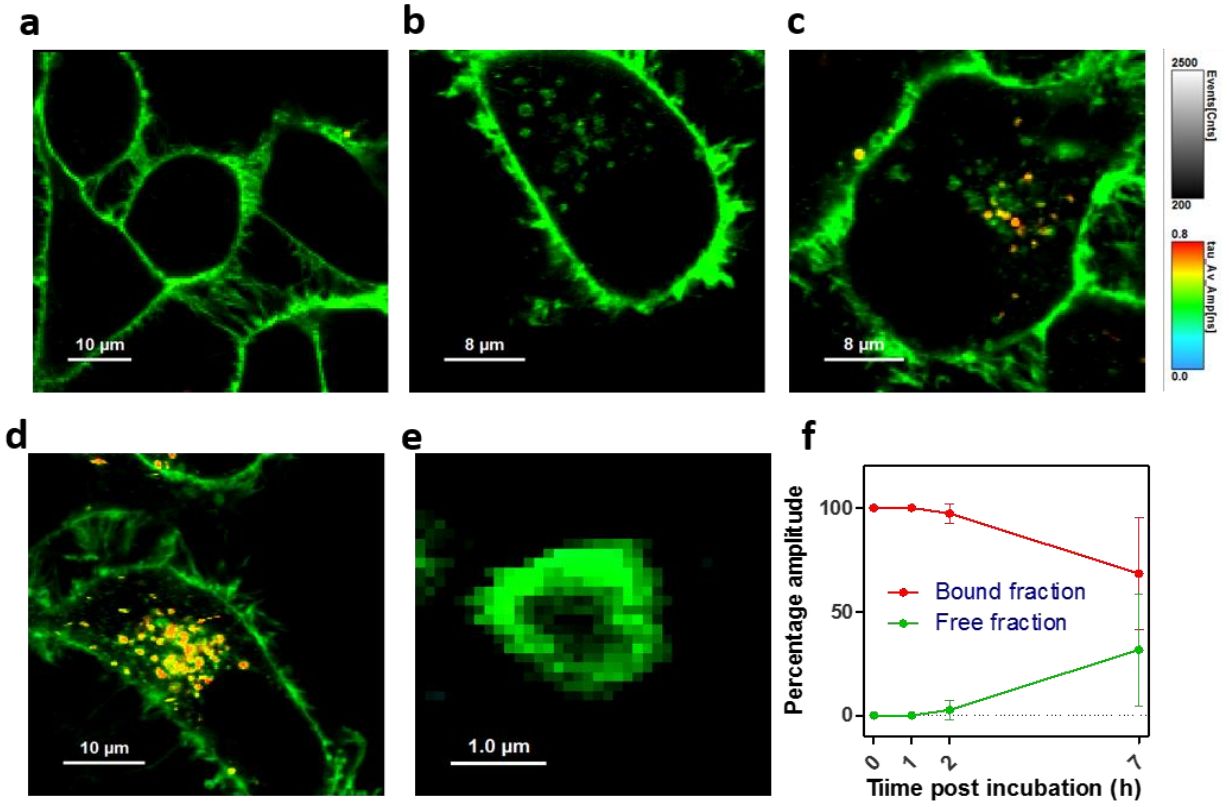

Figure 5-5: Tracking receptor mediated endocytosis of LS872 using fluorescence lifetime imaging (a-d). The lower lifetime component ~0.46 ns in green shows FR bound LS872 while any higher lifetime indicates presence of free LS872. In early time points several intracellular structures with only peripheral signal corresponding to the bound fraction are observed (e). Changes in free and bound fraction of LS872 in cells over time (f), mean ± sd (n=3).

comparison of cell images with LS872 incubated at 37 degrees for 1 h to that incubated at 37 degrees after washing of free LS872 shows considerably more of the free fraction in the former. This indicates that this free fraction is not from the LS872 fallen off from the internalized FR-LS872. They can be attributed to internalization of free LS872 by a non-specific process such as pinocytosis. A similar approach can be translated into *in vivo* imaging and tissue histopathology where by lifetime values will indicate specific and nonspecific uptake of molecularly targeted probes.

5.6. Conclusions

We have developed a fluorescent molecular making agent that shows distinct fluorescent lifetime depending upon its binding state with the targeted molecule. We exploited lifetime sensitivity of the probe to image receptor mediated endocytosis of the probe and quantify changes in the bound and free fraction of the imaging agent over time in cells. A similar approach can be translated into *in vivo* imaging where by lifetime values will indicate specific and nonspecific uptake of molecularly targeted probes.

In the previous chapters we have explored and applied various properties of the fluorescence phenomena to develop imaging agents and applied them to study biological and pathological processes. In the next chapter we will combine fluorescence with nuclear imaging and explore multimodality imaging of diseases.

Chapter 6

Broad spectrum multimodal (PET/Optical) tumor targeting imaging agent

6.1 Introduction

In the previous chapters, we have worked on various type of fluorescence molecular probes and exploited complementary properties of fluorescence phenomena for imaging. Due to many advantages such as high sensitivity, possibility of biological targeting, cost-efficiency, lack of ionizing radiations and high throughput operations optical imaging in general, and fluorescence imaging, in particular, is rapidly moving into clinical settings. There are several examples of fluorescent agents to provide image guidance during surgical procedures and perfusion studies.[112] While fluorescence imaging has the capability to provide rapid high sensitivity imaging, it is not equipped to provide whole body information at an organism level and thus cannot suffice as a diagnostic tool due to limited of depth penetration in biological tissue. One way to circumvent the shallow penetration of light using optical methods, is to develop multimodal imaging approaches by incorporating a radionuclide for nuclear imaging into a fluorescent imaging agent. In this Chapter we will discuss the development of a multimodal analogue of a broad spectrum fluorescent imaging agent LS301. Recently developed in the lab, LS301 is a small molecular NIR fluorescent imaging agent with a cyclic peptide targeting moiety. It has a been shown to target tumors of various kinds tested in the lab in cell lines, animal models and patient models of cancers of the breast, lungs, prostrate, ovarian, pancreas as well as lymphoma and leukemia.

6.2 Materials & Methods

6.2.1 LS301 and LS811

The broad-spectrum tumor targeting NIR fluorescent agent has been described in previously published studies.[113] To make it dual modal, an FDA approved metal ion chelator DOTA was conjugated to the free carboxylic acid group of NIR dye cypate in LS301. The resulting molecular is LS811.

6.2.2 Cold Indium (III) and copper (II) labeling of LS811

A 240 µl solution of 40 µM LS811 was prepared in 20% DMSO in 0.1 M ammonium acetate buffer, pH 5. DMSO was added to enhance solubility of the compound in the buffer. Indium (III) chloride was added to this solution at a final concentration of 80 µM. the resultant was incubated at 70 °C with frequent shaking for one hour. For purification, the cold labelled compound was purified using a waters sep-pak C18 plus light cartridge (WAT023501). The catridge was activated by passing water (0.1 %TFA) and kept for ~30 min. The labeling mixture was passed through it. The compound was eluted in acetonitrile (0.1 %TFA) and dried in lyophilizer overnight.

For cold copper (II) labeling, a 240 µl solution of 40 µM LS811 was prepared in 20% DMSO in 0.1 M ammonium acetate buffer, pH 5.5. DMSO was added to enhance solubility of the compound in the buffer. Copper(II) sulphate was added to this solution at final concentration of 80 µM. The resultant was incubated at 43 °C with frequent shaking for 30 min.

6.2.3 In^{111} labeling and Cu^{64} labeling of LS811

To 470 µCi in 100 uL, 92 uL of buffer to it, 0.1 M ammonium acetate buffer, pH 5 was added.

LS811 (30 ug) was prepared in 48 uL DMSO. This solution was added to 192 uL of In 111 chloride in 0.1 M ammonium acetate buffer, pH 5. This mixture was incubated with shaking for 1 hour at 70 degrees C. After labeling the product was purified using a Waters sep-pak column as in cold-labeled case. The eluent was dried by blowing nitrogen and dissolved in 0.5% MSA in PBS.

To 5µg LS811, 1.0 mCi ^{64}Cu was added in 100µl 0.1 M ammonium acetate buffer, pH5.5 buffer. This mixture was incubated at 45 degree C for 15 min. The mixture was diluted in 0.5% MSA in PBS for injection.

6.2.4 Animal models

All animal studies were conducted according to protocols approved by the Washington University Animal Studies Committee. For LS811 tumor targeting, murine pancreatic cancer (KPC, courtsey Denardo Lab, WUSM) were grown (Charles River Laboratories, Wilmington, MA) by subcutaneous injection of 1 million cells in the right flank of 8-week old male NCR nude mice. For multimodal imaging (with ^{111}In-LS811 and ^{64}Cu-LS811), a spontaneous cancer model PyMT mice with sporadic breast cancer was used. For multimodal imaging (with ^{111}In-LS811) in a subcutaneous tumor xenograft model, 1 million 4T1-luc-GFP cells (courtesy Weilbaecher Lab, WUSTL), were injected cells in the right flank of 8-week old female BALB/c Mice (Charles River Laboratories, Wilmington, MA). Tumors were allowed to grow to ~0.5 min size.

6.2.5 Multimodal imaging

In^{111}-LS811 (160 µCi) was injected into PyMT tumor bearing mice which were imaged till 24 h post injection. Nuclear imaging a performed on the NanoSPECT/CT (Mediso Medical Imaging Sytems) machine and NIR fluorescence imaging was done on the Pearl *in vivo* imager (LICOR). For 4T1 –luc-tumors, each mouse received In^{111}-LS811 (250 µCi) followed by similar imaging.

For ^{64}Cu-LS811, about 111 µCi each was injected three PyMT mice. NIR fluorescence imaging was conducted on a Kodak *In vivo* Multispectral system System (Bruker).

6.3 Results

6.3.1 Imaging agent:

The broad spectrum tumor targeting NIR fluorescent agent has been described in previously published studies (Figure 6-1a).[113] To make it dual modal, an FDA approved metal ion chelator DOTA was conjugated to the free carboxylic acid group of NIUR dye cypate in LS301. The resulting molecule is LS811 (Figure 6-1 b)

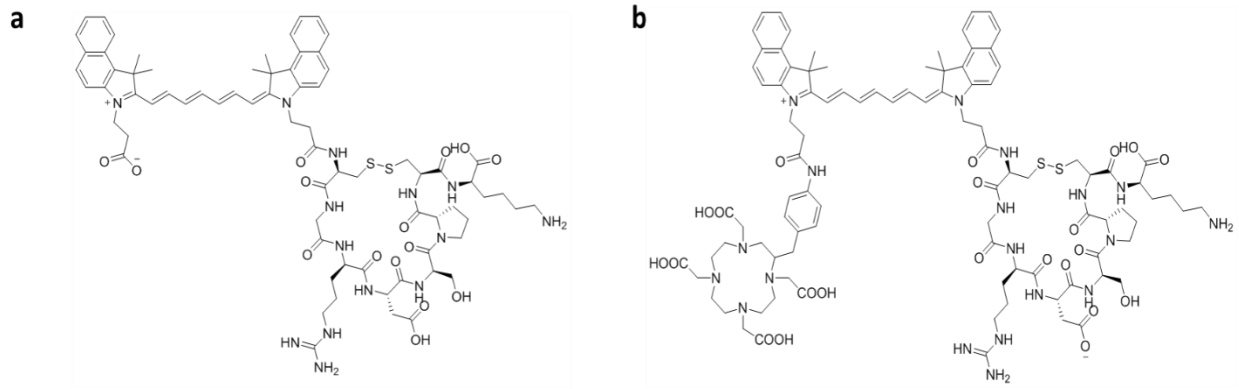

Figure 6-1: Molecular structures of near infrared fluorescent (NIR) broad spectrum tumor targeting agent LS301 (a) and its PET analogue LS811 (b).

6.3.2 Tumor targeting ability of LS811:

LS811 formulation in increased concentrations of mouse serum albumin (MSA) resulted in increased fluorescence indicating better solubility of the molecule (Figure 6-2a). Hence a solution of LS811 in 0.5% MSA was used for animal injection. Upon injection, similar tumor uptake of LS811 in a subcutaneous model of pancreatic cancer indicates preservation of tumor targeting property after addition of radionuclide chelating moiety (Figure 6-4b). LS811 in this study with

one mouse shows much higher kidney uptake and liver uptake as well at post injection 23 hours showing more compound being targeted through clearance routes and lesser bioavailability and can be an undesirable side-effect of DOTA moiety (Figure 6-2c).

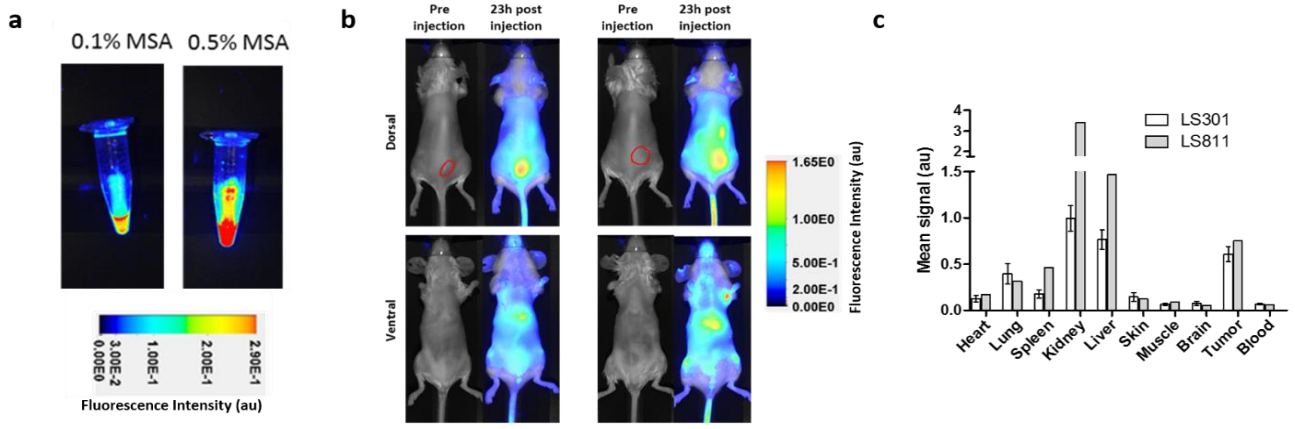

Figure 6-2: Tumor targeting capability of LS811. (a) Increased amounts of mouse serum albumin (MSA) leads to increase in fluorescence signal indicating better solubilizing of LS811 for animal injection. (b) Representative *in vivo* images of LS301 (left) and LS811 (right) in KP2-luc-GFP pancreatic cancer xenograft models at 23 h post injection. Red circles indicates tumors. (c) Corresponding bio-distribution at post injection 23 hours for LS301 (mean ± sd, n=3) and LS811 (n=1).

6.3.3 Cold labeling of LS811

To optimize radiolabeling conditions we first performed labeling of LS811 with cold indium (III) chloride and copper (II) chloride. LCMS analysis was used to confirm incorporation of the indium (II) and copper (II). The absence of blue shift in absorption and no fluorescence quenching after labeling with indium indicates no or minimal dimerization. While incorporation of copper (II) resulted in fluorescence quenching as observed in earlier chapters, the lack of blue shift and absorbance indicated minimal dimerization under labeling conditions (Figure 6-3).

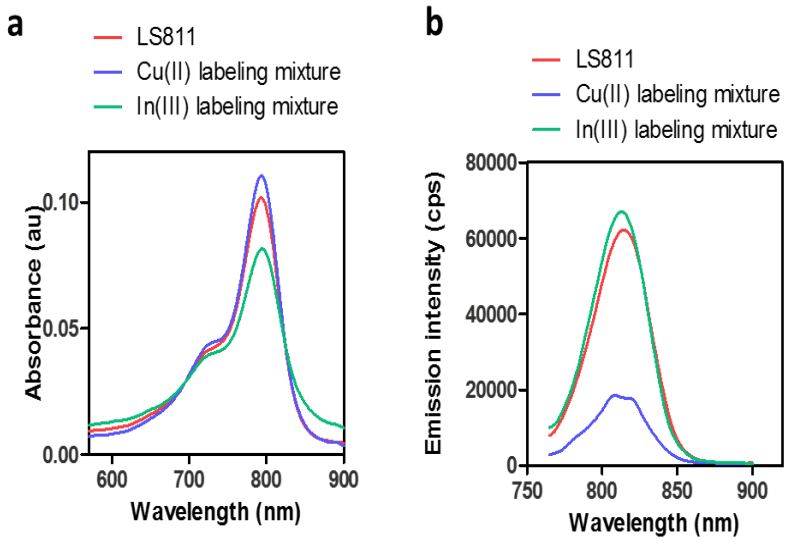

Figure 6-3: Absorption (a) and emission (b) spectra of LS811 and the cold labeling reaction mixtures with Cu(II) and In(III), diluted in DMSO. Lack of blue shift in absorbance indicates no or minimal dimerization. Lack of fluorescence quenching in In(III) labeling confirms no corresponding dimerization. Fluorescence quenching is observed in Cu(II) labeling can be attributed to the effect of the ions.

6.3.4 *In vivo* tumor imaging with In^{111}-LS811

For preliminary study, one PyMT mouse with spontaneous breast cancer was used. Dual imaging shows simultaneous high NIR and PSECT signal from obvious tumors as well as sporadic regions from the mammary fat pad as expected to be cancerous in such an animal model (Figure 6-4a-e). There is a high signal from kidney and liver as observed with the previous studies with unlabeled LS811. Localized high signal from region in the femoral bone was observed in both NIR and SPECT images and may indicate metastasis being pick up (Figure 6-4f). NIR and radioactive bio-distribution data show a high tumor to muscle ratio of 4 (NIR signal) and 4.2 (radioactivity) at 24 hours post injection (Figure 6-4f, g).

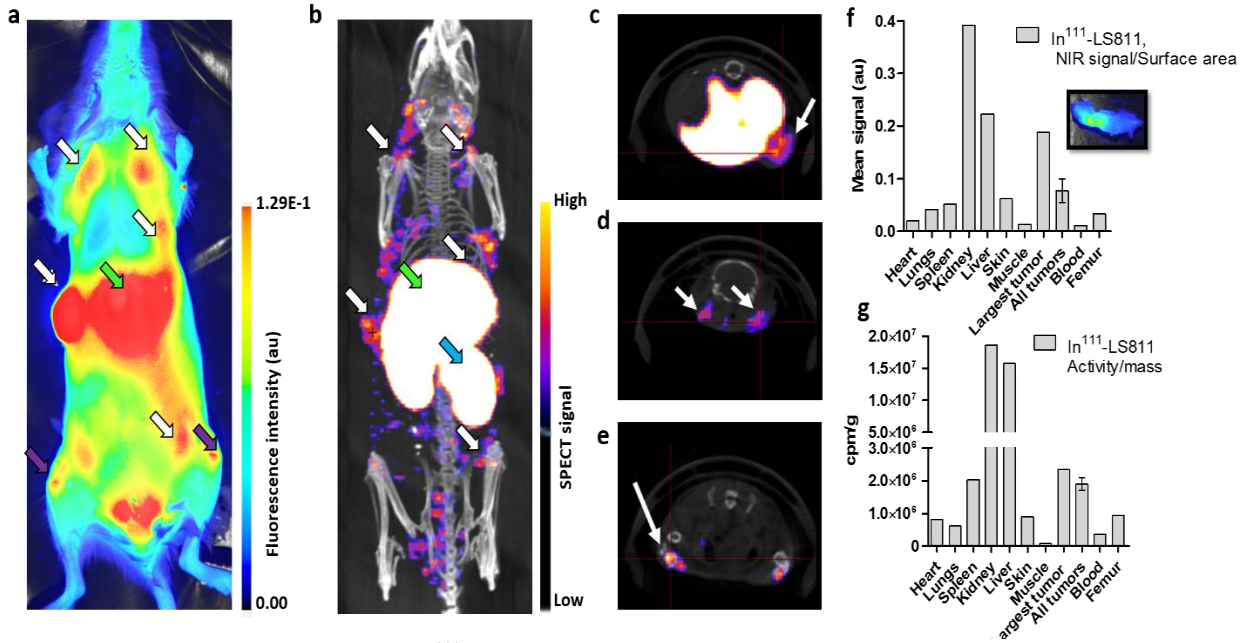

Figure 6-4: Multimodal imaging of In^{111}-LS811 in PyMT spontaneous breast cancer mouse. (a) NIR image of dorsal side at 27 hours post injection showing high signal from tumors in mammary fat pads (white arrows) and liver (green arrow). (b) SPECT/CT image at post injection 23 hours showing high signal from tumors (white arrows), liver (green arrow) and kidney (blue signal). Cross-sectional SPECT/CT images showing localized signal from largest tumor by the liver (c), other smaller tumors near the chest (d) and intra-femoral signal (e). Bio-distribution of In111-LS811 at 27 hours post injection using NIR signal (mean signal/surface area) (f) and counts per minute per gram of tissue (cpm/g) (g). Error bars in tumor signal indicates mean ± sd from multiple tumors form same mouse.

For further studies, BALB/c mice with subcutaneous 4T1-luc-GFP tumors were used. In^{111}-811 showed high tumor uptake in these mice (Figure 6-5a). Bio-distribution (radioactivity) at 24 h post injection showed a tumor to muscle ratio of 10 (mean, n=2) and tumor signal were 6.2 % injected dose/g (ID/g) (mean, n= 2) (Figure 6-5b).

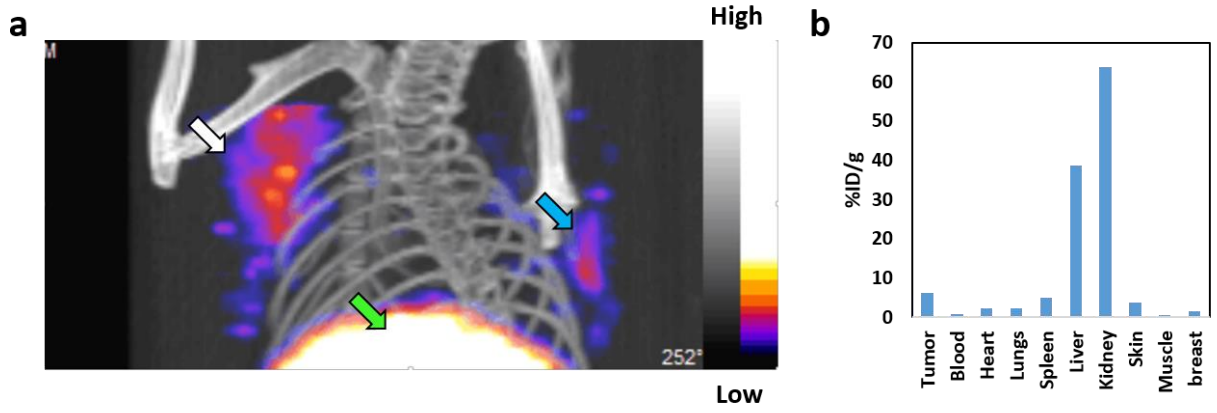

Figure 6-5: In^{111}-LS811 imaging in a 4T1lucGFP xenograft model. (a) Representative SPECT/CT image of the thorax showing high signal from tumor (white arrow, liver (green arrow and some signal from mammary fat pad (blue arrow). White bar represents CT signal and rainbow bar represents SPECT signal. (b) Bio distribution at 24 h post injection from a representative mouse.

6.3.5 *In vivo* tumor imaging with Cu^{64}-LS811

In a PyMT model of spontaneous breast cancer, dual imaging (NIR and scintigraphy) shows simultaneous high signal from obvious tumor and kidneys and liver (Figure 6-6a-d). Tumor to muscle ratio (radioactivity) from all tumors 24 h post injection was 8.7 (mean, n = 9 tumors, in 3 mice).

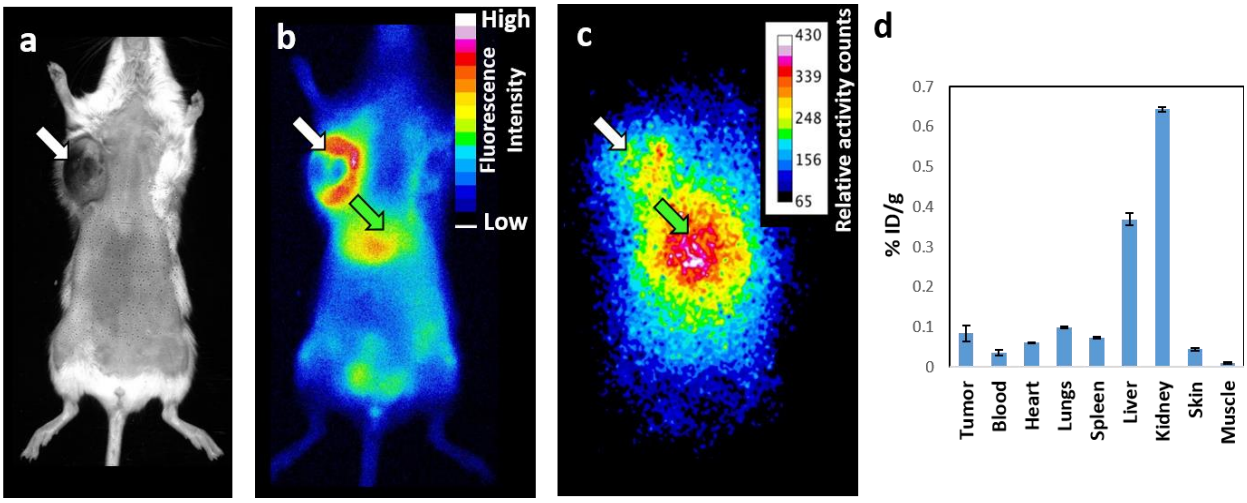

Figure 6-6: *In vivo* tumor imaging with Cu^{64}-LS811. Representative white light image (a), NIR image (b), and un-collimated gamma scintigraphy image (c) of a PyMT mouse at 24 h post injection shows obvious tumor (white arrow, liver (green arrow). (d) Bio-distribution at post injection 24 h (radioactivity, mean ± sd, n=9 tumors in 3 mice).

6.4 Discussions

Fluorescence/SPECT or Fluorescence/PET multi modal imaging agents can be useful for whole body nuclear imaging for initial diagnosis followed by real time NIR image guided surgery if needed. From molecular probe development perspective it is important to evaluate that the biological activity of the imaging agent is preserved after addition of new moieties, which we demonstrated in Figure 6-2. We used mild radionuclide labeling conditions and blew drying with nitrogen (in place of heating or blowing air) in order preserve the peptide and NIR dye moieties. Successful tumor targeting by ^{111}In-LS811was demonstrated in two different tumor models, PyMT and 4T1-luc-GFP. Even though tumor signal was observed with a high tumor to muscle ratio, the non-specific uptake of the probe in the clearance organs kidneys and liver indicates lesser bio-availability of the molecule. Tumor targeting is also shown by ^{64}Cu-LS811 with a tumor to muscle ratio of upto 13. However the %ID/g retained in the organs were all less than 1% at post injection 24 h. This may be due to the well documented *in vivo* instability of ^{64}Cu-DOTA i.e., most for the radionuclide falls of the imaging agent and are cleared by 24 h. Future work includes efforts to introduce additional moieties to enhance blood retention and bioavailability as well as the introduction of alternative radionuclide chelators with greater *in vivo* stability.

6.5 Conclusions

We have developed a SPECT/PET compatible dual modal analogue of broad-spectrum NIR fluorescent tumor targeting agent LS301 by conjugating it to a FDA approved radionuclide chelator DOTA. With this new construct we have successfully performed SPECT/CT and NIR fluorescence imaging with ^{111}In-LS811 as well shown potential for PET/CT and NIR fluorescence imaging with the same agent. Future work will be focused on optimizing probe construct for minimizing non-specific kidney and liver uptake and enhanced stability of radionuclide.

In the next two chapters we will demonstrate the applications of custom fluorescent molecular probes for dynamic imaging, identification and characterization of circulating tumor cells and to longitudinally monitor molecular changes in atherosclerotic plaque development.

Chapter 7

A simple all-near-infrared planar fluorescence imaging platform for identification and size stratification of fluorescent circulating entities

7.1 Introduction

Fluorescence imaging and detection methods have been widely used for basic biomedical research as well as for clinical procedures. The sensitivity of fluorescence detection, availability of a variety of customizable fluorescent contrast agents, and relatively inexpensive instrumentation together makes fluorescence-based methods attractive for addressing pressing biomedical needs. For example, fluorescent imaging and detection strategies have been used for the detection and enumeration of a rare population of cells which play an important role in cancer metastasis,[114] stem cell research,[115] and immunology research.[116] Particularly in cancer, the frequency of occurrence of disseminated cancer cells in the blood circulation holds information about disease progression; having prognostic and predictive values of clinical significance.[117-119] Besides clinical applications, fluorescence based approaches for real time *in vivo* detection of circulating tumor cells (CTCs) and CTC clusters in animal models have proven very useful to study critical steps in cancer progression and for monitoring treatment response. [114,120]

Amongst all fluorescence detection strategies for *in vivo* CTC detection, near infrared (NIR) fluorescence (700nm – 900nm) based methods are being increasingly used as they offer several advantages over visible fluorescence.[121] NIR excitation and emission has greater depth penetration in tissue and blood due to less absorption than visible light. Also, NIR wavelengths have minimal interference from tissue auto-fluorescence. Due to these factors, NIR fluorescence is attractive for *in vivo* detection of CTCs. NIR light may allow for the detection of circulating fluorescent entities with higher sensitivity than using visible light. Additionally, it can image deeper within blood vessels, allowing for analysis of larger diameter blood vessels for faster blood sampling. NIR

fluorescence based methods can be paired with suitable NIR fluorescent imaging agents to allow accurate and rapid studies in animal models *in vivo*. For example, several NIR fluorescent agents (range of optical excitation/emission: 745-785nm/780 – 840 nm) have been described in the recent past which show highly specific accumulation in cancer cells in blood. [122-124] These or similar fluorescent agents can be injected into the blood circulation to selectively label the cancer cells that are present within the blood. Alternatively, an agent could be delivered to a tumor to selectively label tumor cells before they become CTCs, allowing for detection once they escape the solid tumor.

In addition to frequency of occurrence, it has been shown the metastatic potential of CTCs depends greatly on the number and/or type of cells. For example, current data indicates that multicellular aggregates of tumor cells (2 or more tumor cells) may show a much greater potential (up to 50 times) to cause distant organ metastasis than single CTCs.[114,125,126] Therefore it is will be valuable to not only detect and enumerate these entities *in vivo* but also to determine their size to accurately predict their relative potential as a biomarker for metastasis.

In this study, we have designed and validated a simple approach that allows for all near infrared (NIR) planar fluorescence imaging (excitation/emission – 780 nm/ >808 nm) of fluorescent circulating entities. In addition, we developed a simple image processing algorithm that will allow us to measure size of the fluorescent entities from the NIR-video captured. We first validated our imaging method by imaging fluorescent microbeads flowing through a capillary mimicking a blood vessel and demonstrated the performance of our algorithm by accurately detecting their size. To simulate fluorescent CTCs and CTC clusters, we used cells that were pre-labeled with a NIR fluorescent molecular probe which has been shown to target a variety of tumors *in vivo* in mice with high specificity.[127-129] We mixed labeled tumor cells with heparinized whole blood and

imaged them while flowing through our capillary setup. We then estimated and stratified the size of the detected entities. Finally we demonstrated the feasibility of using this approach in mice by imaging the internal thoracic artery of a mouse with flowing NIR fluorescent CTCs.

Our method adds to the existing methods available for fluorescence *in vivo* imaging of CTCs, which has not been previously described for an all-NIR application.[115,130-132] Also, our method uses a planar imaging technique which can be a simpler approach than the standard *in vivo* flow cytometry approaches using confocal or diffuse optics techniques.[123,130] Our simple approach for the size stratification of fluorescent entities in motion can be optimized further and applied to extract size information from videos of fluorescent objects in motion. Mouse imaging highlights that this approach can be executed peripherally or via an implant in a CTC rich region of the circulation with appropriate fluorescent contrast.

7.2 Materials & Methods

7.2.1 Cell Culture and Treatment

All experiments were performed using murine breast carcinoma cell line (4T1-luc-GFP). The cells were cultured in DMEM (Gibco) supplemented with 10% fetal bovine serum and 1% Pen-Strep. To first test preferential uptake of our NIR fluorescent compound in cancer cells, we incubated heparinized porcine blood alone or spiked with 4T1-luc-GFP cancer cells (~5x104 cancer cells per 50 uL blood). We incubated the samples with 10 µM NIR compound, 3 mM added calcium chloride (to enhance compound internalization)) for 2 h at 37 degrees, 5 % atmospheric carbon dioxide. After 1.5 hours of incubation, Hoechst 33342 (5 µg/mL, Thermo Fisher Scientific) was added to the samples stain for nucleus. After a total of 2 h incubation the cells were washed with Hank's Balanced Buffered Solution (Thermo Fisher Scientific) to get rid of non-internalized dyes

and spun down to pellet the cells. The pellet was smeared on glass slides for microscopic visualization. Cells were imaged using an epifluorescence microscope (Olympus BX51), λex/λem = 775nm/845 nm for NIR fluorescence; λex/λem = 480nm/535 nm for GFP; λex/λem = 357 nm/420 nm for Hoechst 33342.

For flow imaging experiments, the 4T1-luc-GFP cells were plated in culture plates in culture media with 20 μM NIR compound, and 3 mM calcium chloride (to enhance compound internalization) and incubated for 24 h at (37˚C, 5% atmospheric CO2). Cells were washed and imaged using an epifluorescence microscope (Olympus BX51), λex/λem = 775nm/810 nm LP. After the initial images were obtained, cells were treated with trypsin for ~4 min and re-suspended in either PBS or heparinized porcine blood. To obtain single cell rich suspensions, post trypsinization cells were pipetted (1mL pipette tip) gently ~20 times and filtered through a cell strainer (40 μM mesh size). In contrast, to obtain clusters rich suspension cells were incubated in trypsin for ~1min and exposed to minimal pipetting.

7.2.2 *In vitro* Imaging

In order to test our method of detecting CTCs, we developed an imaging setup consisting of a microscope and an excitation light source. The microsphere in water, tumor cell in media, or tumor cell in blood mixture was passed through a 0.015 in ID x 0.033 in OD polyurethane tube (PU-033, SAI Infusion Technologies) at a flow rate of 3 mm/sec. Imaging was conducted using a microscope (Leica MZ10F) at 80x magnification. Calibration imaging was conducted using Fluoresbrite® YG Microbeads (Polysciences, Inc.) with a 10 μm diameter because NIR microbeads in a cellular diameter were not available. Excitation was provided via a 460 nm LED (ThorLabs), with a 515 nm LP filter, for microsphere imaging. Excitation light power was measured at 0.8 mW/cm2. NIR imaging was conducted using a 793 nm laser (BWT Beijing), set to a power output of 10 mW/cm2,

and the emission light was filtered using an 808 nm LP filter. The *in vitro* imaging configuration is shown in Figure 7-1a. The microbeads were imaged using the microscope input light port instead of external illumination. Image files were recorded in video files using a NIR sensitive camera (Fluorvivo 1500 BG, INDEC Biosystems) with an exposure time of 100 msec.

7.2.3 *In vivo* Imaging

In vivo imaging was conducted using the same microscope as *in vitro* imaging, however the light configuration was modified (Figure 7-1 a,b). Excitation was provided via the microscope light port using a 780 nm LED (ThorLabs), with an 808 nm LP filter. Excitation light power was measured at 7.3 mW/cm2. Internal thoracic artery imaging was conducted with an exposure time of 500

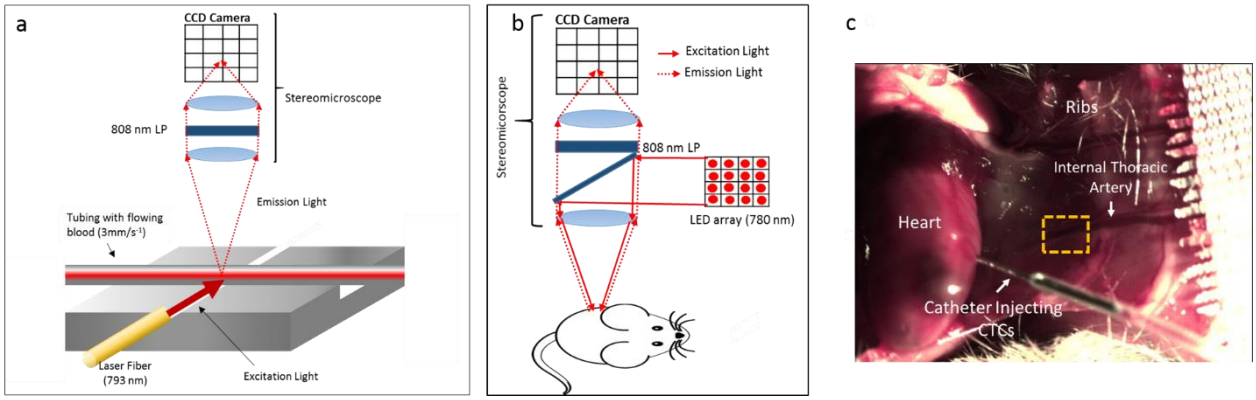

Figure 7-1: a) *In vitro* setup showing the optical configuration. An external light source was used to illuminate tubing containing CTCs in either PBS or blood. The image was magnified using the objective and recorded in video files using a NIR sensitive CCD. b) Mouse imaging setup showing LED illumination through the microscope. c) Photograph of mouse imaging using internal thoracic artery while fluorescent cells injected in the left ventricle using a catheter. Yellow box shows the field of view captured while imaging.

msec. PBS (50 ml) containing CTCs was injected into the left ventricle of a sacrificed mouse while the heart remained beating. Cells were imaged as they were pumped from the heart into the circulation (Figure 7-1 c).

7.2.4 Algorithm to Distinguish CTCs from Cell Clusters

We developed an image processing algorithm to analyze video recordings of circulating objects in our imaging setup. We developed our algorithm first using fluorescent tumor cells in media before moving to cells in blood and then *in vivo* imaging. The algorithm was validated using microbeads with known diameters. The algorithm analyzes the video files frame-by-frame with the user selecting a vertical line within the first frame (Figure 7-2a). That vertical line is used frame-by-frame to generate intensity profiles along that line (Figure 7-2b). The user inputs a threshold value, above which any pixels are considered an object. Subsequent pixels along the line are followed until the values rise above and then fall below the threshold. The length of subsequent pixels above threshold are the object height (*h*). The midpoint of the pixels above the threshold is recorded as the midpoint of a unique object. The same line is examined in the subsequent frame, and if the midpoint is within a certain distance of the first midpoint, it is considered the same object. The object is tracked until a frame is reached where an object with the same midpoint is absent, thus ending the object.

The time for an object to completely pass through the vertical line is captured using the width in time (τ) as calculated using Equation 1. Where *fn* is the number of frames, and *fr* is the frame rate. The velocity (*v*) is calculated by assuming that the distance the object is occupying in the y-dimension is similar to the distance in the x-dimension, and then using Equation 2. The object area (*A*) is calculated by multiplying the height by the physical width (*w*) in Equation 3. The object's physical width is a function of the velocity and time for the object to pass, so it is estimated using Equation 4, which is substituted into Equation 3, to derive Equation 5. Equation 5 is then used to calculate the relative object area. The term relative is applied in this case because the area is represented by a height multiplied by a width, using the simplifying assumption that the object is

rectangular. However, even with this assumption, the relative sizes of single cells and cell clusters can be compared.

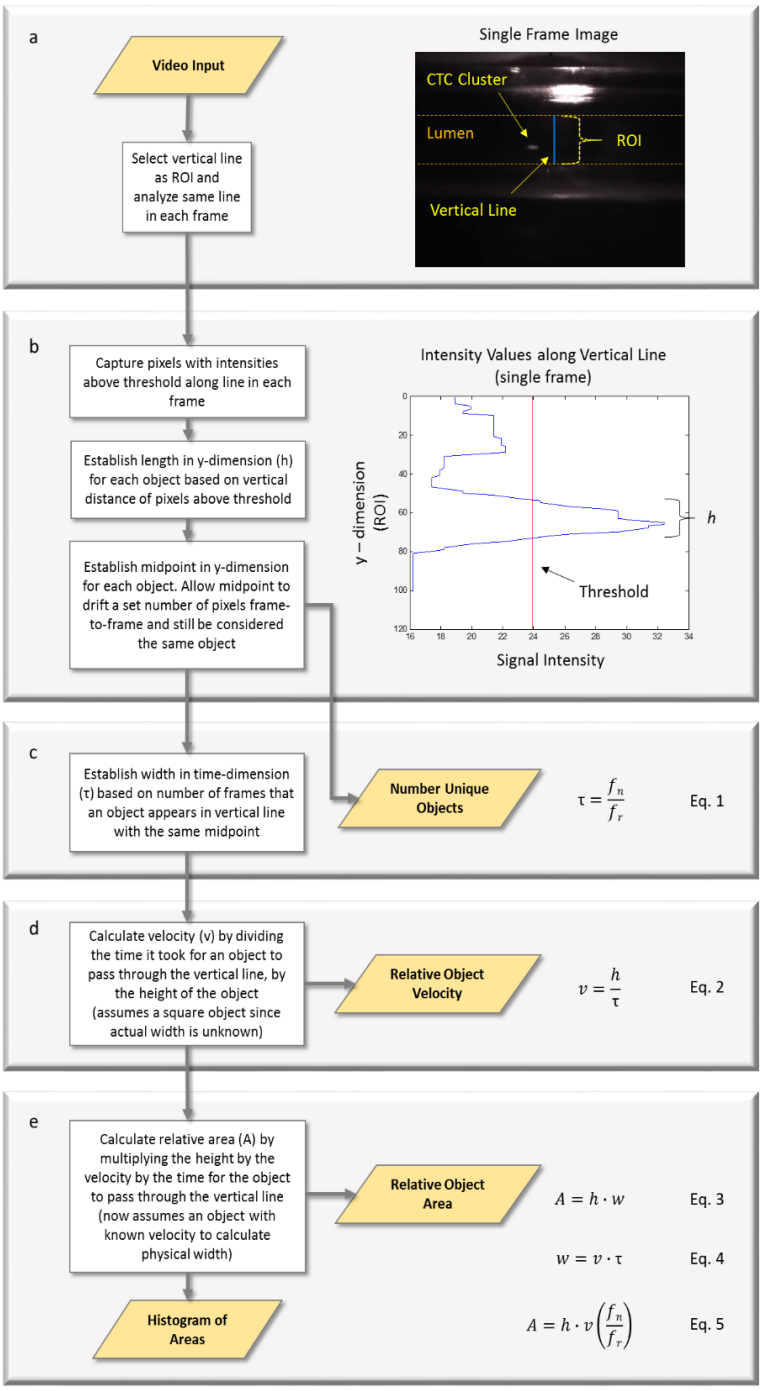

Figure 7-2: a) Single frame showing a CTC in media. b) Signal intensity along a vertical line for a single frame. c) Method for estimating the number of objects passing through the vertical line. d) Method for detecting the relative object velocity. e) Method for calculating the relative object 2D area.

7.3 Results

7.3.1 Labeling cancer cells with NIR fluorescent compound

Fluorescence microscopy images of blood smears post incubation with our NIR fluorescent compound (Figure 7-3a) showed no internalization in both RBCs and WBCs (Figure 7-3b,c). Preferential uptake of the compound was observed in the GFP+ cancer cells that were added to blood before incubation with the compound (Figure 7-3 d,e). At this time we have not investigated the sensitivity and specificity of this compound for cancer cells in blood or mechanism of preferential uptake. For developing our method, we used this NIR compound to represent any NIR imaging agent that may be used for imaging or detecting CTCs. In order to obtain enhanced NIR contrast for imaging in flowing blood, we pre-labeled cancer cells then mixed them with blood to simulate fluorescently labeled CTCs in our experiments (Figure 7-3f).

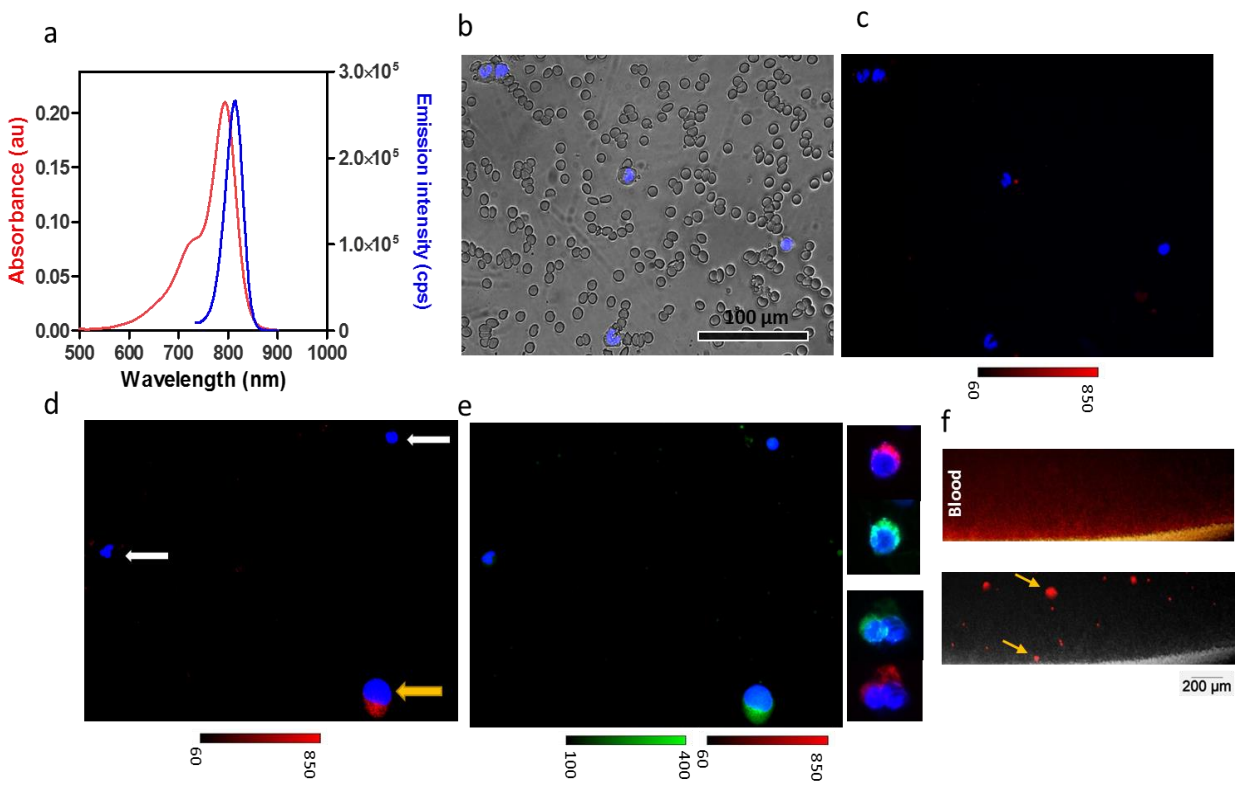

Figure 7-3: a) Absorption and emission spectra of our NIR fluorescent compound in DMSO. b) Overlay of brightfield image with nuclear stain (Hoechst 33342, Blue) for blood incubated with NIR compound showing both RBCs (anucleate) and WBCs (nucleated). c) In the same field of view, no blood cells shows NIR signal (red). d) Overlay of NIR (red) and nuclear stain (blue) for a blood sample spiked with 4T1-luc-GFP cancer cells before incubation shows NIR signal only in the cancer cell (yellow arrow) but not white blood cells (white arrows). e) Cancer cells can be distinguished from blood cells by their GFP signal (green). Other similar cancer cells/clusters identified with NIR and GFP signal. f) Low magnification image of a drop of blood that was spiked with pre-labeled cancer cells as used in the experiments. Top panel shows color image of blood, bottom panel shows overlay with NIR signal (red) showing the fluorescent cells/clusters of various sizes (yellow arrows).

7.3.2 Algorithm validation with fluorescent microbeads

Our algorithm was validated using fluorescent microbeads in media. We selected microbeads with diameters similar to that of our CTCs. Figure 7-4a shows a frame containing multiple microbeads, with the relative fluorescence intensities frame-by-frame (along the vertical line) in Figure 7-4b. The relative velocities of each object detected are shown in Figure 7-4c overlying the intensity map. The relative areas are represented visually as a function of time in Figure 7-4d, and the histogram of the

calculated areas is shown in Figure 7-4e. The microbeads had a diameter of 10 µm, and using the algorithm area calculation method the idealized area would be 100 µm^2 (assumes 2D square geometry). The algorithm histogram predicted object areas clustered around 100 µm^2, thus confirming the accuracy of the algorithm. The detected object heights were output and plotted in Figure 7-4f, and they closely represent the microsphere diameter values, with a mean value of 10.81 ± 6.643 µm. Some of the causes of error may have been from multiple spheres passing at the same time, background fluorescence, and out of plane scattered light.

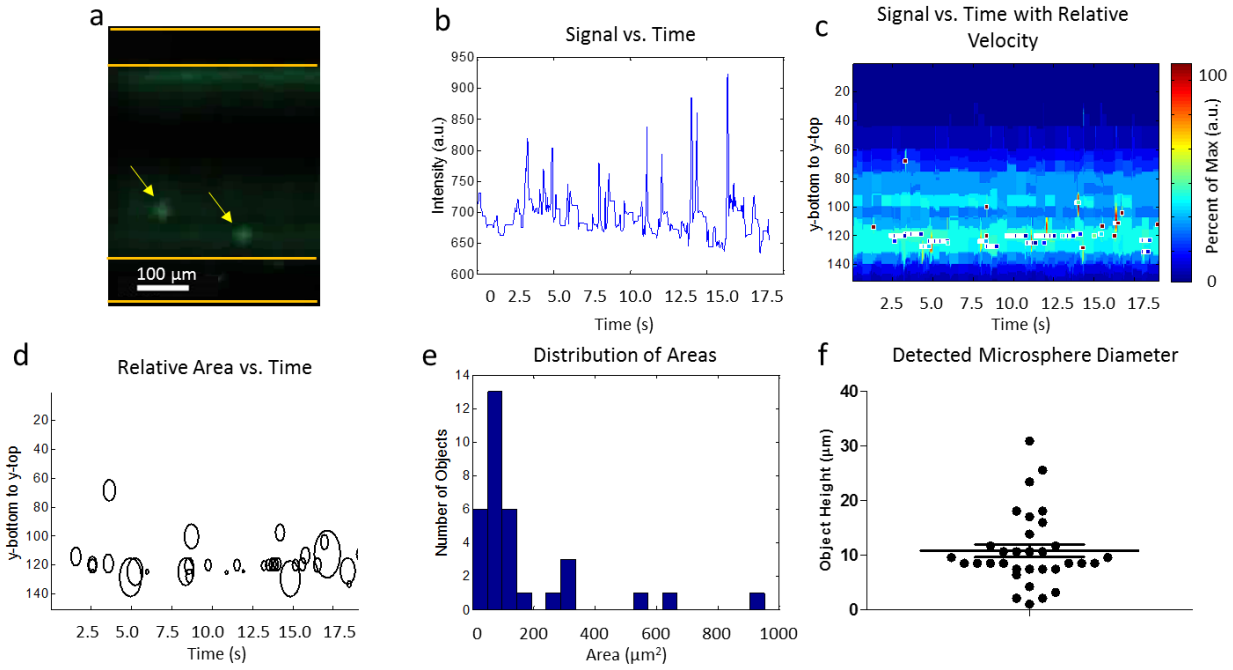

Figure 7-4: a) Circulating green microbeads in media (yellow arrows). Yellow lines indicate capillary wall. b) Microsphere signal intensity vs. time crossing over the vertical line of interest. c) Relative object velocity. Line of squares indicates the same object, and the length of the line of squares indicates the duration that the object took to pass through the vertical line. The color of the squares represents the relative velocity (red max and blue min). d) The relative object areas shown visually over time. e) Histogram of the distribution of object areas over the full time of imaging. f) Plot of individual microsphere diameters detected using the algorithm.

7.3.3 *In vitro* imaging and size stratification of flowing cells and clusters

The goal of our algorithm was to differentiate small individual CTCs from large CTCCs. We tested our detection system and post-processing algorithm by imaging NIR fluorescence labelled cancer

cells and clusters first in PBS then in heparinized blood. To accomplish this, we first suspended individual cells in media via vigorous pipetting during re-suspension, then we compared our findings to larger clusters with reduced pipetting. Figure 7-5a shows a video frame containing a fluorescent CTC passing through the field of view. Figure 7-5b is an intensity map of the vertical line across all of the video frames under analysis (sub-frames). The relative velocities for each object detected were represented by boxes overlying the intensity map (Figure 7-5c), and the relatives areas are represented in Figure 7-5d. The distribution of object areas observed within the sub-frames analyzed were displayed in a histogram (Figure 7-5e). The algorithm was able to detect 10 objects out of the 13 objects observed in the video for a sensitivity of 76.9%. Some objects were below the fluorescence intensity threshold and were not detectable. We then analyzed our video containing large clusters. In this video the clusters were traveling faster at the beginning of the video, and then slower over time. This trend is reflected in the relative velocities reducing at later time points (Figure 7-5f). The relative areas were significantly larger than the previous video, as evident in Figure 7-5g-h. Because the cells were moving very rapidly at the beginning of the video, it was not possible to discern the sensitivity of detection. Of the clusters that were detected the algorithm was able to detect a difference in size as compared to individual cells, with the clusters much larger than the individual CTCs.

Next we imaged simulated CTCs and CTC clusters in blood to determine if our detection system was capable of detecting fluorescence in a scattering medium. The blood was opaque in appearance, and the RBCs scattered our excitation light (Figure 7-6a). We were able to obtain video as shown in Figure 7-6b, however individual changes in intensity due to fluorescent objects were not as readily apparent as when imaging through media. We ran our algorithm to return Figure 7-6c which shows the detected cells and velocities, and Figure 7-6d,e show the areas of the CTCs and

CTC clusters detected. We also ran the post-processing algorithm on videos of our control groups of blood only, and blood with non-fluorescent CTCs and CTC clusters, and the algorithm did not return any detected object. Therefore, the algorithm was able to detect the presence of fluorescent CTCs and CTC clusters though blood, although the relative areas cannot be verified visually do to the reduced contrast between the fluorescent cells and blood.

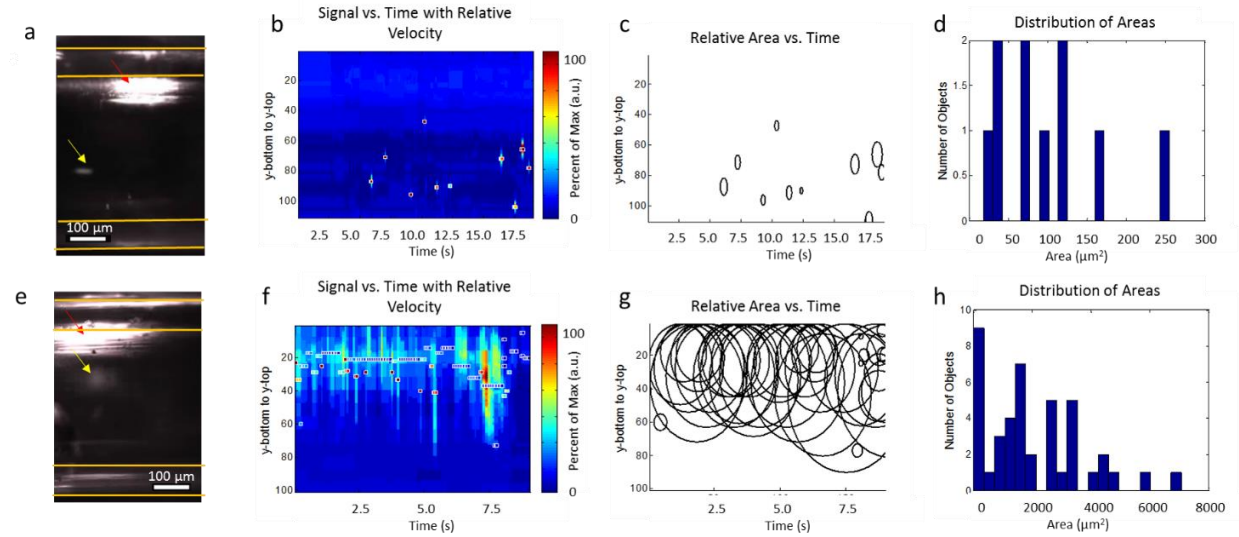

Figure 7-5: a) NIR image of a simulated CTC flowing in PBS (yellow arrow). Yellow lines indicate capillary edge. Red arrow shows reflection of the excitation light which was avoided while choosing line of interest of running the algorithm. b) Relative velocity of each CTC detected. c) Relative area of each CTC detected. d) Histogram of the object areas for CTCs. e) NIR image of a simulated CTCC flowing in PBS (yellow arrows). f) Relative velocity of each CTCC detected. g) Relative area of each CTCC detected. h) Histogram of the object areas for CTCCs.

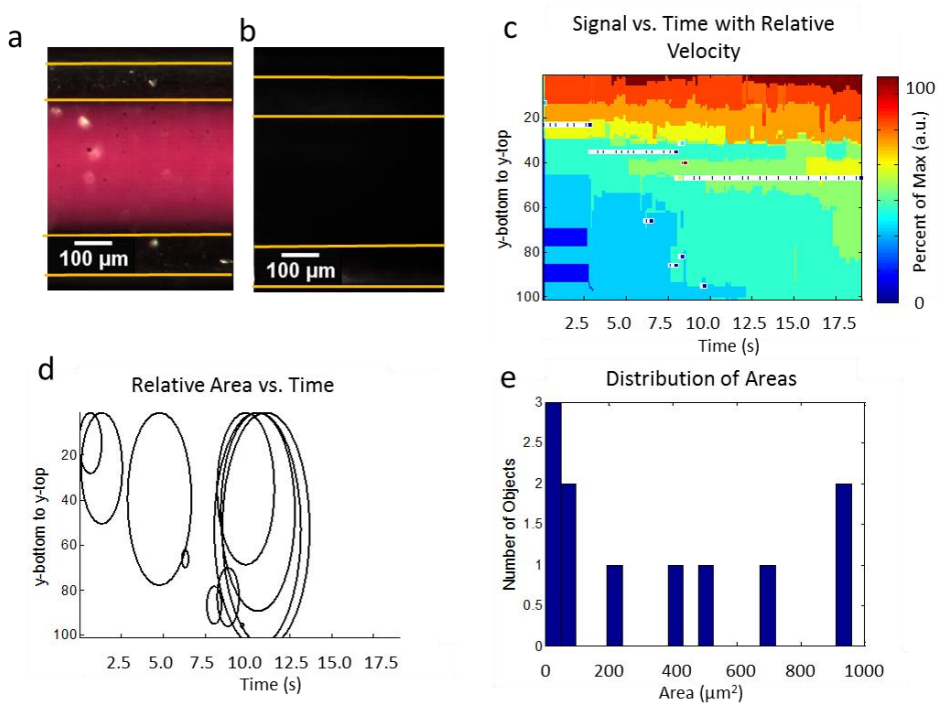

Figure 7-6: a) Color image of blood mixed with fluorescent CTCs and CTC clusters in the capillary. b) NIR image of the same sample. Yellow lines indicate capillary boundary. (c) Relative velocity of CTCs and CTC clusters in blood as detected using the algorithm. d) Relative areas of CTCs and CTC clusters in blood. e) Histogram of the object areas detected.

7.3.4 Mouse imaging and size stratification of flowing cells and clusters

Next we simulated CTCs and CTC clusters by intra-cardiac injection of pre-labeled cells/clusters in a mouse via a left ventricle catheter then imaging the fluorescent in the objects in the internal thoracic artery. Figure 7-7a shows a color image of the internal thoracic artery of a mouse. To correctly focus and find edges of the blood vessel, we first injected the NIR compound only. We then injected our CTCs and CTCCs into the heart and imaged the downstream artery to visualize the movement through the circulation. Figure 7-7b shows a representative snapshot with a fluorescent object flowing through field of view. Edges of the blood vessel (blue dashed line) are identified by fluorescence from the dye injected. Figure 7-7c shows the contrast enhanced view of the same. During our experiment we first injected only cells. A single CTC was visible as it passed

through the field of view, and it was detected using our algorithm (Figure 7-7d,e). The estimated object area was 113 μm^2, supporting the detection of a single CTC rather than a cluster (Figure 7-7f). We next injected cell clusters into the heart and repeated our imaging and analysis (Figure 7-7g,h). The algorithm detected the presence of multiple objects of larger areas than single CTCs, suggesting the presence of clusters (Figure 7-7i).

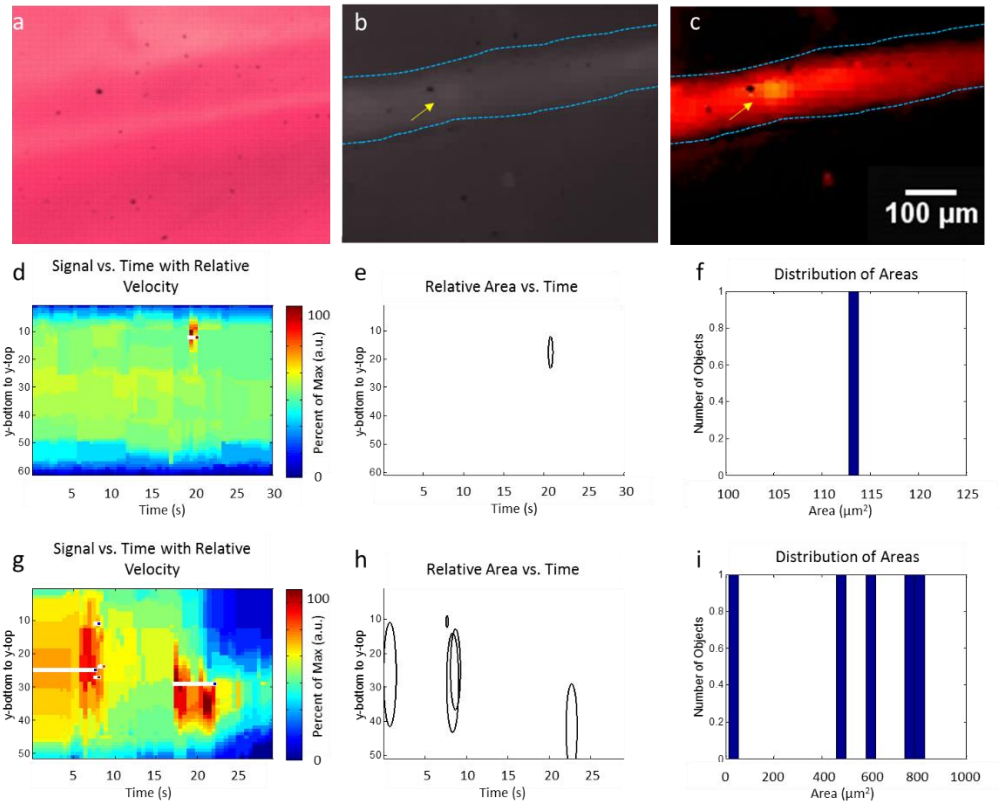

Figure 7-7: a) Bright field image of internal thoracic artery. b) Representative NIR image snapshot showing edges of blood vessel (blue dashed line) and a fluorescent object (yellow object) with higher contrast flowing through c) Corresponding contrast enhanced image. d) Relative velocity of the individual CTC detected. e) Relative area of the individual CTC detected. f) Histogram of the object area for the CTC. g) Relative velocity of each CTC cluster detected. h) Relative area of each CTC cluster detected. i) Histogram of the object areas for CTC clusters.

7.4 Discussion

We have outlined an imaging/detection scheme that allows the imaging and detection of a fluorescence microscopic object in motion, and their differentiation depending on size. Additionally, we validated our method and demonstrated feasibility of an *in vivo* application. NIR light has advantages over visible light of reduced scattering in blood, increased imaging penetration depth, and decreased auto-fluorescence due to endogenous fluorophores. We chose to use a CCD for our detection device to allow for future translation of our technique. Because we use a simple CCD along with magnification and a light source, a device could be constructed that combines these elements for versatile imaging.

The sensitivity of the current approach was dependent on contrast of the cells from the background. We used an in-house NIR fluorescent compound to pre-label the cells before introducing them into the blood or mouse. We used this compound as it gave the best NIR contrast in cells (compared to commercially available Qtracker® 800 Cell Labeling Kit, ThermoFisher Scientific). We achieved enhanced cellular internalization of our NIR compound by increasing the incubation concentration, time of incubation, and adding calcium during the incubation. Presumably, an *in vivo* labeling technique could be developed that allows for bright signal emission from cells, possibly using nanoparticle technology. Another limitation of the approach was that the threshold used to determine the presence of a fluorescent object was determined at the time of image analysis. This was necessary because the light and location of detection would need to be consistent in order to set a consistent threshold. Achieving a consistent threshold would be achievable with the development of a stand-alone device with consistent lighting and imaging configurations. A stand-alone device would be ideal for the versatile imaging of CTCs in different anatomical locations.

Developing this technology could aid in the fight against cancer through the early detection and prevention of tumor metastases. Patients could be stratified based on size of CTC clusters and their therapy and surveillance programs could be tailored to match their individual prognosis. Our imaging method for CTC size stratification demonstrates that CTCs and CTC clusters can be detected and assessed *in vivo* using NIR fluorescence. Improvements in the miniaturization of the technology, and increasing the cellular fluorescence signal, will allow for the translation of this technology to improve cancer treatment for the numerous patients impacted each year.

7.5 Conclusions

We have now explored detection and size stratification of circulating tumor entities as diagnostic aspects of fluorescence imaging. In the next chapter, we focus on longitudinal high-throughput monitoring of the development of pathological presses using a fluorescent molecular imaging agent and diffuse optical tomography.

Chapter 8

Noninvasive imaging of focal atherosclerotic lesions using fluorescence molecular tomography

8.1 Introduction

Carotid artery atherosclerosis is classified as an important cause of stroke. Clinicians lack tools to detect lesion instability early enough to intervene, and are often left to manage patients empirically, or worse, after plaque rupture. Insights into the etiology of stroke and myocardial infarction suggest that rupture of unstable atherosclerotic plaque is the precipitating event. Noninvasive imaging of the molecular events signaling prerupture plaque progression has the potential to reduce the morbidity and mortality associated with myocardial infarction and stroke by allowing early intervention.[133] Unstable plaque is characterized by an eccentric neointimal lesion with a lipid core covered by a thinning cap of smooth muscle cells, active angiogenesis, increased matrix metalloproteinase activity, and translocation of monocyte/macrophages that transform into foam cells. Timely noninvasive imaging that could signal prerupture plaque progression will reduce the morbidity and mortality by allowing early intervention.[133] Although positron emission tomography (PET) and magnetic resonance imaging (MRI) are routinely used for metabolic and morphologic imaging, these modalities are not suited for frequent monitoring or even screening of at-risk patients because of ionizing radiation (PET) and expense (PET, MRI). Transcutaneous Doppler and intravascular ultrasound are insensitive to the subtle molecular changes of critical importance. Fluorescence molecular tomography (FMT) is an emerging optical imaging technology that allows tomographic and quantitative visualization of molecular events *in vivo*.[134] In this study, a custom built, fiber-based, portable, video-rate FMT system was used for proof-of-principle studies to detect C-type natriuretic peptide receptors (NPR-C) on focal atherosclerotic lesions in the superficial rabbit femoral arteries. Here, we demonstrate proof-of-principle *in vivo* molecular imaging of C-type natriuretic peptide receptor in focal atherosclerotic lesions in the femoral arteries of New Zealand white rabbits using a custom built fiber-based, fluorescence

molecular tomography (FMT) system. Longitudinal imaging showed changes in the fluorescence signal intensity as the plaque progressed in the air-desiccated vessel compared to the uninjured vessel, which was validated by *ex vivo* tissue studies. In summary, we demonstrate the potential of FMT for noninvasive detection of molecular events leading to unstable lesions heralding plaque rupture.

8.2 Materials and Methods

8.2.1 Fluorescence Molecular Tomography System

The FMT system has been described in a previous publication.[135] The FMT system consisted of a flexible imaging pad (3 cm×3 cm), containing 12 sources 785 nm 20 kHz, and 830 nm 17-kHz laser diodes as excitation source and reference, respectively.The detectors allowed for dynamic concurrent acquisition of frequency encoded fluorescence emission (830 nm; 20 kHz) and transmission reference (830 nm; 17 kHz) signals for the fast generation of ratio-metric data for tomographic reconstruction of the tissue volume. The system could report varying concentrations (1 nM to 1 μM) of indocyanine green at various depths up to 13.5 mm with a depth-dependent spatial resolution on the order of 12 mm.

8.2.2 Animal model

We used a model of focal atherosclerotic-like plaques in the femoral arteries (located $\sim$1 to 1.5 cm from skin surface) of New Zealand white rabbits. All animal studies performed were approved by the Washington University Animal Studies Committee. Endothelial denudation of surgically exposed right femoral artery was induced by air desiccation of the luminal surface as described previously.[136] The uninjured left femoral artery served as the internal control. The animals were

maintained on a cholesterol-enriched diet (>200 mg/dL in blood), and over time the air desiccation led to a focal lesion. In this animal model, anatomical co-registration was not used because the location of the lesion was apparent due to the surgical markings and identification by the surgeon at each imaging session.

8.2.3 Fluorescent imaging agent

We chose to monitor the progression of the receptor, NPR-C, which has been shown to undergo changes during atherosclerotic plaque progression and was recently evaluated as a PET imaging marker.[5] NPR-C is a cell surface protein found on endothelial, vascular smooth muscle, and macrophage cells. Natriuretic peptides (NPs) play an important role in regulating cardiovascular homeostasis. NPR-C (clearance receptor) removes NPs from circulation by receptor mediated endocytosis.[137] We evaluated a bioconjugate LS668 (Cypate-RSSc[CFGGRIDRIGAC]), consisting of a near infrared (NIR) fluorescent dye cypate conjugated to a targeting peptide, C-type atrial natriuretic peptide, specific for NPR-C (). NIR fluorescent (700 to 900 nm) imaging agents are desirable for *in vivo* imaging due to enhanced depth penetration of NIR light. The absorption spectra of LS668 was measured on a DU 640 spectrophotometer (Beckman-Coulter, Brea, CA). For all fluorescence measurements, absorbance at the excitation wavelength was kept below 0.05. Fluorescence emission spectra were recorded on a FluoroLog 3 spectrofluorometer (Horiba Jobin Yvon, Edison, NJ) using 720 nm/735-900 nm excitation/emission wavelength with 5 nm slits. The spectra were measured in dimethylsulfoxide.

8.2.4 Cell culture and microscopy of probe uptake

Stably transfected 293-T NPRC and 293-T NPRC cells were cultures in 8 well glass slides. LS668 was added to the wells (1 μM) 293-T NPRC for 1 hour. Uptake of LS668 was blocked by adding

100 µM free CANF peptide. Cells were washed after 1 hour incubation and mounted in V ectashield mounting media with DAPI (Vector Labs), followed by imaging with fluorescence imaging on Olympus BX51 upright microscope (Olympus America, PA, USA).

8.2.5 *In vivo* imaging

For *in vivo* imaging, we determined 24 h post injection of LS668 as the optimal time point, as complete clearance of LS668 from blood was achieved (serial blood sampling, data not shown). Both injured and control femoral artery of 3 animals were imaged at day 3 and weeks 1, 2, 4, 6 and 8 following the surgery. For each time point, LS668 (0.1 mg/kg intravenous) was injected and 24 h later FMT scans were performed (5 min each) in triplicates for each artery. FMT reconstruction was performed as reported earlier[138] to obtain 3D data from the tissue containing the lesion. FMT scans of the respective arteries before surgery were used as blank scans for image reconstruction.

8.2.6 Histological Analysis

Ex vivo validation studies were performed on the arteries at week 8 following the final imaging session. Prior to collecting the arterial segments, the vascular system was flushed with saline and then perfusion fixed with 4% paraformaldehyde and embedded in paraffin. Tissue sections were deparaffinized for further studies. The bright-field images of the injured artery showed a thick concentric layer of primary neo-intima (1° NEO) within the internal elastic lamina (IEL). The control artery showed intact adventitia (A), media (M) and IEL. *Ex vivo* staining of the injured artery section with LS668 (10µM; 30 min; 37 °C) followed by fluorescence microscopy (excitation/emission: 710±75 nm/ 810±90 nm. To validate the presence of macrophages infiltration, the sections were stained for macrophages with mouse monoclonal antibody to rabbit

macrophages, (clone RAM11, Dako, Carpenteria, CA, USA, 1:100 dilution). A positive signal was visualized using Vector Laboratories (Burlingame, CA, USA) alkaline phosphatase-conjugated secondary antibody and blue substrate, and nuclear fast red counterstain.

8.3 Results

8.3.1 Probe uptake in cells

The absorption and emission spectra of LS668 are shown in (Figure 8-1a). Fluorescence microscopy images demonstrated that LS668 (1 μM, 30-min incubation at 37°C, 5% CO2) was selectively internalized by stably transfected 293TNPR- C cells (Figure 8-1b). Internalization was blocked in the presence of excess (100 μM) C-ANF peptide and additionally, LS668 did not internalize into the control 293T-NPR-A cells Figure 8-1 b-d), supporting receptor mediated endocytosis of LS668.

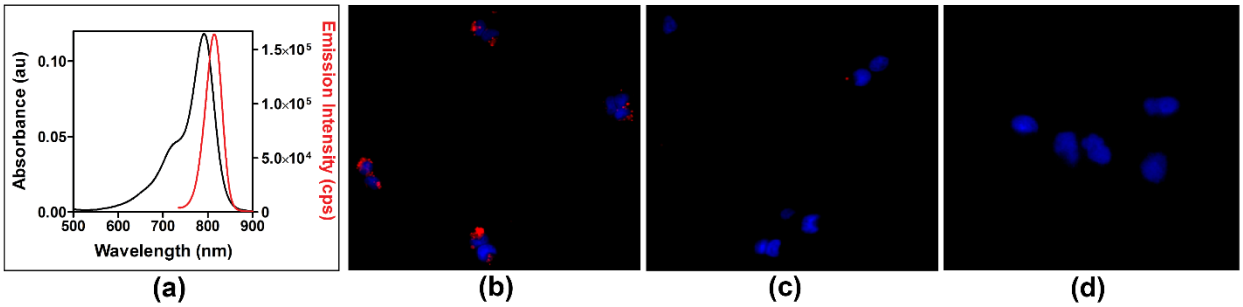

Figure 8-1: (a) Absorption and fluorescence spectra of LS668 in dimethylsulfoxide. Fluorescence microscopy images showing cellular internalization of LS668 (b) in NPR-C transfected cells, (c) inhibition of inter- nalization in presence of excess C-ANF peptide, and (d) absence of internalization in NPR-A transfected cells. Blue (DAPI, nuclear stain) and red (LS668). Scale: 100 μm.

8.3.2 *In vivo* tomographic imaging

For *in vivo* imaging, 24 h post injection of LS668 was selected as the optimal time point as clearance of LS668 from blood was achieved at 24 h. Both injured and control femoral arteries of

three animals were imaged at day 3 and weeks 1, 2, 4, 6, and 8 following the surgery. For each time point, LS668 (0.1 mg/kg intravenous) was injected and 24 h later FMT scans were performed (5 min each) in triplicates for each artery. FMT reconstruction was performed as reported earlier to obtain three-dimensional (3-D) data from the tissue containing the lesion.[138] FMT scans of the respective arteries before surgery were used as blank scans for image reconstruction. In the reconstructed data, localized fluorescence signal indicating accumulation of LS668 was observed at a depth of 4 to 16 mm and over 15 mm of length consistent with the location of the focal lesion. Coronal section images of the 3-D volumes are shown at a depth of 7 mm for one representative animal [Figure 8-2a]. The corresponding sagittal and transverse sections show the spread of the lesion along the length and breadth [Figure 8-2a,b]. Near background signal from the tissue surrounding the localized fluorescent region indicated negligible nonspecific uptake by surrounding tissue. Contralateral non-injured femoral arteries showed minimal signal indicating negligible background uptake of LS668 in the control artery. [Figure 8-2b]. Integrated fluorescence signal (directly related to the quantity of LS668 in tissue) was calculated from each tissue volume (thresholded at above 20% of respective maximum signal) [Figure 8-2c]. Unpaired t test (two tailed) showed statistically significant difference between control and injured arteries at week 2 ($P=0.0283$) and week 6 ($P=0.0282$) [Figure 8-2 c]. The changes in the signal over time most likely result from a transient increase in macrophages after injury usually at week 2, followed by a decrease resulting from the increased amount of the matrix and decrease in cellularity. Inflammation resumes in the following days or weeks due to the diet-induced macrophage-enriched unstable lesions. The variance within the cohorts highlights the differences in the pace of lesion formation in individual animals, probably as a function of their cholesterol levels. *Ex vivo* tissue biodistribution even after 24-h postinjection at week 8 showed ~3.7-fold

(n=2) higher localization of LS668 into the injured femoral artery as compared to the control femoral artery [Figure 8-2 d].

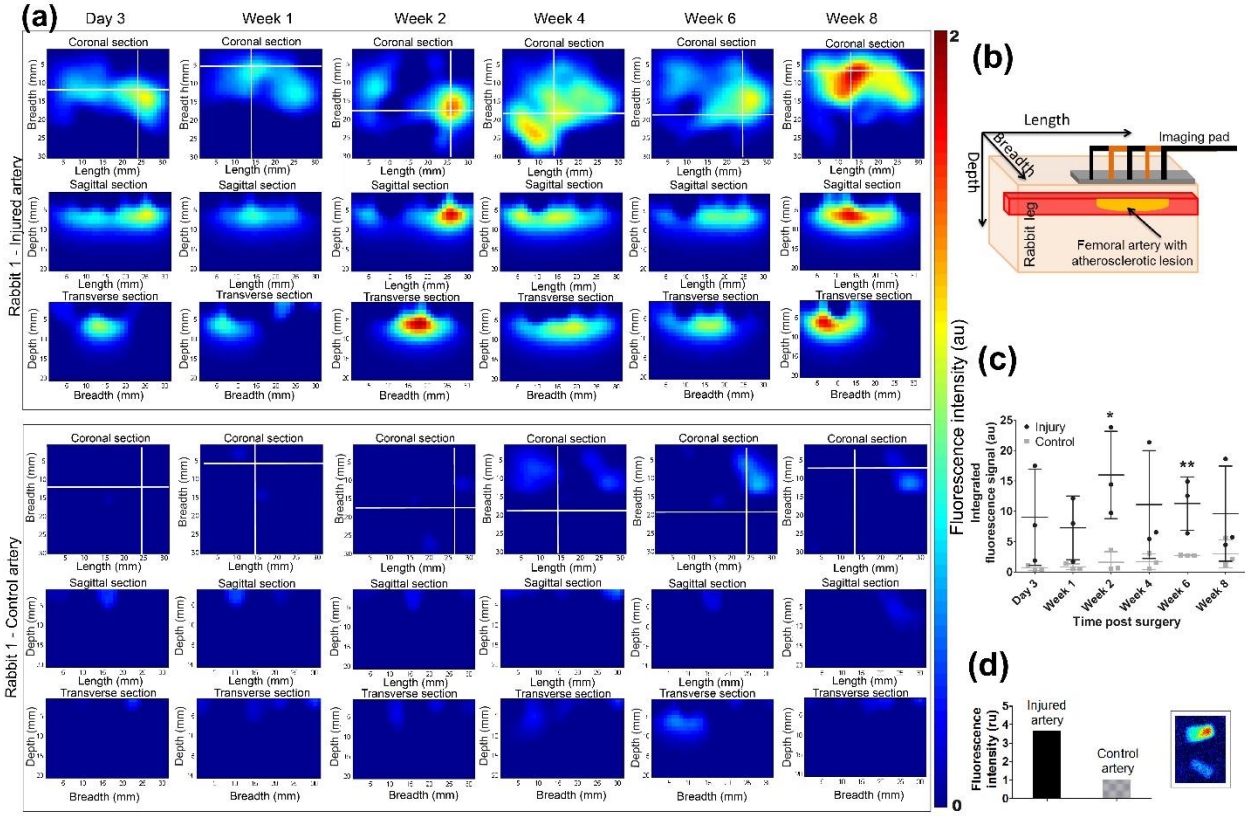

Figure 8-2: Coronal (depth ¼ 7 mm), sagittal and transverse sections of reconstructed fluorescence molecular tomography (FMT) signal from injured artery and corresponding control artery from a representative animal (rabbit 1). White lines indicate the position of the respective sagittal and transverse sections. (b) Schematic showing the relationship between the FMT images displayed to their orientation with respect to the tissue volume. (c) Time dependent changes in integrated fluorescence signal (mean AE SD, n ¼ 3) for injured and control arteries (*P ¼ 0.0283; **P ¼ 0.0282). (d) Mean (n ¼ 2) fluorescence intensity obtained from the ex vivo injured artery containing the lesion and the control artery. Adjoining figure (inset) shows the fluorescence images (excitation/emission: 785 nm/ >800 nm) of the injured artery containing the lesion (top) and the control artery (bottom).

8.3.3 *Ex vivo* and histological validation

Ex vivo histological validation studies were performed on the arteries at week 8 following the final imaging session. Prior to collecting the arterial segments, the vascular system was flushed with

saline and then perfusion fixed with 4% paraformaldehyde and paraffin embedded. Tissue sections were deparaffinized for further studies. The bright-field images of the injured artery showed a thick concentric layer of primary neointima (1° NEO) within the internal elastic lamina (IEL) [Figure 8-3a]. The control artery showed an intact adventitia (A), media (M), and IEL. *Ex vivo* staining of the injured artery section with LS668 ($10\ \mu$ M; 30 min; 37°C) followed by fluorescence microscopy showed an increased signal in the layers between A and the lumen (L), which is most likely due to the presence of infiltrating NPR-C expressing macrophages migrating from the adventitia through the media (smooth muscle cells) to accumulate in the base of the NEO closest to the media [Figure 8-3b]. The control section had a uniform fluorescence signal akin to nonspecific background. Histology sections were also stained for macrophages with mouse monoclonal antibody to rabbit macrophages (clone RAM11). Positive signal was visualized using alkaline phosphatase-conjugated secondary antibody and blue substrate, and nuclear fast red counterstain. In the injured artery, IHC showed a thickened adventitial layer and neointima with a dense accumulation of infiltrating macrophages primarily in the adventitial and medial layers of the injured femoral artery, and also some in the neointima [Figure 8-3c]. The control artery showed a negligible staining for macrophages. Serial sections were also stained for alpha-smooth muscle actin (SMA). The injured artery demonstrated medial hypertrophy and the staining for alpha-SMA was also markedly higher as compared to the control vessel (data not shown).

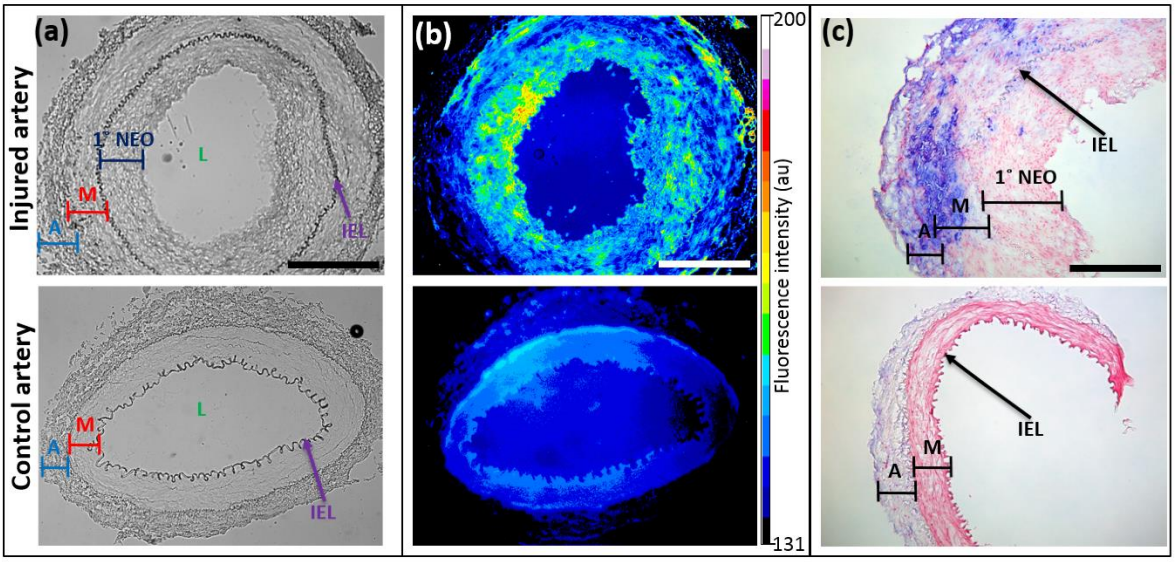

Figure 8-3: Ex vivo studies on the paraffin fixed sections of injured (top row) and control artery (bottom row) sections obtained at 8 weeks postsurgery. (a) Bright field images showing IEL, internal elastic lamina; A, adventitia; M, media; 1° NEO, primary neointima. Scale: 500 µm. (b) Corresponding fluorescence images (excitation/emission: 710±75 nm/810±90 nm) after ex vivo staining with LS668. Scale: 500 µm. (c) Immunohistochemistry on tissue sections with clone RAM11 antibody (1: 100 dilution; blue) for macrophages and counterstained with nuclear fast red. Scale: 250 µm.

8.4 Discussion

Noninvasive molecular imaging of atherosclerotic lesions with FMT allowed convenient frequent (weekly/biweekly) - a feature that is not practical for performing similar PET studies. Sequential imaging with FMT over several weeks showed quantifiable relative changes in the fluorescence intensity that may provide insights into receptor concentration as the lesion progressed. The large difference in signal from lesion between animals calls for closer monitoring of diet and disease progression in this animal model. To differentiate specific probe accumulation from inflammation related uptake, a sham injured artery can be used instead of uninjured artery. Receptor concentration can be quantified from the fluorescence signal as previously described. Additional NIR-fluorescent imaging agents to serially evaluate the progression of high-risk plaques can be employed to evaluate their potential as biomarkers.

8.5 Conclusions

This pilot study demonstrates a unique application of an FMT system for serial imaging of focal atherosclerotic plaques in the shallow femoral arteries in a rabbit model of atherosclerosis using a targeted NIR-fluorescent molecular imaging probe.

Chapter 9 Conclusions

Fluorescence imaging methods at molecular, cellular and systemic levels have demonstrated tremendous promise for studying the development of pathophysiological processes and potential as a tool for clinical diagnosis. Progress in the field is dependent on the development of novel and customized imaging probes. Through this body of work, we have developed and characterized novel fluorescent molecular probes strategies. We have then demonstrated their applications in solving critical biomedical problems. This work lays the foundation for further exploration and validation of these strategies towards broader applications.

References

1 Zeng, H., McWilliams, A. & Lam, S. Optical spectroscopy and imaging for early lung cancer detection: a review. *Photodiagnosis and photodynamic therapy* **1**, 111-122, doi:10.1016/S1572-1000(04)00042-0 (2004).

2 Hebden, J. C., Arridge, S. R. & Delpy, D. T. Optical imaging in medicine: I. Experimental techniques. *Physics in medicine and biology* **42**, 825-840 (1997).

3 Solomon, M., Liu, Y., Berezin, M. Y. & Achilefu, S. Optical imaging in cancer research: basic principles, tumor detection, and therapeutic monitoring. *Medical principles and practice : international journal of the Kuwait University, Health Science Centre* **20**, 397-415, doi:10.1159/000327655 (2011).

4 Tuchin, V. V. *Tissue optics: light scattering methods and instruments for medical diagnosis*. 3 edn, (SPIE Publications).

5 Lihong V. Wang, H.-I. W. *Biomedical Optics: Principles and Imaging*. 1 edn, (WileyInterscience).

6 A. Wax, V. B. *Biomedical applications of light scattering.*, (McGraw-Hill).

7 Wang, L. V. *Photoacoustic imaging and spectroscopy* . (CRC).

8 Berezin, M. Y., Lee, H., Akers, W., Nikiforovich, G. & Achilefu, S. Ratiometric analysis of fluorescence lifetime for probing binding sites in albumin with near-infrared fluorescent molecular probes. *Photochem Photobiol* **83**, 1371-1378, doi:DOI 10.1111/j.1751-1097.2007.00173.x (2007).

9 NPTEL, G. o. I. *Module 2: Spectroscopic Techniques, Lecture 6: Fluorescence Spectroscopy*, <http://nptel.ac.in/courses/102103044/module2/lec6/1.html> (

10 Berezin, M. Y. & Achilefu, S. Fluorescence lifetime measurements and biological imaging. *Chemical reviews* **110**, 2641-2684, doi:10.1021/cr900343z (2010).

11 Monici, M. Cell and tissue autofluorescence research and diagnostic applications. *Biotechnology annual review* **11**, 227-256, doi:10.1016/S1387-2656(05)11007-2 (2005).

12 Systems, V. *Infrared cameras enhance diagnostic medical imaging*, <http://www.vision-systems.com/articles/print/volume-17/issue-10/features/infrared-cameras-enhance-diagnostic-medical-imaging.html> (

13 ISS. *Technical Notes - Fluorescence LIfetime*, <http://www.iss.com/resources/research/technical_notes/K2CH_FLT.html> (

14 Pandey, S. K. *et al.* Multimodality agents for tumor imaging (PET, fluorescence) and photodynamic therapy. A possible "see and treat" approach. *Journal of medicinal chemistry* **48**, 6286-6295, doi:10.1021/jm050427m (2005).

15 Barrefelt, A. *et al.* Fluorescence labeled microbubbles for multimodal imaging. *Biochemical and biophysical research communications* **464**, 737-742, doi:10.1016/j.bbrc.2015.07.017 (2015).

16 Leblond, F., Davis, S. C., Valdes, P. A. & Pogue, B. W. Pre-clinical whole-body fluorescence imaging: Review of instruments, methods and applications. *J Photoch Photobio B* **98**, 77-94, doi:10.1016/j.jphotobiol.2009.11.007 (2010).

17 Gibson, A. P., Hebden, J. C. & Arridge, S. R. Recent advances in diffuse optical imaging. *Physics in medicine and biology* **50**, R1-43 (2005).

18 Wang, L., Liang, X., Galland, P., Ho, P. P. & Alfano, R. R. True scattering coefficients of turbid matter measured by early-time gating. *Optics letters* **20**, 913-915 (1995).
19 Durduran, T., Choe, R., Baker, W. B. & Yodh, A. G. Diffuse Optics for Tissue Monitoring and Tomography. *Reports on progress in physics. Physical Society* **73**, doi:10.1088/0034-4885/73/7/076701 (2010).
20 Eggebrecht, A. T. *et al.* Mapping distributed brain function and networks with diffuse optical tomography. *Nature photonics* **8**, 448-454, doi:10.1038/nphoton.2014.107 (2014).
21 Lee, K. Optical mammography: Diffuse optical imaging of breast cancer. *World journal of clinical oncology* **2**, 64-72, doi:10.5306/wjco.v2.i1.64 (2011).
22 Maji, D. *et al.* Noninvasive imaging of focal atherosclerotic lesions using fluorescence molecular tomography. *Journal of biomedical optics* **19**, 110501, doi:10.1117/1.JBO.19.11.110501 (2014).
23 Solomon, M. *et al.* Multimodal fluorescence-mediated tomography and SPECT/CT for small-animal imaging. *Journal of nuclear medicine : official publication, Society of Nuclear Medicine* **54**, 639-646, doi:10.2967/jnumed.112.105742 (2013).
24 Patwardhan, S., Bloch, S., Achilefu, S. & Culver, J. Time-dependent whole-body fluorescence tomography of probe bio-distributions in mice. *Optics express* **13**, 2564-2577 (2005).
25 Kobayashi, H. & Choyke, P. L. Target-cancer-cell-specific activatable fluorescence imaging probes: rational design and in vivo applications. *Accounts of chemical research* **44**, 83-90, doi:10.1021/ar1000633 (2011).
26 Lee, S., Park, K., Kim, K., Choi, K. & Kwon, I. C. Activatable imaging probes with amplified fluorescent signals. *Chemical Communications*, 4250-4260 (2008).
27 Lacivita, E., Leopoldo, M., Berardi, F., Colabufo, N. A. & Perrone, R. Activatable fluorescent probes: a new concept in optical molecular imaging. *Current medicinal chemistry* **19**, 4731-4741 (2012).
28 Bremer, C., Tung, C. H. & Weissleder, R. In vivo molecular target assessment of matrix metalloproteinase inhibition. *Nature medicine* **7**, 743-748, doi:10.1038/89126 (2001).
29 Lee, S. *et al.* A near-infrared-fluorescence-quenched gold-nanoparticle imaging probe for in vivo drug screening and protease activity determination. *Angewandte Chemie International Edition* **47**, 2804-2807 (2008).
30 Maxwell, D., Chang, Q., Zhang, X., Barnett, E. M. & Piwnica-Worms, D. An improved cell-penetrating, caspase-activatable, near-infrared fluorescent peptide for apoptosis imaging. *Bioconjugate chemistry* **20**, 702-709, doi:10.1021/bc800516n (2009).
31 Liu, T. W., Chen, J. & Zheng, G. Peptide-based molecular beacons for cancer imaging and therapy. *Amino acids* **41**, 1123-1134, doi:10.1007/s00726-010-0499-1 (2011).
32 Wu, C. *et al.* Preliminary investigation of the clinical significance of detecting circulating tumor cells enriched from lung cancer patients. *Journal of thoracic oncology : official publication of the International Association for the Study of Lung Cancer* **4**, 30-36, doi:10.1097/JTO.0b013e3181914125 (2009).
33 Frangioni, J. V. In vivo near-infrared fluorescence imaging. *Current opinion in chemical biology* **7**, 626-634 (2003).
34 Achilefu, S. The insatiable quest for near-infrared fluorescent probes for molecular imaging. *Angewandte Chemie International Edition* **49**, 9816-9818, doi:10.1002/anie.201005684 (2010).

35 Peng, X. *et al.* A nonfluorescent, broad-range quencher dye for Forster resonance energy transfer assays. *Analytical biochemistry* **388**, 220-228, doi:10.1016/j.ab.2009.02.024 (2009).
36 Lee, H. *et al.* Complementary optical and nuclear imaging of caspase-3 activity using combined activatable and radio-labeled multimodality molecular probe. *Journal of biomedical optics* **14**, doi:Artn 040507. Doi 10.1117/1.3207156 (2009).
37 Kotagiri, N., Niedzwiedzki, D. M., Ohara, K. & Achilefu, S. Activatable Probes Based on Distance-Dependent Luminescence Associated with Cerenkov Radiation. *Angewandte Chemie International Edition* **52**, 7756-7760, doi:DOI 10.1002/anie.201302564 (2013).
38 Berezin, M. Y. *et al.* Radioactivity-synchronized fluorescence enhancement using a radionuclide fluorescence-quenched dye. *Journal of the American Chemical Society* **131**, 9198-9200, doi:10.1021/ja903685b (2009).
39 Chen, Y. F. & Rosenzweig, Z. Luminescent CdS quantum dots as selective ion probes. *Anal Chem* **74**, 5132-5138, doi:Doi 10.1021/Ac0258251 (2002).
40 Brunner, J. & Kraemer, R. Copper(II)-quenched oligonucleotide probes for fluorescent DNA sensing. *Journal of the American Chemical Society* **126**, 13626-13627, doi:Doi 10.1021/Ja047252a (2004).
41 Wadas, T. J. & Anderson, C. J. Radiolabeling of TETA- and CB-TE2A-conjugated peptides with copper-64. *Nature protocols* **1**, 3062-3068, doi:10.1038/nprot.2006.431 (2006).
42 Tamura, K. *et al.* 64Cu-DOTA-trastuzumab PET imaging in patients with HER2-positive breast cancer. *Journal of Nuclear Medicine* **54**, 1869-1875, doi:10.2967/jnumed.112.118612 (2013).
43 Lee, M. H. *et al.* Disulfide-cleavage-triggered chemosensors and their biological applications. *Chemical reviews* **113**, 5071-5109, doi:10.1021/cr300358b (2013).
44 Achilefu, S., Dorshow, R. B., Bugaj, J. E. & Rajagopalan, R. Novel receptor-targeted fluorescent contrast agents for in vivo tumor imaging. *Investigative Radiology* **35**, 479-485 (2000).
45 Allalunis-Turner, M. J., Lee, F. Y. & Siemann, D. W. Comparison of glutathione levels in rodent and human tumor cells grown in vitro and in vivo. *Cancer research* **48**, 3657-3660 (1988).
46 Ortega, A. L., Mena, S. & Estrela, J. M. Glutathione in cancer cell death. *Cancers* **3**, 1285-1310, doi:10.3390/cancers3011285 (2011).
47 Wong, D. Y. *et al.* Glutathione concentration in oral cancer tissues. *Cancer letters* **81**, 111-116 (1994).
48 Perry, R. R., Mazetta, J. A., Levin, M. & Barranco, S. C. Glutathione levels and variability in breast tumors and normal tissue. *Cancer* **72**, 783-787 (1993).
49 Qu, Y. *et al.* Thioredoxin-like 2 regulates human cancer cell growth and metastasis via redox homeostasis and NF-kappaB signaling. *The Journal of clinical investigation* **121**, 212-225, doi:10.1172/JCI43144 (2011).
50 Parton, R. L. & Lenhard, J. R. Dimerization Reactions of Cyanine Radical Dications. *J Org Chem* **55**, 49-57, doi:Doi 10.1021/Jo00288a011 (1990).
51 Achilefu, S. *et al.* Synergistic effects of light-emitting probes and peptides for targeting and monitoring integrin expression. *Proceedings of the National Academy of Sciences of the United States of America* **102**, 7976-7981, doi:10.1073/pnas.0503500102 (2005).

52 Beard, P. Biomedical photoacoustic imaging. *Interface focus* **1**, 602-631, doi:10.1098/rsfs.2011.0028 (2011).
53 Akers, W. J. *et al.* Noninvasive photoacoustic and fluorescence sentinel lymph node identification using dye-loaded perfluorocarbon nanoparticles. *ACS nano* **5**, 173-182, doi:10.1021/nn102274q (2011).
54 Frangioni, J. In vivo near-infrared fluorescence imaging. *Curr Opin in Chem Biol* **7**, 626-634 (2003).
55 Kobayashi, H. & Choyke, P. Target-Cancer-Cell-Specific Activatable Fluorescence Imaging Probes: Rational Design and in Vivo Applications. *Acc Chem Res* **44**, 83-90 (2011).
56 Dam, G. v. *et al.* Intraoperative tumor-specific fluorescence imaging in ovarian cancer by folate receptor-α targeting: first in-human results. *Nature medicine* **17**, 1315-1319 (2011).
57 Liu, Y. *et al.* Hands-free, wireless goggles for near-infrared fluorescence and real-time image-guided surgery. *Surgery* **149**, 689-698 (2011).
58 Valdés, P. *et al.* Quantitative, spectrally-resolved intraoperative fluorescence imaging. *Scientific Reports* **2** (2012).
59 Becker, A. *et al.* Receptor-targeted optical imaging of tumors with near-infrared fluorescent ligands. *Nature Biotechnology* **19**, 327-331 (2001).
60 Luker, G. D. & Luker, K. E. Optical imaging: current applications and future directions. *Journal of nuclear medicine : official publication, Society of Nuclear Medicine* **49**, 1-4, doi:10.2967/jnumed.107.045799 (2008).
61 Dunn, A. K., Wallace, V. P., Coleno, M., Berns, M. W. & Tromberg, B. J. Influence of optical properties on two-photon fluorescence imaging in turbid samples. *Applied Optics* **39**, 1194-1201 (2000).
62 Hall, D., Ma, G., Lesage, F. & Wang, Y. Simple time-domain optical method for estimating the depth and concentration of a fluorescent inclusion in a turbid medium. *Optics letters* **29**, 2258-2260 (2004).
63 Konecky, S. D. *et al.* Quantitative optical tomography of sub-surface heterogeneities using spatially modulated structured light. *Optics express* **17**, 14780-14790 (2009).
64 Belanger, S., Abran, M., Intes, X., Casanova, C. & Lesage, F. Real-time diffuse optical tomography based on structured illumination. *J Biomed Opt* **15**, 016006, doi:10.1117/1.3290818 (2010).
65 Lukic, V., Markel, V. A. & Schotland, J. C. Optical tomography with structured illumination. *Optics letters* **34**, 983-985 (2009).
66 Patwardhan, S., Bloch, S., Achilefu, S. & Culver, J. Time-dependent whole-body fluorescence tomography of probe bio-distributions in mice. *Optics Express* **13** (2005).
67 Solomon, M. *et al.* Video-rate fluorescence diffuse optical tomography for in vivo sentinel lymph node imaging. *Biomed Opt Express* **2**, 3267–3277 (2011).
68 Stuker, F., Ripoll, J. & Rudin, M. Fluorescence molecular tomography: principles and potential for pharmaceutical research. *Pharmaceutics* **3**, 229-274, doi:10.3390/pharmaceutics3020229 (2011).
69 Corlu, A. *et al.* Three-dimensional in vivo fluorescence diffuse optical tomography of breast cancer in humans. *Optics express* **15**, 6696-6716 (2007).
70 Kepshire, D., Davis, S. C., Dehghani, H., Paulsen, K. D. & Pogue1, B. W. Fluorescence tomography characterization for sub-surface imaging with protoporphyrin IX. *Optics express* **16**, 8581–8593 (2008).

71 Kolste, K. *et al.* Macroscopic optical imaging technique for wide-field estimation of fluorescence depth in optically turbid media for application in brain tumor surgical guidance. *J Biomed Opt* **20** (2015).
72 Swartling, J., Svensson, J., Bengtsson, D., Terike, K. & Andersson-Engels, S. Fluorescence spectra provide information on the depth of fluorescent lesions in tissue. *Applied Optics* **44**, 1934-1941 (2005).
73 Leblond, F. *et al.* Analytic expression of fluorescence ratio detection correlates with depth in multi-spectral sub-surface imaging. *Physics in medicine and biology* **56**, 6823-6837, doi:10.1088/0031-9155/56/21/005 (2011).
74 Achilefu, S., Dorshow, R. B., Bugaj, J. E. & Rajagopalan, R. Novel receptor-targeted fluorescent contrast agents for in vivo tumor imaging. *Investigative radiology* **35**, 479-485 (2000).
75 Prahl, S. A., Gemert, M. J. C. v. & Welch, A. J. Determining the optical properties of turbid media by using the adding–doubling method. *Applied Optics* **32**, 559-568 (1993).
76 Prahl, S. A., Vangemert, M. J. C. & Welch, A. J. Determining the Optical-Properties of Turbid Media by Using the Adding-Doubling Method. *Applied Optics* **32**, 559-568 (1993).
77 Sabino, C. P. *et al.* The optical properties of mouse skin in the visible and near infrared spectral regions. *J Photoch Photobio B* **160**, 72-78, doi:10.1016/j.jphotobiol.2016.03.047 (2016).
78 Jacques, S. L. Optical properties of biological tissues: a review. *Physics in medicine and biology* **58**, R37-61, doi:10.1088/0031-9155/58/11/R37 (2013).
79 Cuccia, D. J., Bevilacqua, F., Durkin, A. J., Ayers, F. R. & Tromberg, B. J. Quantitation and mapping of tissue optical properties using modulated imaging. *J Biomed Opt* **14**, 024012, doi:10.1117/1.3088140 (2009).
80 Sarder, P., Maji, D. & Achilefu, S. Molecular probes for fluorescence lifetime imaging. *Bioconjugate chemistry* **26**, 963-974, doi:10.1021/acs.bioconjchem.5b00167 (2015).
81 Berezin, M. Y. & Achilefu, S. Fluorescence lifetime measurements and biological imaging. *Chemical reviews* **110**, 2641-2684, doi:10.1021/cr900343z (2010).
82 Monici, M. Cell and tissue autofluorescence research and diagnostic applications. *Biotechnol Annu Rev* **11**, 227-256, doi:10.1016/S1387-2656(05)11007-2 (2005).
83 Gallas, J. M. & Eisner, M. Fluorescence of melanin-dependence upon excitation wavelength and concentration. *Photochem Photobiol* **45**, 595-600, doi:10.1111/j.1751-1097.1987.tb07385.x (1987).
84 De Giorgi, V. *et al.* Combined non-linear laser imaging (two-photon excitation fluorescence microscopy, fluorescence lifetime imaging microscopy, multispectral multiphoton microscopy) in cutaneous tumours: first experiences. *Journal of the European Academy of Dermatology and Venereology : JEADV* **23**, 314-316, doi:10.1111/j.1468-3083.2008.03045.x (2009).
85 Dimitrow, E. *et al.* Spectral fluorescence lifetime detection and selective melanin imaging by multiphoton laser tomography for melanoma diagnosis. *Experimental dermatology* **18**, 509-515, doi:10.1111/j.1600-0625.2008.00815.x (2009).
86 Miura, Y. *et al.* Two-photon microscopy and fluorescence lifetime imaging of retinal pigment epithelial cells under oxidative stress. *Investigative ophthalmology & visual science* **54**, 3366-3377, doi:10.1167/iovs.13-11808 (2013).

87 Ying, W. NAD+/NADH and NADP+/NADPH in cellular functions and cell death: regulation and biological consequences. *Antioxid Redox Signal* **10**, 179-206, doi:10.1089/ars.2007.1672 (2008).
88 Gafni, A. & Brand, L. Fluorescence decay studies of reduced nicotinamide adenine dinucleotide in solution and bound to liver alcohol dehydrogenase. *Biochemistry* **15**, 3165-3171 (1976).
89 Maeda-Yorita, K. & Aki, K. Effect of nicotinamide adenine dinucleotide on the oxidation-reduction potentials of lipoamide dehydrogenase from pig heart. *J Biochem* **96**, 683-690 (1984).
90 Skala, M. C. *et al.* In vivo multiphoton microscopy of NADH and FAD redox states, fluorescence lifetimes, and cellular morphology in precancerous epithelia. *Proceedings of the National Academy of Sciences of the United States of America* **104**, 19494-19499, doi:10.1073/pnas.0708425104 (2007).
91 Cicchi, R. *et al.* Multidimensional non-linear laser imaging of Basal Cell Carcinoma. *Opt Express* **15**, 10135-10148 (2007).
92 Cicchi, R. & Pavone, F. S. Non-linear fluorescence lifetime imaging of biological tissues. *Analytical and bioanalytical chemistry* **400**, 2687-2697, doi:10.1007/s00216-011-4896-4 (2011).
93 Wu, T. J. *et al.* Tracking the engraftment and regenerative capabilities of transplanted lung stem cells using fluorescent nanodiamonds. *Nat Nanotechnol* **8**, 682-689 (2013).
94 Nothdurft, R., Sarder, P., Bloch, S., Culver, J. & Achilefu, S. Fluorescence lifetime imaging microscopy using near-infrared contrast agents. *J Microsc* **247**, 202-207, doi:10.1111/j.1365-2818.2012.03634.x (2012).
95 Hoffmann, K., Behnke, T., Grabolle, M. & Resch-Genger, U. Nanoparticle-encapsulated vis- and NIR-emissive fluorophores with different fluorescence decay kinetics for lifetime multiplexing. *Anal Bioanal Chem* **406**, 3315-3322, doi:10.1007/s00216-013-7597-3 (2014).
96 Kobayashi, H., Ogawa, M., Alford, R., Choyke, P. L. & Urano, Y. New strategies for fluorescent probe design in medical diagnostic imaging. *Chemical reviews* **110**, 2620-2640, doi:10.1021/cr900263j (2010).
97 Yadav, R. B. *et al.* mTOR direct interactions with Rheb-GTPase and raptor: sub-cellular localization using fluorescence lifetime imaging. *BMC cell biology* **14**, 3, doi:10.1186/1471-2121-14-3 (2013).
98 Dore, K., Labrecque, S., Tardif, C. & De Koninck, P. FRET-FLIM Investigation of PSD95-NMDA Receptor Interaction in Dendritic Spines; Control by Calpain, CaMKII and Src Family Kinase. *PloS one* **9**, e112170, doi:10.1371/journal.pone.0112170 (2014).
99 Chen, Y., Saulnier, J. L., Yellen, G. & Sabatini, B. L. A PKA activity sensor for quantitative analysis of endogenous GPCR signaling via 2-photon FRET-FLIM imaging. *Frontiers in pharmacology* **5**, 56, doi:10.3389/fphar.2014.00056 (2014).
100 Nobis, M. *et al.* Intravital FLIM-FRET imaging reveals dasatinib-induced spatial control of src in pancreatic cancer. *Cancer research* **73**, 4674-4686, doi:10.1158/0008-5472.CAN-12-4545 (2013).
101 Spoelgen, R. *et al.* Interaction of the apolipoprotein E receptors low density lipoprotein receptor-related protein and sorLA/LR11. *Neuroscience* **158**, 1460-1468, doi:10.1016/j.neuroscience.2008.10.061 (2009).

102 Chen, J., Miller, A., Kirchmaier, A. L. & Irudayaraj, J. M. Single-molecule tools elucidate H2A.Z nucleosome composition. *Journal of cell science* **125**, 2954-2964, doi:10.1242/jcs.101592 (2012).
103 Kong, A. *et al.* Prognostic value of an activation state marker for epidermal growth factor receptor in tissue microarrays of head and neck cancer. *Cancer research* **66**, 2834-2843, doi:10.1158/0008-5472.CAN-05-2994 (2006).
104 Abe, K., Zhao, L., Periasamy, A., Intes, X. & Barroso, M. Non-invasive in vivo imaging of near infrared-labeled transferrin in breast cancer cells and tumors using fluorescence lifetime FRET. *PloS one* **8**, e80269, doi:10.1371/journal.pone.0080269 (2013).
105 Kokko, T., Kokko, L., Soukka, T. & Lövgren, T. Homogeneous non-competitive bioaffinity assay based on fluorescence resonance energy transfer. *Analytica Chimica Acta* **585**, 120-125, doi:http://dx.doi.org/10.1016/j.aca.2006.12.021 (2007).
106 Vuojola, J., Lamminmäki, U. & Soukka, T. Resonance Energy Transfer from Lanthanide Chelates to Overlapping and Nonoverlapping Fluorescent Protein Acceptors. *Anal Chem* **81**, 5033-5038, doi:10.1021/ac9005793 (2009).
107 Zhang, Z. *et al.* Activatable molecular systems using homologous near-infrared fluorescent probes for monitoring enzyme activities in vitro, in cellulo, and in vivo. *Molecular pharmaceutics* **6**, 416-427, doi:10.1021/mp800264k (2009).
108 French, T. *et al.* Two-photon fluorescence lifetime imaging microscopy of macrophage-mediated antigen processing. *J Microsc-Oxford* **185**, 339-353, doi:DOI 10.1046/j.1365-2818.1997.d01-632.x (1997).
109 Goergen, C. J., Chen, H. H., Bogdanov, A., Sosnovik, D. E. & Kumar, A. T. In vivo fluorescence lifetime detection of an activatable probe in infarcted myocardium. *J Biomed Opt* **17**, 056001, doi:10.1117/1.JBO.17.5.056001 (2012).
110 Solomon, M. *et al.* Detection of enzyme activity in orthotopic murine breast cancer by fluorescence lifetime imaging using a fluorescence resonance energy transfer-based molecular probe. *Journal of biomedical optics* **16**, 066019, doi:10.1117/1.3594153 (2011).
111 Berezin, M. Y., Lee, H., Akers, W., Nikiforovich, G. & Achilefu, S. Ratiometric analysis of fluorescence lifetime for probing binding sites in albumin with near-infrared fluorescent molecular probes. *Photochemistry and photobiology* **83**, 1371-1378, doi:10.1111/j.1751-1097.2007.00173.x (2007).
112 Gioux, S., Choi, H. S. & Frangioni, J. V. Image-Guided Surgery Using Invisible Near-Infrared Light: Fundamentals of Clinical Translation. *Mol Imaging* **9**, 237-255, doi:10.2310/7290.2010.00034 (2010).
113 Achilefu, S. *et al.* Synergistic effects of light-emitting probes and peptides for targeting and monitoring integrin expression. *Proceedings of the National Academy of Sciences of the United States of America* **102**, 7976-7981, doi:10.1073/pnas.0503500102 (2005).
114 Aceto, N. *et al.* Circulating tumor cell clusters are oligoclonal precursors of breast cancer metastasis. *Cell* **158**, 1110-1122, doi:10.1016/j.cell.2014.07.013 (2014).
115 Pestana, N. *et al.* Improved diffuse fluorescence flow cytometer prototype for high sensitivity detection of rare circulating cells in vivo. *Journal of biomedical optics* **18**, 077002, doi:10.1117/1.JBO.18.7.077002 (2013).
116 Abdulreda, M. H. *et al.* High-resolution, noninvasive longitudinal live imaging of immune responses. *Proceedings of the National Academy of Sciences of the United States of America* **108**, 12863-12868, doi:10.1073/pnas.1105002108 (2011).

117 Giuliano, M. *et al.* Circulating tumor cells as early predictors of metastatic spread in breast cancer patients with limited metastatic dissemination. *Breast Cancer Res* **16**, doi:Unsp 44010.1186/S13058-014-0440-8 (2014).

118 Cristofanilli, M. Circulating tumor cells, disease progression, and survival in metastatic breast cancer. *Semin Oncol* **33**, S9-S14, doi:10.1053/j.seminoncol.2006.03.016 (2006).

119 Bauernhofer, T. *et al.* Association of disease progression and poor overall survival with detection of circulating tumor cells in peripheral blood of patients with metastatic breast cancer. *Oncol Rep* **13**, 179-184 (2005).

120 Juratli, M. A. *et al.* In Vivo Long-Term Monitoring of Circulating Tumor Cells Fluctuation during Medical Interventions. *PloS one* **10**, doi:ARTN e013761310.1371/journal.pone.0137613 (2015).

121 Frangioni, J. V. In vivo near-infrared fluorescence imaging. *Curr. Opin. Chem. Biol.* **7**, 626-634 (2003).

122 Yang, X. *et al.* Optical imaging of kidney cancer with novel near infrared heptamethine carbocyanine fluorescent dyes. *The Journal of urology* **189**, 702-710, doi:10.1016/j.juro.2012.09.056 (2013).

123 Shao, C. *et al.* Detection of live circulating tumor cells by a class of near-infrared heptamethine carbocyanine dyes in patients with localized and metastatic prostate cancer. *PloS one* **9**, e88967, doi:10.1371/journal.pone.0088967 (2014).

124 Cai, H. & Peng, F. 2-NBDG fluorescence imaging of hypermetabolic circulating tumor cells in mouse xenograft model of breast cancer. *Journal of fluorescence* **23**, 213-220, doi:10.1007/s10895-012-1136-z (2013).

125 Fidler, I. J. The relationship of embolic homogeneity, number, size and viability to the incidence of experimental metastasis. *European journal of cancer* **9**, 223-227 (1973).

126 Cheung, K. J. & Ewald, A. J. A collective route to metastasis: Seeding by tumor cell clusters. *Science* **352**, 167-169, doi:10.1126/science.aaf6546 (2016).

127 Achilefu, S. *et al.* Synergistic effects of light-emitting probes and peptides for targeting and monitoring integrin expression. *PNAS* **102**, 7976-7981 (2005).

128 Liu, Y. *et al.* Hands-free, wireless goggles for near-infrared fluorescence and real-time image-guided surgery. *Surgery* **149**, 689-698, doi:10.1016/j.surg.2011.02.007 (2011).

129 Charanya, T. *et al.* Trimodal color-fluorescence-polarization endoscopy aided by a tumor selective molecular probe accurately detects flat lesions in colitis-associated cancer. *Journal of biomedical optics* **19**, 126002, doi:10.1117/1.JBO.19.12.126002 (2014).

130 Georgakoudi, I. *et al.* In vivo flow cytometry: a new method for enumerating circulating cancer cells. *Cancer research* **64**, 5044-5047, doi:10.1158/0008-5472.CAN-04-1058 (2004).

131 Sasportas, L. S. & Gambhir, S. S. Imaging Circulating Tumor Cells in Freely Moving Awake Small Animals Using a Miniaturized Intravital Microscope. *PloS one* **9**, doi:ARTN e8675910.1371/journal.pone.0086759 (2014).

132 Markovic, S. *et al.* A Computer Vision Approach to Rare Cell In Vivo Fluorescence Flow Cytometry. *Cytom Part A* **83**, 1113-1123, doi:10.1002/cyto.a.22397 (2013).

133 Quillard, T. & Libby, P. Molecular imaging of atherosclerosis for improving diagnostic and therapeutic development. *Circulation research* **111**, 231-244, doi:10.1161/CIRCRESAHA.112.268144 (2012).

134 Weissleder, R. & Ntziachristos, V. Shedding light onto live molecular targets. *Nat Med* **9**, 123-128, doi:10.1038/nm0103-123 (2003).
135 Solomon, M. *et al.* Video-rate fluorescence diffuse optical tomography for in vivo sentinel lymph node imaging. *Biomed Opt Express* **2**, 3267-3277, doi:10.1364/BOE.2.003267 (2011).
136 Recchia, D., Abendschein, D. R., Saffitz, J. E. & Wickline, S. A. The biologic behavior of balloon hyperinflation-induced arterial lesions in hypercholesterolemic pigs depends on the presence of foam cells. *Arteriosclerosis, thrombosis, and vascular biology* **15**, 924-929 (1995).
137 Maack, T. The broad homeostatic role of natriuretic peptides. *Arquivos brasileiros de endocrinologia e metabologia* **50**, 198-207, doi:/S0004-27302006000200006 (2006).
138 Solomon, M. *et al.* Video-rate fluorescence diffuse optical tomography for in vivo sentinel lymph node imaging. *Biomed Opt Express* **2**, 3267-3277, doi:10.1364/BOE.2.003267 (2011).